# Noise and dissipation in superconducting granular aluminum circuits

Zur Erlangung des akademischen Grades eines

Doktors der Naturwissenschaften (Dr. rer. nat.)

von der KIT-Fakultät für Physik des

Karlsruher Instituts für Technologie (KIT)

genehmigte

**Dissertation**

von

M.Sc. Maximilian Kristen

| | |
|---|---|
| Tag der mündlichen Prüfung: | 30. Juni 2023 |
| Referent: | Prof. Dr. Alexey V. Ustinov |
| Korreferent: | Prof. Dr. Alexander Shnirman |

# Contents


**1 Introduction . . . . . 1**

**2 Disordered superconductors . . . . . 5**
2.1 Theoretical description of superconductivity . . . . . 5
2.1.1 Fundamental properties . . . . . 6
2.1.2 Collective modes . . . . . 9
2.1.3 Electrodynamic response . . . . . 10
2.2 Granular aluminum . . . . . 13
2.2.1 Superconducting properties . . . . . 13
2.2.2 The insulating state . . . . . 15
2.3 Noise and dissipation . . . . . 17
2.3.1 Nonequilibrium quasiparticles . . . . . 18
2.3.2 Two-level-systems . . . . . 22

**3 High impedance superconducting circuits . . . . . 29**
3.1 Microwave network theory . . . . . 29
3.2 Asymmetric resonances . . . . . 32
3.3 Bifurcation . . . . . 35

**4 Experimental methods . . . . . 37**
4.1 Sample design and fabrication . . . . . 37
4.1.1 Thin film preperation . . . . . 37
4.1.2 Sample parameters . . . . . 39
4.2 Measurement environment . . . . . 43
4.2.1 Cryogenic setup . . . . . 44
4.2.2 Microwave setup . . . . . 45
4.2.3 Sample housing . . . . . 46
4.3 Noise measurement techniques . . . . . 47
4.3.1 Frequency fluctuation tracking . . . . . 48
4.3.2 Power spectral density . . . . . 49
4.3.3 Allan deviation . . . . . 52
4.4 Electric field simulations . . . . . 54

**5 Resonance frequency fluctuations . . . 57**
5.1 Resonator frequencies and linewidths . . . 57
5.1.1 Power dependence . . . 58
5.1.2 Temperature dependence . . . 59
5.2 Resonator noise data . . . 61
5.3 Power spectral density . . . 62
5.3.1 1/f noise background . . . 63
5.3.2 Random telegraph signal . . . 65
5.4 Allan analysis . . . 66
5.5 Dissipative properties . . . 68
5.6 Discussion . . . 69

**6 Experiments with applied electric fields . . . 71**
6.1 Transmission spectrum . . . 71
6.1.1 Electric fields . . . 72
6.1.2 Strain fields . . . 74
6.2 Resonator broadening . . . 75
6.3 Anticrossing analysis . . . 77
6.3.1 TLS parameters . . . 78
6.3.2 TLS location . . . 81
6.4 Field dependent frequency fluctuations . . . 83
6.5 Discussion . . . 85

**7 Conclusion . . . 89**

**Bibliography . . . 91**

**List of Publications . . . 115**

**Appendix . . . 117**
A Fabrication parameters . . . 117
B Cable attenuation . . . 119
C Noise measurements details . . . 120
C.1 Noise spectrum of a RTS . . . 120
C.2 PSD window comparison . . . 122
D Additional TLS data . . . 123
D.1 TLS parameter . . . 123
D.2 Anticrossing gallery . . . 125
D.3 Thermal cycling . . . 126

**Acknowledgements . . . 127**

# 1 Introduction

With demands on superconducting microwave circuits increasing over the past decade [1], it has become clear that their performance is eventually limited by material losses. As a consequence, increasing experimental effort has been undertaken to characterize the microwave properties of different materials [2–5] and their surface oxides [6–8]. For these studies, superconducting resonators have emerged as one of the most versatile platforms [9], being a central part of both microwave detectors and quantum circuits for information processing [10]. In particular, noise and dissipation measured in resonators is related to decoherence of qubits made from the same materials. While most works aim to find ways to mitigate noise and dissipation, the corresponding measurements have shown to also offer unique insights into the complex physics dictating the dynamics of solid-state devices [11–13].

In the context of microwave resonators, noise typically refers to fluctuations of the resonance frequency, while dissipation corresponds to the linewidth of the resonance. In practical applications, where different frequency states have to be distinguished, both are of importance. For superconducting samples, the most universally observed sources of noise and dissipation are quasiparticles and two-level-systems. Quasiparticles (QP), on the one hand, are elementary excitation within the superconducting film, which contribute to the AC conductance, thereby causing dissipation [14, 15] and frequency fluctuations [16, 17]. Critically, the experimentally measured QP concentrations are usually much higher than expected in thermal equilibrium, a phenomenon that occurs for various reasons [18–20].

Two-level-systems (TLS), on the other hand, primarily exist in the dielectric circuit layers, e.g., surface or junction oxides. While TLS have long been known to exist in amorphous and glassy solids [21], their coherent interacting with superconducting resonators and qubits opened a more direct pathway towards uncovering their microscopic nature in recent years [22]. The most common form of TLS are atoms or groups of atoms tunnelling between two nearly degenerate configurations. If the atom is charged, such a TLS possesses an electric dipole moments which can couple dissipatively [23] or dispersively [24] to a resonant circuit. While dissipative coupling renders the circuit inoperable in a certain frequency range and provides

a parasitic channel for energy relaxation [25, 26], dispersive coupling leads to resonance frequency fluctuations in the form of $1/f$ or RTS noise [27, 28], likewise limiting the overall performance [29, 30].

In this work, noise and dissipation is studied in granular aluminum, a disordered superconducting material. Due to its particularly high kinetic inductance, granular aluminum has proven valuable for many quantum circuit applications, like kinetic inductance detectors [31, 32], nanowire devices [33, 34], and junction free [35–37] or protected [38, 39] qubit architectures. Further, it allows fabrication of high impedance resonators with an enhanced dipole coupling strength [40]. Combined with the good magnetic field resilience of disordered superconductors [41], this promotes their application in hybrid quantum systems including molecular or semiconductor spin qubits [42, 43].

For disordered superconductors, the kinetic inductance of a film is directly proportional to its normal state sheet resistance, which, in the case of granular aluminum, depends on the oxygen concentration of the sample. However, when the resistivity of the film surpasses a critical value, it become insulating instead of superconducting. The quantum nature of this so-called superconductor to insulator transition (SIT), which imposes a natural limit on the maximum obtainable kinetic inductance, is still under intense debate [44]. Fueled by the increasing use of disordered superconductor in quantum circuits and detectors as well as the realization that high-Tc superconductors are intrinsically disordered [45, 46], new theoretical and experimental efforts in this direction are still being put forward [44].

While, in the past, good microwave properties have been reported for granular aluminum samples sufficiently far from the SIT [3, 47], the high degree of disorder implies the presence of intrinsic defects, possible opening up new loss channels. Indeed, several experiments have recently reported peculiar frequency fluctuations in granular aluminum circuits [37, 48, 49]. At the same time, it remains an open question how the microwave properties of disordered films generally change in the vicinity of the SIT, as experiments studying SIT physics usually resort to scanning tunneling microscopy [50–52] or optical spectroscopy [53–55].

Here, to address these issues, multiple ultra-compact, high impedance superconducting resonators are fabricated from different granular aluminum films with the goal to investigate how noise and dissipation of these resonators changes when experimental parameters like temperature or probing power are varied. In particular, samples with different normal state resistances gradually approach the SIT are compared to that effect. Additionally, electric and strain fields are used to perform TLS spectroscopy on the same samples.

This thesis is organized as follows: In the next chapter, a short overview of the theories on (disordered) superconductors is provided, with a special focus on granular aluminum as well as material specific loss mechanisms, i.e, quasiparticles and two-level-systems. Subsequently, the theoretical framework for superconducting resonators embedded in a microwave network is provided. In chapter four, the tools necessary for fabricating and analyzing granular aluminum resonators are described. Thereafter, the experimental results are presented in two consecutive chapters, covering noise measurements and TLS spectroscopy data, respectively. Finally, the thesis is concluded by a brief summary of the main results.

# 2 Disordered superconductors

The discovery of superconductivity by Heike Kamerlingh Onnes[56] spawned a widespread quest at beginning of the 20th century to investigate the low temperature properties of different materials. Because the available range of pure metals that undergo a phase transition into the superconducting state is limited, scientist eventually explored more exotic systems to shine light on the nature of superconductivity. A group of materials that was intensely studied were disordered superconductors [57–60], i.e, metal compounds like nitrides, oxides, or silicides. The apparent contradiction between the purity of the superconducting state and the disorderd nature of these compounds was later resolved by Anderson [61], who showed that superconductivity is almost insensitive to any general type of disorder. Consequently, disordered superconductors are, to a degree, well described by the phenomenological [62–64] and microscopic theories [65, 66] that were developed for conventional superconductors.

In the first part of this chapter, a brief summary of these theories is given, extended by a discourse on the response of superconductors to high frequency electromagnetic field. There, particular attention is paid to the derivation of the kinetic inductance, a hallmark property of disordered superconductors. In the second part, the peculiarities of granular aluminum, the material of choice for this work, are detailed for different resistance regime. Finally, in the third part, mechanisms specific to superconducting thin films which can introduce noise and dissipation in microwave circuits are discussed, providing a basis for the theoretical analysis of the experiments presented in the later part of the thesis.

## 2.1 Theoretical description of superconductivity

The term "superconductivity" was coined by Heike Kamerlingh Onnes himself to describe the zero resistance state he measured on mercury below a critical temperature $T_c$ [56]. This property was viewed as the main characteristic of superconductors until 1933, when Walther Meissner and Robert Ochsenfeld found that superconductors also expel magnetic fields from their interior, up to a critical

value. Remarkably, this effect is observed regardless whether the transition to the superconducting state occurs before or after the magnetic field is applied [67], making superconductors perfect diamagnetism and thus fundamentally different from an ideal conductor.

### 2.1.1 Fundamental properties

One of the first works that provided an explanation for the fundamental properties of superconductivity was the theory developed by Ginzburg and Landau in 1950 [63]. The starting point for their calculations was the more general Landau theory for phase transitions [68]. In this context, Landau introduced an order parameter $\Psi = |\Psi|e^{i\Phi}$ that is zero on one side of the phase transition occurring at $T = T_c$ and nonzero on the other. They then expanded the free energy of the system $f(\Psi, \mathbf{A})$ around $T \approx T_c$ up to forth order in $\Psi$ and introduced gradients to the model to go beyond a constant, spatially uniform order parameter. The change of the free energy density due to the superconducting phase transition then reads

$$\delta f(\Psi, \mathbf{A}) = \alpha_{GL}|\Psi|^2 + \frac{\beta_{GL}}{2}|\Psi|^4 + \frac{1}{2m_s}|(-i\hbar\nabla - q_s\mathbf{A})\Psi|^2 + \frac{\mathbf{B}^2}{2\mu_0}, \tag{2.1}$$

where, $m_s$ is an effective mass and $q_s$ an effective charge, and $\mathbf{B} = \nabla \times \mathbf{A}$ the magnetic filed with the corresponding electromagnetic vector potential $\mathbf{A}$. The parameters $\alpha_{GL}$ and $\beta_{GL}$ are introduced as material dependent constants. In the absence of fields and gradients ($\mathbf{A} = 0$ , $\nabla\Psi = 0$, ), it is easy to see that for $\alpha_{GL} \geq 0$ the free energy has a single minimum at $\Psi = 0$, corresponding to the normal state. If $\alpha_{GL} < 0$ instead, $\delta f(\Psi)$ has a ring of minima with nonzero amplitude $|\Psi| = \Psi_\infty = \sqrt{-\alpha_{GL}/\beta_{GL}}$ but arbitrary phase $\Phi$ (see Fig. 2.1(a) for 2D representation), corresponding to the superconducting state.

Minimizing the free energy density with respect to either $\Psi$ or $\mathbf{A}$ yields the two Ginzburg-Landau equations

$$0 = \alpha_{GL}\Psi + \beta_{GL}|\Psi|^2\Psi + \frac{1}{2m_s}(-i\hbar\nabla - q_s\mathbf{A})^2\Psi, \tag{2.2}$$

$$\mathbf{j}_s = \frac{q_s\hbar}{2im_s}(\Psi^*\nabla\Psi - \Psi\nabla\Psi^*) - \frac{q_s^2}{m_s}|\Psi|^2\mathbf{A}, \tag{2.3}$$

where $\mathbf{j}_s = \nabla \times \mathbf{B}/\mu_0$ is the supercurrent density. By studying spacial variations of the order parameter, e.g., on the surface of a superconducting film, one finds from Eq. 2.2 that they decays on a characteristic lenght scale

$$\xi_{GL} = \sqrt{\frac{\hbar^2}{-2m_s\alpha_{GL}}}, \tag{2.4}$$

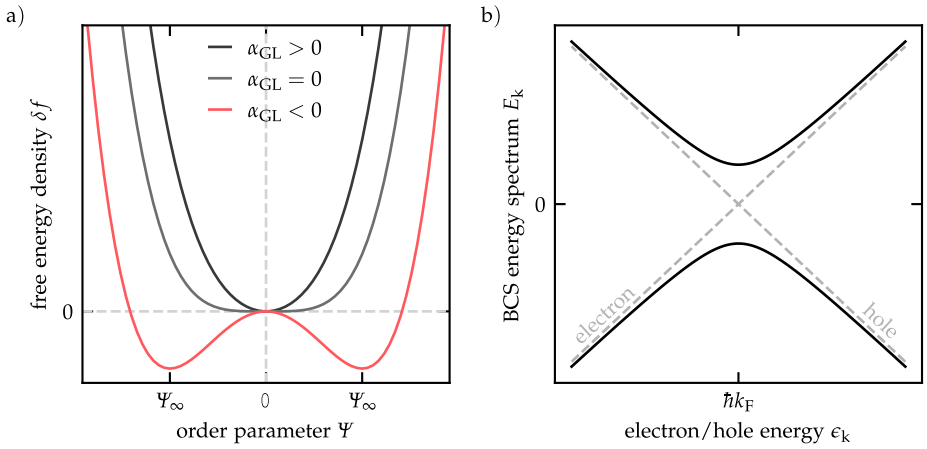


**Figure 2.1: Theories of superconductivity. a)** The phenomenological model by Ginzburg and Landau describes superconductivity as a temperature driven, second order phase transition. Below the critical temperature $T_c$ ($\alpha_{GL} \propto (T - T_c) < 0$), the order parameter minimizing the free energy takes a non-zero value. **b)** In the microscopic BCS-theory, a phonon mediated, attractive electron-electron interaction leads to the condensation of Cooper pairs, accompanied by an energy gag emerging around the Fermi surface with radius $k_F$. Excitation above this gap are superpositions of electrons and holes, called quasiparticles.

the so-called Ginzburg-Landau coherence length (Fig. 2.1(b)). Looking at the limit of a uniform $\Psi(x)$ instead, once can simplify Eq. 2.3 to

$$\mathbf{j}_s = -\frac{q_s^2}{m_s}|\Psi|^2\mathbf{A} = q_s|\Psi|^2\mathbf{v}_s, \tag{2.5}$$

where $\mathbf{v}_s$ is the velocity of the superconducting charge carriers. Prior to the theory of Ginzburg and Landau, the brothers Fritz and Heinz London developed a description of the superconductor's electromagnetic properties [62], where they found a similar expression for the supercurrent density

$$\mathbf{j}_s = q_s n_s \mathbf{v}_s. \tag{2.6}$$

Comparing Eq. 2.5 and Eq. 2.6 then identifies the Ginzburg-Landau order parameter $|\Psi|^2 = |\Psi_\infty|^2 = n_s$ as the density of the superconducting charge carriers. Using the Maxwell equations, they further showed that these currents (and the magnetic field) decay exponentially inside the superconductor on a length scale

$$\lambda_L = \sqrt{\frac{m_s}{\mu_0 q_s^2 n_s}}, \tag{2.7}$$

which is called the London penetration depth.

The Ginsburg-Landau theory and the London theory provided a first phenomenological explanation for superconductivity and the corresponding parameters are, to this day, important quantities for the characterization of superconducting materials. However, they can not make any claim on the microscopic origin of the superconducting state. This problem was first successfully tackled by John Bardeen, Leon Neil Cooper and John Robert Schrieffer (BCS) in 1957 [65]. Their theory was based on the assumption that a traveling electron causes a temporal vibration of the lattice perturbing the next electron, leading to an attractive (phonon mediated) electron-electron interaction which, at low enough temperatures, leads to the formation of so-called Cooper pairs with charge $q_s = 2e$ ($m_s = 2m_e$). Making a mean-field approximation, they were able to write down the following BCS Hamiltonian

$$\mathcal{H}_{\mathrm{BCS}} = E_{\mathrm{BCS}} + \sum_{\mathbf{k}} E_{\mathbf{k}} \gamma_{\mathbf{k}}^{\dagger} \gamma_{\mathbf{k}}, \tag{2.8}$$

where $E_{\mathrm{BCS}}$ is the energy gained by the ground state due to the electron pairing. Excitation above this ground state are called (Bogoliubov [69]) quasiparticles, which are linear combinations of the electron creation and annihilation operators $\gamma_{\mathbf{k}} = u_{\mathbf{k}}^{*} c_{\mathbf{k}} - v_{\mathbf{k}} c_{-\mathbf{k}}^{\dagger}$. The corresponding energy

$$E_{\mathbf{k}} = \sqrt{\epsilon_{\mathbf{k}}^2 + \Delta^2}. \tag{2.9}$$

is a function of the total energy $\epsilon_{\mathbf{k}}$ of an electron with momentum $\mathbf{k}$ and the strength of the mean field $\Delta \propto T_c$. From Eq. 2.9, one finds that a gap of $2\Delta$ emerges around the Fermi surface (see Fig. 2.1(b)), which is the minimum energy necessary to break a Cooper pair into two quasiparticles.

Generally, the emergence of superconductivity should be understood as a two step process. After their formation, which is accompanied by the opening of the gap $\Delta$, Cooper pairs condensate into a macroscopic quantum state which can be described by a single wave function, in accordance with Landaus initial guess. Indeed, shortly after the BCS paper, Gor'kov derived the Ginzburg-Landau equations from BCS theory [70], showing that the order parameter can be expressed as

$$\Psi \propto |\Delta| \mathrm{e}^{-i\Phi}. \tag{2.10}$$

As a consequence, there are two energy scales controlling the stability of the superconducting state: the quasiparticle gap $\Delta$ and the stiffness $J \propto n_s$ of the global phase $\Phi$, i.e, the energy required to apply a phase twist of unit magnitude over a unit length [71]. In most conventional superconductors $\Delta \ll J$, and, as shown by BCS theory, the transition temperature $T_c$ only depends on the magnitude of $\Delta$. However, in thin films made from strongly disordered superconductors with low charge carrier densities, $J$ can become relevant and even destroy the superconducting ground state, as will be discussed in Sec. 2.2.2.

### 2.1.2 Collective modes

So far, only the mean field state of the superconducting order parameter was considered, i.e, the value that minimizes the Landau free energy (or, for the BCS theory, simply a constant value $\Delta$). In reality, however, the system will rather fluctuate around $\Psi$, which manifests as collective modes of the superconducting condensate. To see this, one should write

$$\Psi = (\Psi_0 + \delta\Psi)\mathrm{e}^{-i(\Phi_0+\delta\Phi)}, \tag{2.11}$$

with $\delta\Psi$ and $\delta\Phi$ being the fluctuations of the amplitude and phase, respectively. The change of the Landau free energy density (Eq. 2.1) then becomes [72]

$$\begin{aligned}\delta f(\Psi, \mathbf{A}) = &-2\alpha_{\mathrm{GL}}\delta\Psi^2 - \frac{\hbar^2}{2m_{\mathrm{s}}}|\nabla\delta\Psi|^2 \\ &- \frac{n_{\mathrm{s}}\hbar^2}{2m_{\mathrm{s}}}\left|\nabla\delta\Phi - \frac{q_{\mathrm{s}}}{\hbar}\mathbf{A}\right|^2 + \frac{1}{2\mu_0}|\nabla\times\mathbf{A}|^2\end{aligned} \tag{2.12}$$

keeping only terms up to second order in the fluctuations (Gaussian approximation). From Eq. 2.12, one can see that the amplitude fluctuations have a mass of $-2\alpha_{\mathrm{GL}}$, which, according to macroscopic theories, coincides with the gap energy $2\Delta$. Due to this mass, they are commonly referred to as Higgs mode.

The phase fluctuations in Eq. 2.12, on the other hand, appear to be masless. This so-called Goldstone mode is a direct consequence of the spontaneously broken U(1) phase symmetry at the superconducting phase transition (Fig. 2.1(a)). However, upon closer inspection, one realizes that the free energy is invariant under the gauge transformation

$$\mathbf{A} \to \mathbf{A} - \frac{\hbar}{q}\nabla\delta\Phi. \tag{2.13}$$

Thus, the phase fluctuations are eaten by the field $\mathbf{A}$, which in turn becomes massive inside the superconductor (Anderson-Higgs mechanism).[1] The corresponding mass $n_{\mathrm{s}}q_{\mathrm{s}}^2/2m_{\mathrm{s}}$ is typically much larger than $\Delta$.

Due to the high energy associated with the "Goldstone" mode and the large phase space for the decay of the Higgs mode into quasiparticles, they are both difficult to observe experimentally. In disordered superconductors, however, the situation might be different [73]. Various calculations based on a effective bosonic $XY$ lattice model [74] showed that the phase modes can appear as a subgap spectral feature

[1] The Meißner effect can be thought of as a direct consequence of this mass term.

in the optical conductivity if the disorder is sufficient [75–78]. In particular, it was shown that these modes acquire an effective dipole moment [75]

$$d_\Phi = \frac{1}{E_\alpha}\left(\sum_i J_{i,i+x}\Delta_\mu \hat{\Phi}_{i,\alpha}\right)^2, \tag{2.14}$$

where $\hat{\Phi}_{i,\alpha}$ is the phase operator of each mode with energy $E_\alpha$, $\Delta_{\mu=x,y}$ is the phase gradient in $\mu$ direction, and $J_{i,j}$ is the local phase stiffness that dictates the hopping of Cooper pairs between different lattice sites.

From Eq. 2.14 on can see that if the system is homogeneous ($J_{i,j} = J$), $d_\Phi$ is proportional to the total phase gradient over the sample which vanishes for periodic boundary conditions. In the inhomogeneous case, however, $d_\Phi$ is finite and should be experimentally accessible. While some works promoted the idea that Higgs modes could also appear below the gap in disordered samples [79], explicit calculations [80] suggest that signatures of amplitude fluctuations only appear du to strong mixing with underlying phase modes.

### 2.1.3 Electrodynamic response

Because Cooper pairs condense into a collective, macroscopic state (Eq. 2.10) that is insensitive to small-scale effects like scattering, DC currents inside a superconductor flow without any resistance. However, in this work, superconducting films are mainly studied by applying microwave signals. There, to describe the non-static response of a superconductor to alternating fields, it is usefully to follow the approach of Tinkham and introduce the complex conductivity of the superconducting state $\sigma_s = \sigma_1 - i\sigma_2$ [81, 82]. An instructive starting point for the calculation of $\sigma_s$ is the Drude model [83], which describes the electrical transport in materials as

$$\sigma = \frac{nq^2\tau}{m(1+\omega^2\tau^2)} - i\frac{nq^2\omega\tau^2}{m(1+\omega^2\tau^2)} \tag{2.15}$$

Here, $\tau$ is relaxation time of the charge carriers $q$ with mass $m$ and $\omega$ is the frequency of the alternating field. In the normal state, $\omega\tau \ll 1$ for all relevant frequencies and Eq. 2.15 describes Ohmic behavior. In the superconducting state, the relaxation time $\tau \to \infty$ is practically infinite and the conductivity becomes almost purely imaginary $\sigma_s \approx i\sigma_2 = -in_s q_s^2/(m_s\omega)$.[2] Here, $q_s = 2q_e$ and $m_s = 2m_e$

[2] For DC currents, the resistivity $\rho_{dc} = 1/\sigma_{dc}$ of the superconductor is always zero because $\sigma_{dc} = nq^2\tau/m \propto \tau \to \infty$. However, for $\omega \neq 0$, the ratio $\sigma_{dc}/\omega\tau$ remains finite and the AC resistance can become nonzero, i.e, the Cooper pairs no longer provide a perfect shunt for the quasiparticles.

are the charge and mass of a Cooper pair, respectively. A more specific expression for $\sigma_s$ can be derived from BCS theory, including also quasiparticle contributions ($\sigma_1 \neq 0$, see Sec. 2.3.1 for details)). Since, for $T \ll T_c$, these only has a minor effect on the overall behavior, their (direct) influence will be neglected for the following discussion.

In the thin film limit, where the film thickness $t_z \ll \lambda_L$ is small compared to the field penetration, the current distribution is almost uniform and one can write $\sigma_s \frac{w_x t_z}{l_y} = \frac{1}{Z} = \frac{1}{R+i\omega L_k}$ [14]. Then it is easy to see that the AC response of the superconductor is given by a sheet inductance

$$L_k^{\square} = \frac{L_k}{N^{\square}} = \frac{1}{\omega |\operatorname{Im}(\sigma_s)| t} = \frac{m_s}{n_s q_s^2} \frac{1}{t_z}, \tag{2.16}$$

where $N^{\square} = l_y / w_x$ is the number of squares of the wire with lenght $l_y$ and width $w_x$. By extending the BCS theory to time-varying electromagnetic interactions, Mattis and Bardeen found a more handy expression for the complex conduction, relating it to the normal state conductance $\sigma_n$ [66]. Then, the sheet inductance

$$L_k^{\square} \approx \frac{\hbar R_n^{\square}}{\pi \Delta}, \tag{2.17}$$

can directly be calculated from the normal state sheet resistance $R_n^{\square} = (\sigma_n t_z)^{-1}$, which is easily accessible experimentally.

Because conceptionally, this inductance emerges from the momentum $v_s \propto \omega$ obtained by the Cooper pairs from electric field, it is referred to as kinetic inductance. As with any conductor, wires made from a superconducting film also possess a geometric inductance $L_g$, whose energy is stored in the magnetic field instead. To characterize a superconducting film, it is sometimes useful to introduce the kinetic inductance fraction

$$\alpha = \frac{L_k}{L} = \frac{L_k}{L_k + L_g}. \tag{2.18}$$

Discorded superconductors are metal compounds with a sizable fraction of insulating material, and their charge carrier density, also in the superconducting state, is therefore typically greatly reduced (compared to the pure superconductor). In accordance with Eq. 2.16, this yields a higher increased kinetic inductance and it is possible to achieve $\alpha$ values close to unity. Microscopically, this dependence can be understood from the fact that, in order to carry the same current, less charge carri-

ers have to be proportionally faster, and the overall kinetic energy $\frac{1}{2}n_s m_s v_s^2 \propto L_k$ increases [3].

An expression for the kinetic inductance can also be derived more rigorously from the phenomenological theories of superconductivity. Using the first London equation $E = \frac{dv_s}{dt}\frac{m_s}{q_s}$ (direction of the wire, 1D case), one directly finds from the definition of the inductance

$$L_k^{\square} = \frac{U}{N^{\square}}\left(\frac{dI_s}{dt}\right)^{-1} = \frac{E}{t_z}\left(\frac{dj_s}{dt}\right)^{-1} = \frac{m_s}{q_s t_z}\left(\frac{dj_s}{dv_s}\right)^{-1} = \frac{m_s}{|\Psi|^2 q_s^2 t_z}, \tag{2.19}$$

where in the last step Eq. 2.5 was used. As shown above, the order parameter is equal to $|\Psi|^2 = |\Psi_\infty|^2 = n_s$ for weak perturbation fields and Eq. 2.19 thus reduces to Eq. 2.16, consistent with London theory. However, in order to treat the kinetic inductance more precisely one should consider the more general case of strong fields, where $q_s\mathbf{A} = \mathbf{v}_s m_s$ is no longer small. Then, $|\Psi|$ will change from $\Psi_\infty$ (but still has the same value everywhere, $t_z \ll \xi_{GL}$) and minimizing Eq. 2.1 yields [84]

$$|\Psi|^2 = n_s\left(1 - \frac{m_s v_s^2}{2|\alpha_{GL}|}\right) \tag{2.20}$$

instead. The corresponding current density $j_s \propto v_s^3$ has a maximum value when the charge carrier velocity reaches $v_c^2 = 2|\alpha_{GL}|/(3m_s)$. The maximum value can be identified as a critical current density

$$j_c = \frac{2}{3}q_s n_s\left(\frac{2|\alpha_{GL}|}{3m_s}\right)^{\frac{1}{2}} = \frac{2}{3}q_s n_s v_c. \tag{2.21}$$

above which the superconducting state is no longer favorable. Combining Eq. 2.19 to 2.21 then yields a expression for the kinetic inductance in case of strong perturbations [85, 86]

$$L_k^{\square} = \frac{m_s}{n_s q_s^2 t_z}\left(1 - \frac{v_s^2}{v_c^2}\right)^{-1}. \tag{2.22}$$

By inverting $j_s(v_c)$ along its stable branch, Eq. 2.22 can be rewritten in a more convenient form as [87]

$$L_k^{\square} \approx \frac{m_s}{n_s q_s^2 t_z}\left(1 + \left(\frac{2j_s}{3j_c}\right)^2 + \mathcal{O}(j_s^4)\right). \tag{2.23}$$

[3] Equation 2.16 can also be calculated by equating the total kinetic energy with the inductive energy stemming from the current $I = q_s v_s n_s w d$

Thus, the kinetic inductance shows a nonlinear dependence on the currents flowing in the superconductor. Experimental consequences of this dependence for resonant circuits where $j_c \propto n_s$ is small, which is typically the case for disordered superconductors, will be discussed in section 3.3.

## 2.2 Granular aluminum

The disordered superconductor studied in the framework of this work is granular aluminum. Historically, this material was first investigated in the sixties and seventies, mainly by Abeles in New Jersey [88–91] and Deutscher in Tel-Aviv [92–95]. In the following decades, granular aluminum was repeatedly used in experiments designed to gain insight in the peculiar nature of superconductivity in granular films [52, 53, 76, 96–99], but was also studied with regard to its applicability in superconducting circuits, like single photon detectors [32], superconducting qubits [35–37, 39], high impedance resonators [3, 41, 47, 49] or nanowire [34] and long Josephson junction experiments [100]. In microwave applications, it has showed promising loss properties, [47, 48], in addition to a particularly sizable kinetic inductance $L_k^{\square}$, unmatched by other popular disordered superconductors [101].

### 2.2.1 Superconducting properties

Granular aluminum consists of pure aluminum grains with diameter $w_{grain} \sim 3 - 5\,\mathrm{nm}$ embedded in a matrix of amorphous aluminum oxide $AlO_x$ (see Fig. 2.2(a)), which self assembles during the deposition of aluminum in a oxygen atmosphere. In the process, the oxygen partial pressure influences the thickness of the oxide barrier separating the grains, around $s \sim 1 - 2\,\mathrm{nm}$ and thus the normal state sheet resistance $R_n^{\square}$. Bellow $T_c$, the individual grains first become superconducting and are subsequently coupled via the Josephson effect. [4] In this process, the phase difference $\Delta\Phi$ of coupled grains equalizes and all Cooper pairs again form a global condensate that is described by a single wave function (Eq. 2.10). This assumption is supported by the fact that the coherence length $\xi_{GL} \sim 10\,\mathrm{nm}$ in granular aluminum is larger then the grain size [34].

[4] The Josephson effect [102] describes coherent tunneling of Cooper pairs through an insulating barrier separating two superconductors. The corresponding current is proportional to the phase difference $\Delta\Phi$ between the two superconductors

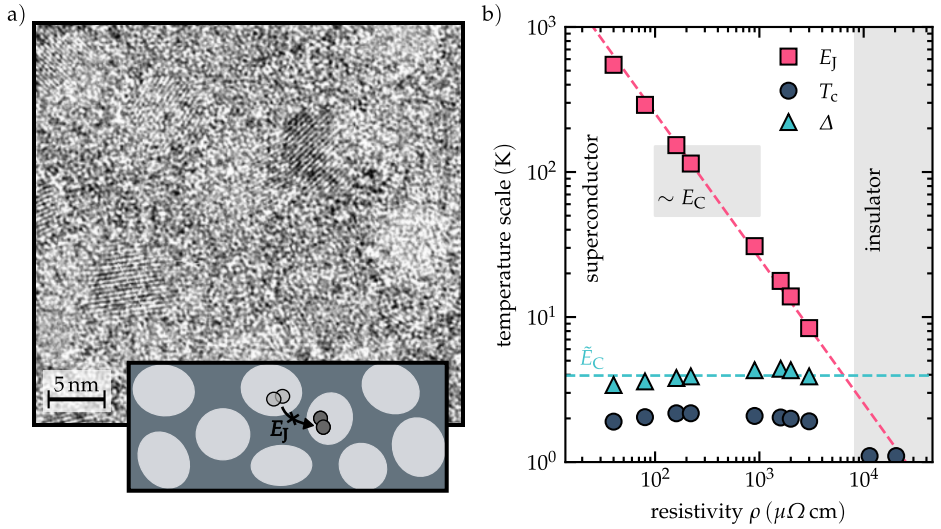


**Figure 2.2: Microscopic picture and superconducting properties of granular aluminum. a)** Transmission electron microscope (TEM) picture of granular aluminum. Inset illustrates the aluminum grains (Al) embedded in a matrix of amorphous aluminum oxide ($AlO_x$). In the superconducting state, the Josephson mechanism allows for coherent transport of Cooper pairs between neighboring grains. **b)** Critical temperature $T_c$, superconducting gap $\Delta$ and Josephson energy $E_J$ for increasing resistivity. When the Josephson energy surpasses the effective Coulomb energy $\tilde{E}_C \propto \Delta$, the film is an insulator below $T_c$. Data adopted from Ref.[3] and Ref.[53].

As shown in Fig. 2.2(b), the superconducting transition temperature of granular aluminum strongly depends on the normal state resistivity $\rho = R_n^{\square} t_z$ of the film. This phenomena is, due to the shape of the dependency, referred to as the "superconducting dome". Noticeable, the maximum value $T_c \sim 2\,\mathrm{K}$ at $\rho \sim 1000\,\mu\Omega\,\mathrm{cm}$ is around two times higher than pure aluminum ($T_{c,Al} = 1.2\,\mathrm{K}$). This enhancement was one of the main incentives to initially study granular superconductors [88]. The question concerning its origin has not yet conclusively been resolved, despite numerous explanations that have been brought forward over the years, some of which will be discussed in the following.

Based on early experiments, Ginzburg [103] and later Cohen and Douglass [104] suggested that the effective electron-phonon interaction $V_{k,k'}$ near the surface of a superconducting grain may be larger than that of the bulk. This mechanism was explained by the presence of surface phonons or an enhanced electron pairing across the grain boundaries, respectively. If the width of the enhanced surface

region $w_s$ is larger then half the grain size $w_{grain}/2$, the transition temperature of the granular superconductor can be calculated as [104]

$$k_B T_c \approx 1.13 \hbar \omega_D e^{-\frac{1}{D(E_F) V_s}} \tag{2.24}$$

However, if $w_s \leq w_{grain}$, the transition temperature should not depend on the grain size, which contradicts experimental observation [92, 93]. In the opposite case $w_s > w_{grain}$, Eq. 2.24 becomes more complicated and one would expect two values for the gap, which has not been observed experimentally [52, 90].

Around the same time, Parmenter calculated an enhancement of $T_c$ from the quantization of electron motion due to the grain size [105]. He showed that modifying the BCS theory for a finite lattice parameter leads to an enhanced electron-electron interaction $V$ and consequently, an enhancement $x = T_c/T_{c,bulk}$ of the critical temperature by

$$x \log(x) = \frac{\pi}{2} \left( \frac{l_P}{d} \right)^3 \tag{2.25}$$

where $l_P = (\lambda_L^2 \xi_0)^{1/3}$ is the characteristic lengthscale of this effect, with the BCS coherence length $\xi_0 = \frac{\hbar v_f}{\pi \Delta}$. For aluminum, $l_P = 6.2\,\text{nm}$, which results in $x \sim 2$ for grain sizes on the order of $w_{grain} \sim 3\,\text{nm}$, in reasonable agreement with experimental findings (Fig. 2.2(b)).

Following Parmenters line of thinking, a number of recent theoretical works proposed that the enhancement can be understood as a consequence of the electronic shell effect [106–108]. Essentially, small isolated grains are treated as atomic nanoclusters which, due to their finite size, have a discrete spectrum of states. If the highest of theses states is degenerate, there is a sharp peak in the density of states $D(E_F)$ at the Fermi level which, according to Eq. 2.24, enhances $T_c$. The questions whether this effect survives in a bulk granular material composed of such nanograins, where inter-grain coupling should smear out the sharp peak, was affirmatively answered by Mayoh and García-García [109]. They also showed that, as the resistivity increases, individual grains progressively decouple and the smearing effect is reduced, explaining the increase of $T_c$ with $\rho$ on the left side of the dome.

### 2.2.2 The insulating state

When the resistivity takes on even larger values and the transparency of the barriers is reduced, it becomes increasing hard for the film to uphold a superconducting state due to the weakened coupling between the grains. Above a critical value,

films cooled down below $T_c$ then become insulating instead [110]. This is know as the (disorder driven) superconductor to insulator phase transition (SIT).

Based on earlier considerations from Anderson [111], Abeles [91] suggested that the two relevant energy scales in a granular superconductor are the Josephson coupling $E_J$ and the Coulomb energy $E_C$. On the one hand, the Josephson energy [112]

$$E_J = \frac{\Delta}{2}\frac{R_0}{R_n^{\square}}, \tag{2.26}$$

which in granular aluminum is identical to the phase stiffness $J$, attempts to lock the phases of neighboring grains. Here, $R_0$ is the superconducting resistance quantum. Because the quantum variables for the phase and the charge carrier number do not commute $[\hat{\Phi}, \hat{N}] = i$, this leads to a delocalization of the Cooper pairs as mentioned above. On the other hand, the Coulomb energy [113]

$$E_C \simeq \frac{e^2}{4\pi\epsilon_0\epsilon_r d}\frac{s}{s+\frac{d}{2}}, \tag{2.27}$$

where $\epsilon_r \sim 8.5$ is the dielectric constant of the barrier [53], attempts to localize the Cooper pairs on the grain, enhancing quantum phase fluctuations $\delta\Phi$. For the simple case of two grains weakly coupled together, Abeles came to the conclusion that for

$$E_J < \frac{E_C}{2} \tag{2.28}$$

all Cooper pairs localize and the film will be insulating [91]. Shortly after, Efetov [114] obtained a similar result from a full quantum mechanical model for electrons in a system of metal grains, including phonon interaction, short and long-range Coulomb repulsion and inter grain tunneling.

The inequality of Eq. 2.28 is generally referred to as the Anderson-Ables criterion. For a large ratio $\Delta/E_C \ll 1$, it predicts that there is a parametrically large number of resistances $R_n^{\square} < \Delta R_0/E_C$ where superconductivity should exist even if the corresponding film made from normal grains would be an insulator ($R_n^{\square}/R_0 > 1$). While this prediction was supported by some early experiments [115], many later works found that superconducting and insulating samples can be separated solely by their normal-state resistance [116, 117], with a critical value on the order of $R_0$.

The discrepancy between the intuitive theoretical considerations and the experimental findings was eventually resolved by Chakravarty *et. al.* [118], who proposed a model that also takes into account quasiparticle tunneling [119]. They found that in the case of strong Coulomb interaction $\Delta/E_C \sim 10^{-1} - 10^{-2}$, the virtual

tunneling process reduces the Coulomb interaction down to a renormalized value $\tilde{E}_C \approx \Delta R_n^{\square}/R_0$. In this case, Anderson-Ables criterion can be rewritten as

$$R_n^{\square} > R_0 = \frac{h}{(2e)^2} = 6.453\,\mathrm{k}\Omega, \tag{2.29}$$

in good agreement also with later experiments on different granular materials [53, 120, 121].

For granular superconducting films near the SIT (right side of the dome), the reduction of $T_c$ is a consequence of already emerging phase fluctuations. This fluctuations increase as the Cooper pairs progressively localize with deceasing Josephson energy $E_J \propto 1/R_n^{\square}$ [122]. As seen in Fig. 2.2(b), the onset of this reduction remarkably coincides with $E_J < E_C$, i.e., the point where pairing becomes significant locally [123]. This suggest that the superconductivity on each individual grain remains strong in the presence of growing inter-grain barriers and solely the critical temperature of the whole film is weakened.

When the condition 2.29 is eventually met, the fluctuations become so large that the phase coherence across the sample is lost and the film becomes insulating. Note that the exact value of $R_c$ differs between materials, but is usually close to $R_0$. More recent experiments [53, 99] suggest that the phase transition is rather governed by $\rho = R_n^{\square} t$, which could be due to the crossover into the 3D limit for films with $t \gg \xi_{GL}$. Also, while optical measurements found evidence for an superconducting gap persisting across $T_c$ [99], the question whether individual grains can remain superconducting in the insulating region is not definitively answered yet.

Motivated by the mechanism at hand, the SIT in granular aluminum is commonly interpreted as a Mott transition for the Cooper pairs [114]. Within this picture, the Josephson energy plays the role of the width of the band. When this width becomes less than the (effective) Colomb energy, the Cooper pairs localize and the superconductivity is destroyed. This picture is consistent with Muon spin spectroscopy ($\mu$SR) data showing a weak resistance dependence of the density of states $D(E_F)$, which is predicted to behave noncritical at the Mott transition [96, 98, 124].

## 2.3 Noise and dissipation

Due to the purity associated with the superconducting state it seem, at first glance, counter intuitive to assume that they are a relevant loss channel for any superconducting system. It turns out, however, that sources of noise and dissipation can be

manifold and that good microwave properties, while crucial for their application in superconducting circuits, are not guaranteed.

In this work, noise and dissipation are studied in superconducting resonators, whose center frequencies $\omega_r$ correspond to the actual measurement signal im most application, i.e, the particular value of $\omega_r$ provides information on the state of the circuit. For example, a resonator weakly coupled to a superconducting qubit changes its resonance frequency depending on the state of the qubit [125] and kinetic inductance detectors count single photons by measuring the frequency shift they induce in a superconducting resonator via breaking of a Cooper pair [31]. To effectively discriminate between different frequency states, narrow resonators with low internal dissipation $\kappa_i$ are thus desirable. Further, unwanted fluctuations of the resonance frequency $\delta\omega_r$ on the timescale of the measurement can be classified as (resonator) noise in this context. Combined, the signal quality of a resonator and, likewise, the overall performance of the respective quantum circuit can then quantitatively be described by a signal-to-noise ratio SNR $\propto (\delta\omega_r\kappa_i)^{-1}$ that becomes worse as noise and dissipation increase. In the following, the two most prominent candidates that are typically found to make the largest contribution are discussed: Quasiparticles and two-level-systems.

### 2.3.1 Nonequilibrium quasiparticles

At non-zero temperatures and frequencies, the system can provide the energy necessary ($2\Delta$) to break a Cooper pair with a certain probability, creating quasiparticle excitations (QP) above the gap. There, they adhere to normal scattering processes, which leads to a finite ac resistance of the superconducting film and thus a increased loss rate for the resonator. Additionally, because the QP density $n_{qp}$ is directly (negatively) correlated with the Cooper pair density $n_s$, fluctuations in the QP number result in a changing kinetic inductance and thus resonator frequency noise (Eq. 2.19). Note that the magnitude of these effects scale with the kinetic inductance fraction $\alpha$, which is typically on the order of unity for disordered superconductors.

The exact influence of QP on a superconducting resonator can be calculated from the work of Mattis and Bardeen [66], who extended the BCS theory to study the anomalous skin effect of superconductors, therein describing its electrodynamic properties. With regards to the complex conductivity $\sigma_s = \sigma_1 - i\sigma_2$, they found that at low frequencies $\hbar\omega \ll \Delta$ it relates to the normal state conductivity $\sigma_n$ as

$$\frac{\sigma_1(\omega)}{\sigma_n} = \frac{2}{\hbar\omega}\int_{\Delta}^{\infty} dE \frac{E^2+\Delta^2+\hbar\omega E}{\sqrt{E^2-\Delta^2}\sqrt{(E+\hbar\omega)^2-\Delta^2}}[f(E)-f(E+\hbar\omega)] \tag{2.30}$$

and

$$\frac{\sigma_2(\omega)}{\sigma_n} = \frac{1}{\hbar\omega}\int_{\Delta}^{\Delta+\hbar\omega} dE \frac{E^2+\Delta^2-\hbar\omega E}{\sqrt{E^2-\Delta^2}\sqrt{\Delta^2-(E-\hbar\omega)^2}}[1-2f(E)]. \tag{2.31}$$

Here, $f(E)$ is the distribution function for quasiparticles which, in case of thermal equilibrium, is given by the Fermi-Dirac distribution $f(E) = 1/(e^{E/k_BT}+1)$ [126]. Physically, the reactive response $\sigma_2$ comes from the Cooper pairs and the dissipative response $\sigma_1$ from the QPs. For $k_BT \ll \Delta$, the corresponding QP density can be written as [10]

$$n_{qp} = 4D(E_F)\int_{\Delta}^{\infty} dE \frac{E}{\sqrt{E^2-\Delta^2}} f(E) \approx 2D(E_F)\sqrt{2\pi k_BT\Delta}e^{-\Delta/k_BT} \tag{2.32}$$

Note that as $T \to 0$, both $n_{qp}$ and $\sigma_1$ are linearly proportional to $f(E)$ and thus vanish exponentially as $e^{-\Delta/k_BT}$. Thus, for $T \ll T_c$, the dissipative response of the superconductor should be very small compared to the reactive response, i.e, $\sigma_1 \ll \sigma_2$.

However, QP densities experimentally measured in superconductors [19, 127], including granular aluminum [47], are typically much higher then predicted by Eq. 2.32. Such nonequilibrium (or excess) QP can, for example, be generated by electromagnetic [128] and ionizing [129] radiation or high-energy impacts from cosmic rays [20]. Theoretically, QP localization at the spatial fluctuations of the gap edge has been suggested to effectively increase the observed QP density, an effect that might be particularly relevant for disordered superconductors [18].

With regards to the complex conductivity, adding a thermal QP or a nonequilibrium QP has the same effect [14]. Then, the quantity of interest is the change of the conductance with the QP number $d\sigma/dn_{qp} = \frac{\delta\sigma/\delta T}{\delta n_{qp}/\delta T}$. At low temperatures ($k_BT \ll \Delta$), an approximate expression is given by

$$\frac{d\sigma_1}{dn_{qp}} = \sigma_n \frac{1}{D(E_F)\hbar\omega}\sqrt{\frac{2\Delta}{\pi k_BT}}\sinh(\xi)K_0(\xi) \tag{2.33}$$

and

$$\frac{d\sigma_2}{dn_{qp}} = -\sigma_n \frac{\pi}{2D(E_F)\hbar\omega}\left(1+\sqrt{\frac{2\Delta}{\pi k_BT}}e^{-\xi}I_0(\xi)\right), \tag{2.34}$$

where $\xi = \hbar\omega/(2k_BT)$ and $I_n$, $K_n$ are the $n$th order modified Bessel function of the first and second kind, respectively.

In microwave transmission experiments with superconducting resonators the complex conductivity is usually not directly accessible. Instead, the complex surface

impedance $Z_s$ is the quantity being probed. For thin films $t_z \ll \lambda_L$, where the field penetrates the entire film and the current distribution is uniform, the surface impedance relates to the conductivity as

$$Z_s = R_s - iX_s = \frac{1}{(\sigma_1 - i\sigma_2)t_z}. \tag{2.35}$$

From Eq. 2.35 it follows that $\delta Z_s / Z_s = \delta\sigma/\sigma$ and one can then easily see that [130]

$$\delta Z_s = \iota |Z_s| \delta n_{qp}, \tag{2.36}$$

with

$$\begin{aligned} \iota = \frac{\delta\sigma/|\sigma|}{\delta n_{qp}} \approx & \frac{1}{D(E_F)\pi}\sqrt{\frac{2}{\Delta\pi k_B T}}\sinh(\xi)K_0(\xi) \\ & + i\frac{1}{2D(E_F)\Delta}\left(1+\sqrt{\frac{2\Delta}{\pi k_B T}}e^{-\xi}I_0(\xi)\right). \end{aligned} \tag{2.37}$$

Equation 2.36 and 2.37 reveal that both the surface resistance $R_s$ and the surface reactance $X_s$ increase with the QP density. The latter, of course, is due to the corresponding change in the Cooper pair density. The effect of $\delta Z_s$ on the resonator frequency $\delta\omega_r$ and the internal loss $\delta\kappa_i$ scales with $\alpha$ and is therefore increased in films with a high kinetic inductance. Finally, for $\alpha = 1$, noise and dissipation relate to the QP density as follows

$$\begin{aligned} \frac{\delta\omega_r^{QP}}{\omega_r} &= -\frac{1}{2}\frac{X_s(T) - X_s(0)}{X_s(0)} = -\frac{1}{2}\frac{\mathrm{Im}(\iota)|Z_s|}{X_s(0)}\delta n_{qp} \\ \frac{\delta\kappa_i^{QP}}{\omega_r} &= \frac{R_s(T) - R_s(0)}{X_s(0)} = \frac{\mathrm{Re}(\iota)|Z_s|}{X_s(0)}\delta n_{qp}. \end{aligned} \tag{2.38}$$

Thus, at any event that suddenly changes the quasiparticle density $n_{qp}$, e.g., a high energy impact or sudden change of temperature, the frequency and linewidth of the resonator change simultaneously according to

$$\kappa_i = \kappa_{i,0} + 2\delta\omega_r \frac{\mathrm{Re}(\iota)}{\mathrm{Im}(\iota)} \tag{2.39}$$

By inserting Eq. 2.39 into the usual expression for the transmission signal $S_{21}(\omega_r)$ of a microwave resonator, which will be derived in the next section (Eq. 3.15), one finds that the resulting trace (Inset Fig. 2.3(b)) is quenched and does not coincide with the resonance circle.

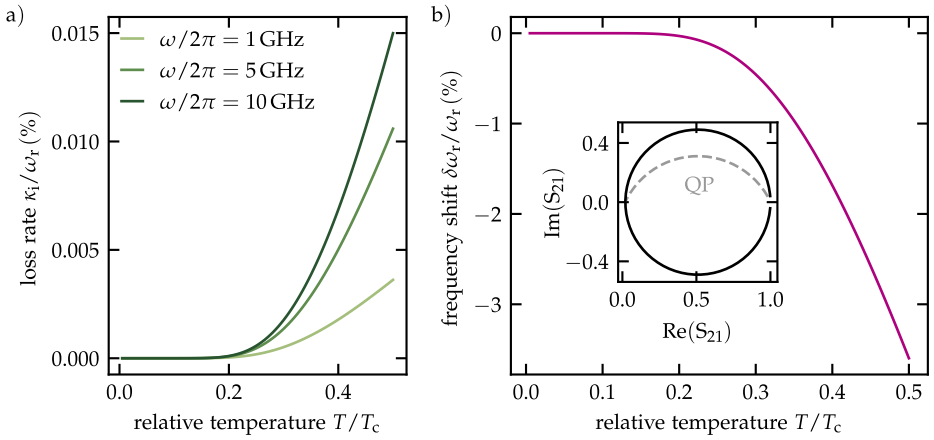


**Figure 2.3: Mattis-Bardeen theory for Bogoliubov quasiparticles. a)** Internal loss $\kappa_i$ of a superconducting film at various frequencies due to the activation of quasiparticles at increasing temperatures, as described by Eq. 2.40. **b)**Temperature dependent frequency shift of a superconducting microwave resonator according to Eq. 2.41. Inset: Resonator trajectory, Eq. 2.39, due to a quasiparticle generating event. For all plots $\Delta = 300\,\mu\mathrm{eV}$ was assumed.

In the steady state ($\delta n_{qp} = 0, n_{qp} \neq 0$), an approximate expression for the internal losses of the resonator due to (equilibrium) quasiparticles can be given at low frequencies and temperatures [10]

$$\frac{\kappa_i^{QP}(\omega, T)}{\omega_r} = \frac{R_s(T)}{X_s(T)} \approx \frac{\sigma_1(T)}{\sigma_2(0)} \approx \frac{4}{\pi} \frac{\sinh(\xi) K_0(\xi)}{e^{\frac{\Delta}{k_B T}}}. \tag{2.40}$$

For a typical granular aluminum sample ($\Delta = 300\,\mu\mathrm{eV}$, $T_c = 2\,\mathrm{K}$) operated and measured in the microwave regime, this loss only becomes relevant when temperatures exceed $T \approx 0.2 T_c$

Similarly, according to Turneaure *et al.* [131], a simple formula for the temperature depended frequency shift due to thermally activated quasiparticles can be derived

$$\frac{\delta\omega_r^{QP}}{\omega_r} = -\frac{1}{2}\sqrt{\frac{\Delta\pi}{2k_B T}} e^{-\frac{\Delta}{k_B T}}, \tag{2.41}$$

using the fact that $X_s = \omega\mu_0\lambda_L$ [130]. Note that the magnitude of the effect is determined by the size of the superconducting gap alone. As a consequence, measurements of the resonator frequency at different temperatures can be fitted to obtain an estimate for $\Delta$ (see Sec. 5.1).

### 2.3.2 Two-level-systems

Besides quasiparticles, the most prominent source of noise and dissipation in quantum circuits are tunneling two-level-systems (TLS) which are universally observed in the amorphous circuit dielectrics, typically surface or junction oxides. For disordered superconductors, and granular aluminum in particular, such TLS would also be expected within the film. Microscopically, TLS are pictured as atoms or groups of atoms with two nearly degenerate configurations (Fig. 2.4(a)). At low temperatures, these states are connected by a coherent tunneling process. The corresponding effective charge gives rise to an electric dipole moment that can couple to the AC fields of quantum circuits where they are causing frequency fluctuations and energy relaxation [22].

#### Standard tunneling model

Historically, TLS have first been postulated in amorphous solids in the 1970s to explain the thermal and acoustic properties of cold glasses, which differed fundamentally from the predictions of the Debye model [132, 133]. The unusually high heat capacitance, which was observed universally over a wide range of solids, suggested the presence of additional degrees of freedom, which absorb and store energy at low temperatures. A corresponding theory, the so-called standard tunneling model (STM), was provided by Phillips and Anderson [21, 134], linking these degree of freedom to TLS. Independent of its physical origin, they described a TLS as a virtual particle trapped in a double well potential (Fig. 2.4(b)). The potential is characterized by an asymmetry energy $\epsilon_{\mathrm{TLS}}$ and the dynamics are governed by the purely quantum inter-well tunneling rate $\Delta_{\mathrm{TLS}}/\hbar$. The Hamiltonian of this system reads

$$\mathcal{H}_{\mathrm{TLS}} = \frac{1}{2}\epsilon_{\mathrm{TLS}}\hat{\sigma}_z + \frac{1}{2}\Delta_{\mathrm{TLS}}\hat{\sigma}_x, \tag{2.42}$$

where $\hat{\sigma}_z$ and $\hat{\sigma}_x$ are Pauli matrices. Due to the tunneling between the wells, the eigenstates

$$\begin{aligned} |\Psi_+\rangle &= \sin\left(\frac{\theta}{2}\right)|L\rangle + \cos\left(\frac{\theta}{2}\right)|R\rangle \\ |\Psi_-\rangle &= \cos\left(\frac{\theta}{2}\right)|L\rangle - \sin\left(\frac{\theta}{2}\right)|R\rangle \end{aligned} \tag{2.43}$$

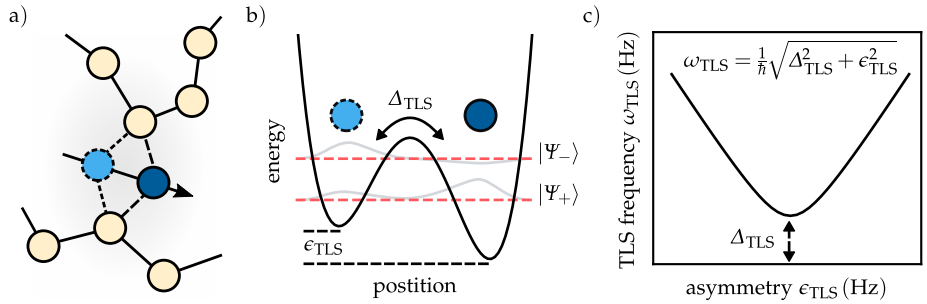


**Figure 2.4: Standard tunneling model for two level systems (TLS). a)** Illustration of the conventional picture of TLS in amorphous materials: atoms tunneling between meta-stable positions. **b)** Double well potential describing the dynamics of a TLS. The asymmetry energy $\epsilon_{\mathrm{TLS}}$ and tunneling energy $\Delta_{\mathrm{TLS}}$ determine the transition frequency $\omega_{\mathrm{TLS}}$ between the TLS eigenstates $|\Psi_+\rangle$ and $|\Psi_-\rangle$. **c)** TLS frequency as a function of the potential asymmetry, which, according to Eq. 2.48, can be tuned by electric or strain fields. The displayed hyperbolic shape is characteristic for TLS.

can be written in terms of the eigenstates in the left ($|L\rangle$) and right ($|R\rangle$) well, mixed by an angle $\tan\theta = \Delta_{\mathrm{TLS}}/\epsilon_{\mathrm{TLS}}$. The energy difference between the eigenstates is then given by

$$E_{\mathrm{TLS}} = E_+ - E_- = \hbar\omega_{\mathrm{TLS}} = \sqrt{\epsilon_{\mathrm{TLS}}^2 + \Delta_{\mathrm{TLS}}^2}, \tag{2.44}$$

with $\omega_{\mathrm{tls}}$, the transition frequency of the TLS. In the limit $|\epsilon_{\mathrm{TLS}}| \gg \Delta_{\mathrm{TLS}}$ the virtual particle is trapped in one minimum and well described by $|L\rangle$ or $|R\rangle$. For $|\epsilon_{\mathrm{TLS}}| \approx 0$, the particle is maximally delocalized and the eigenstates are a superposition of the two well states, as illustrated in Fig. 2.4(b).

Using Wentzel–Kramers–Brillouin (WKB) theory, the tunneling energy can be estimated as

$$\Delta_{\mathrm{TLS}} = \hbar\omega_L e^{-\lambda}. \tag{2.45}$$

There, the tunneling parameter

$$\lambda = \sqrt{\frac{2m_{\mathrm{TLS}}V}{\hbar^2}}s_{\mathrm{W}} \tag{2.46}$$

depends on the barrier height $V$, the separation of the wells $s_{\mathrm{W}}$ and the effective mass of the particle $m_{\mathrm{TLS}}$. Because of the exponential scaling, the exact value for the average frequency of the localized states $\omega_L$ is usually not important. Due to the random nature of the atomic configurations, both $\epsilon_{\mathrm{TLS}}$ and $\lambda$ are expected to be uniformly distributed in the STM. As a consequence, the TLS density of

states $D_{\mathrm{TLS}}(E) \approx D_0$ is found to be approximately constant. Note that this result is obtained under the assumption that TLS do not interact with each other, which is generally not true (see, e.g., [135]).

In the presence of static electric or strain fields, the potential landscape in the vicinity of the TLS is modified. There, the dominant effect is typically a change in the asymmetry of the TLS potential, while changes in the barrier height can usually be ignored [21]. Because this coupling to both fields is linear, the modified asymmetry energy can simply be written as [136]

$$\epsilon_{\mathrm{TLS}} \rightarrow \epsilon_{\mathrm{TLS}} + 2\mathbf{d}_{\mathrm{TLS}}\mathbf{E} + 2\gamma_{\mathrm{TLS}}\mathbf{S}, \tag{2.47}$$

resulting in a TLS transition frequency

$$\omega_{\mathrm{TLS}} = \frac{1}{\hbar}\sqrt{\Delta_{\mathrm{TLS}}^2 + (\epsilon_{\mathrm{TLS}} + 2\mathbf{d}_{\mathrm{TLS}}\mathbf{E} + 2\gamma_{\mathrm{TLS}}\mathbf{S})^2}. \tag{2.48}$$

as shown in Fig. 2.4(c). Here, $\mathbf{E}$ is the electric and $\mathbf{S}$ the strain field. The electric dipole of the TLS is then defined as $\mathbf{d} \equiv \delta\epsilon_{\mathrm{TLS}}/(2\delta\mathbf{E})$ and analogously, $\gamma \equiv \delta\epsilon_{\mathrm{TLS}}/(2\delta\mathbf{S})$ is the TLS' deformation potential.

### Weakly coupled TLS

The STM proved to be very successful at predicting the behavior of amorphous materials at the lowest temperatures. In resonant quantum circuits, TLS are typically present in the naturally forming, amorphous surface oxides (dielectrics). For disordered superconductors, particularly granular aluminum, the intrinsically disordered structure should also allow the presence of material defects (TLS) below the surface of the film. As mentioned above, the dipole moment of a TLS can couple to the oscillating fields of the resonator (with a coupling rate $g$), which leads to distinct resonator behavior that can also be described in the scope of the STM.

The largest contribution in this regard is made from an ensemble of (mostly) weakly coupled TLS ($g << \kappa_{\mathrm{r}}$), where the details of the interaction with the individual TLS is negligible, but the density of contributing TLS is high ($\sim 0.5\,(\mathrm{GHz}\,\mu\mathrm{m}^2)^{-1}$ [23, 137]). If the majority of these TLS are in their ground state, there is a finite probability that a resonator photon is absorbed by one of the TLS. This results, on average, in an increased loss rate $\kappa_{\mathrm{i}}$. However, when the number of circulating photons $\overline{n}$ exceeds some characteristic value $n_{\mathrm{c}}$, near resonant TLS ($\omega_{\mathrm{TLS}} \sim \omega_{\mathrm{r}}$) are excited by an effective Rabi frequency [138] $\Omega_{\mathrm{TLS}} \propto \sqrt{\overline{n}}$ larger then their loss rate

$\gamma_{\mathrm{TLS}}$ and the population of non excited TLSs decreases. This results in a power depended resonator loss tangents [21]

$$\tan(\delta) = \frac{F \tan(\delta_0) \tanh\left(\frac{\hbar\omega}{2k_{\mathrm{B}}T}\right)}{\sqrt{1 + (\overline{n}/n_{\mathrm{c}})^{\beta}}} + \tan(\delta_+) \tag{2.49}$$

that decreases as $\overline{n}$ increases. Here, $\tanh\left(\frac{\hbar\omega}{2k_{\mathrm{B}}T}\right)$ is the thermodynamic average of the TLS mean field and $\tan(\delta_+)$ is a residual loss rate due to, e.g., quasiparticles or coupling to the transmission line. The dielectric loss tangent $\tan(\delta_0) = \pi P_0 d^2/(3\epsilon)$ generally depends on the TLS spectral and spatial density $P_0$ as well as the (mean) dipole moment $d$ and is dressed by a filling factor $F$, which accounts for the participation ratio of the dielectric material [21]. Loss as describe by Eq. 2.49 has been observed and analyzed for a wide range of materials and resonator geometries [48, 139–143], where the exponent $\beta$ was found to be on the order of unity.

Besides providing a loss channel for the resonator, TLS also contribute to the dielectric constant $\epsilon$ seen by the resonator, resulting in a frequency shift described by [144, 145]

$$\frac{\delta\omega_{\mathrm{r}}^{TLS}}{\omega_{\mathrm{r}}} = -\frac{F}{2}\frac{\delta\epsilon}{\epsilon} = \frac{F\tan(\Delta)}{\pi}\left[\mathrm{Re}\,\Psi\left(\frac{1}{2} + \frac{1}{2\pi i}\frac{\hbar\omega_{\mathrm{r}}}{k_{\mathrm{B}}T}\right) - \ln\left(\frac{\hbar\omega_{\mathrm{r}}}{k_{\mathrm{B}}T}\right)\right], \tag{2.50}$$

where $\Psi$ is the complex digamma function. This equation has been used in the past to derive values for the effective TLS density $P_0 d^2 \propto \tan(\delta_0)$ in amorphous materials [21], usually through measurements of $\delta\epsilon$. In contrast to Eq. 2.49, the effect described by Eq. 2.50 also arises due to non-resonant TLS which are not saturated at high photon numbers. Measuring this frequency shift is thus not limited to the single-photon regime.

### Strongly coupled TLS

Due due the high TLS density in amorphous materials, there is a non-zero change to find TLS in the spacial as well as spectral ($\omega_{\mathrm{TLS}} \approx \omega_{\mathrm{r}}$) vicinity of the resonator that have a large dipole moment $\mathbf{d}$ aligning with the resonator field $\mathbf{E}_{\mathrm{rms}}$. In the single photon regime, the coupling $g$ between these TLS and the resonator can be comparably strong and one finds that [146]

$$g = \frac{\Delta_{\mathrm{TLS}}}{\omega_{\mathrm{TLS}}}\frac{\mathbf{d}\mathbf{E}_{\mathrm{rms}}}{\hbar^2}. \tag{2.51}$$

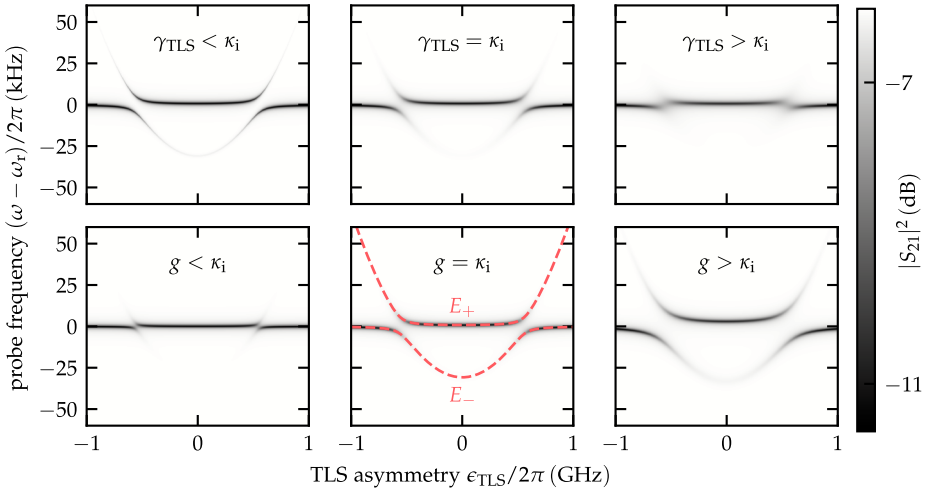


**Figure 2.5: Anticrossings for different parameters of the coupled resonator-TLS system.** Transmitted microwave signal when tuning the TLS hyperbola $\omega_r$ through the resonator at $\omega_r = 5\,\text{GHz}$. The energies $E_\pm$ of the coupled system are described by Eq. 2.53. Top row: Simulated anticrossings for different TLS decay rate $\gamma_{TLS}$ at a constant coupling rate $g = \kappa_i = 5\,\text{MHz}$. Bottom row: Simulated anticrossings for different coupling strength $g$ at a constant TLS decay rate $\gamma_{TLS} = \kappa_i = 5\,\text{MHz}$. Plots generated from Eq. 6.3.

Experiments on distributed resonators, where $E_{rms}$ can be particularly high, have shown that individual strongly coupled TLS can directly be observed in the resonator transmission spectrum [143, 147, 148]. Such results can be interpreted based on a full quantum mechanical analysis of the corresponding Jaynes-Cummings Hamiltonian, which reads

$$\mathcal{H} = \hbar\omega_r \hat{r}\hat{r}^\dagger + \hbar\omega_{TLS}\hat{\sigma}_z - i\hbar g(\hat{\sigma}_- \hat{r}^\dagger - \hat{\sigma}_+ \hat{r}). \tag{2.52}$$

Here, $\hat{\sigma}_z$ is the third Pauli matrix and $\hat{\sigma}_-$ and $\hat{r}$ are the raising operators of the resonator and the TLS, respectively. Diagonalizing Eq. 2.52 in the basis of the combined occupation number yields the following eigenenergies for this system

$$E_\pm = \frac{\hbar}{2}(\omega_r + \omega_{TLS}) \pm \hbar\sqrt{g^2 + \left(\frac{\omega_r - \omega_{TLS}}{2}\right)^2}. \tag{2.53}$$

Thus, when the frequency of the resonator and the TLS come close ($|\omega_r - \omega_{TLS}| \sim g$) they hybridize instead of crossing each other, i.e., they are no longer separately observable. This process is commonly referred to as "anticrossing". As shown in Fig. 2.5, the visibility of anticrossings does, in practice, not only depend on the coupling strength $g$, but also the loss rate of the TLS $\gamma_{TLS}$ and of the resonator $\kappa_i$.

Due to the hyperbolic shape of the TLS transition frequency, it always crosses the resonator mode twice (given that $\Delta_{\mathrm{TLS}}/\hbar < \omega_{\mathrm{r}}$), resulting in two anticrossings that are symmetric around $\epsilon_{\mathrm{TLS}} = 0$.

### Thermal fluctuators

In the STM, the interacting between different TLS is assumed to also be of a dipole-dipole type (similar to Eq. 2.48), where the effective strength is given by the dimensionless parameter $\chi_0 = D_0 U_0$, where, $U_0 = d^2/\epsilon$. Direct measurements in bulk amorphous materials give values of $\chi \approx 10^{-3} - 10^{-4}$ [149], i.e., the TLS are only weekly coupled and thus this effect is often neglected.

However, with the advance of superconducting quantum circuits, the level of detail with which TLS could be studied increased tremendously. Using superconducting qubits, the strong interaction of individual TLS has been directly observed and probed [135]. Previous to these findings, measurements of resonators with low intrinsic loss rates showed a much weaker power dependence as predicted by Eq. 2.49 [150, 151], which was explained by TLS interacting [149, 152].

Further evidence is provided by measurements of the frequency noise of superconducting resonators [150, 153–155]. There, the magnitude of this noise decreased with increasing readout power as $\propto \overline{n}^{-1/2}$ and with increasing temperature as $\propto T^{-(1+\mu)}$. These findings are consistent with a generalized tunneling model [27, 28], where near-resonant resonant TLS ($\omega_{\mathrm{TLS}} \sim \omega_{\mathrm{r}}$) are expected to interact with surrounding two-level-fluctuators (TLF), i.e, TLS who have a much lower energy $\omega_{\mathrm{TLF}} < k_{\mathrm{B}}T$ and are therefore subjected to slow, thermal fluctuations. The coupling to these TLF causes an energy drift, bringing the resonant TLS in and out of resonance (see Fig. 2.6(a)), which in turn causes fluctuations of the resonator frequency $\delta\omega_{\mathrm{r}}$. In particular, this model also explains the spectral distribution of this resonator noise, which typically decreases as $1/f$. Here, $f$ is the frequency of the spectral analysis (see Sec. 4.3 for details). For the individual TLF, the spectrum is expected to have Lorentzian form, due to the stochastic nature of their switching. However, as illustrated in Fig. 2.6(b), averaging over a large number of fluctuators with varying switching times results in an overall $1/f$ noise spectrum of the resonant TLS and thus the resonator itself [156].

A key assumption of the generalized tunneling model is that, due to the interaction being larger than expected from the STM, the TLS density of states has a weak power law dependency $D_{\mathrm{TLS}}(E) \propto D_0 E^{\mu}$, where $\mu \approx 0.3$ has been derived from experiments [132, 157]. Thus, the number of TLF is proportional to $T^{1+\mu}$. Generally, resonator noise only occurs if the coupling between the TLS and the TLF is greater

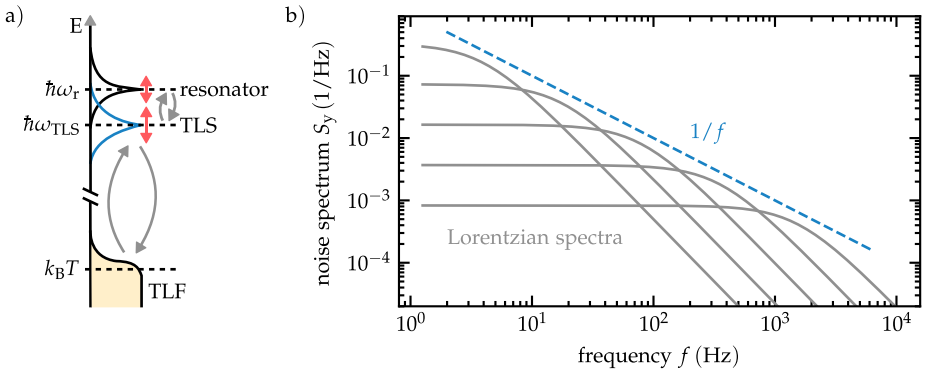


**Figure 2.6: Two-level fluctuators as a source of 1/f noise. a)** Illustration of a TLS fluctuating due to its interaction with a bath of thermally activated two-level-fluctuators (TLF) with energies below $k_BT$. A electric dipole coupling transfers these fluctuations from the TLS onto the resonator. **b)** Each TLF produces a Lorentzian noise spectrum. The superposition of Lorentzian noise from TLF with different lifetimes results in 1/f noise. Illustration inspired by Ref. [30]

then the TLS decay rate. In other words, the fluctuators must be located within a sphere of radius $R_{max} = (U_0/\gamma_{TLS})^{1/3}$ from the TLS, where $\gamma_{TLS} \propto T^{1+\mu}$. As a consequence, the volume of the sphere grows and therefore the noisy sensitivity increases at lower temperatures, even though the number of TLF decreases.

Based on these assumptions, an analytical computation yields [27]

$$S_y \propto \frac{N_f D_0 U_0^2}{\sqrt{1+\overline{n}/n_c}} \frac{1}{T^{1+\mu}} \frac{1}{f}, \tag{2.54}$$

for the noise spectrum, where $N_f$ is the number of sufficiently coupled fluctuators. Note that, since $n_c \propto T^{2(1+\mu)}$, at high powers the temperature dependence of the spectra is constant. Resonator noise data evaluated by this model showed exponents $\mu$ in the range from 0.2 to 0.7 [27, 149, 158], in good agreement with the presumed scaling of the density of states. Recent experiments with superconducting qubits further affirmed the physical model of TLF, finding evidence also for resonant TLS predominantly coupled to only a single fluctuator, resulting in a distinct Lorentzian peak in the noise spectrum [29, 30].

# 3 High impedance superconducting circuits

The theoretical and experimental progress made in superconducting circuits in the past 20 years stimulated their application in an increasing variety of research fields, including quantum information processing [159], particle detector physics [10] or microwave photonics [160]. One of the most versatile and widely used components in superconducting circuits are resonators, which are a crucial part of almost any practical application. Since they are also comparable easy to fabricate and well described theoretically, they provide a convenient platform to study how material choices affect the circuit performance.

For their measurement, superconducting resonators (or quantum circuits in general) usually get embedded in a microwave network. From the response of the network to microwave signals, one can then infer information about the resonators, e.g., their resonance frequency. In this chapter, the theoretical framework for the analysis of a resonant microwave network is provided. In particular, the frequency response of high impedance resonators is studied, including a detailed description of the influence of the usually encountered impedance missmatch in the measurement environments and of increased probing powers.

## 3.1 Microwave network theory

A common technique to describe a microwave network is provided by the scattering matrix formalism. For an arbitrary network, it relates the complex input to the complex output voltage via [161]

$$\mathbf{V}^{out} = S\mathbf{V}^{in}. \tag{3.1}$$

There, the coefficients of the scattering matrix are given by

$$S_{ij} = \frac{V_i^{out}}{V_j^{in}}, \tag{3.2}$$

where $S_{ii}$ is the reflection coefficient of port $i$ and $S_{ij}$ is the transmission from port $j$ to port $i$. For reciprocal networks, it is easy to see that $S_{ij} = S_{ji}$ for all ports.

The microwave network employed throughout this work consists of a two port transmission line shunted by a load impedance $Z_R$ (see Fig. 3.1(a)). For the ideal case where the transmission line ports are matched to the the $Z_0 = 50\,\Omega$ industrial standard of the network, the S-matrix reads [161]

$$S = \begin{pmatrix} S_{11} & S_{12} \\ S_{21} & S_{22} \end{pmatrix} = \begin{pmatrix} (1+\frac{2Z_R}{Z_0})^{-1} & (1+\frac{Z_0}{2Z_R})^{-1} \\ (1+\frac{Z_0}{2Z_R})^{-1} & (1+\frac{2Z_R}{Z_0})^{-1} \end{pmatrix}. \tag{3.3}$$

In particular, the load impedance $Z_R$ is provided by a distributed $\lambda/2$ resonator formed by a open-end waveguide of lenght $l_y$ (see section 4.1). Neglecting the coupling to the transmission line $C_c$, the resonance condition of such a distributed resonator is [3]

$$\omega_r = \frac{1}{2l_y\sqrt{L_l C_l}} = \frac{1}{\sqrt{LC}}, \tag{3.4}$$

where $L_l$ and $C_l$ are the inductance and capacitance per unit lenght respectively and the factor $1/2$ incorporates the fundamental mode having a wavelength of $\lambda/2$. By assigning an effective capacitance $C$ and inductance $L$, one can translate the distributed resonator to the lumped-element RLC-circuit sketched in Fig. 3.1(a). For resonators made from granular aluminum films with high normal state sheet resistances ($R_n^{\square} \gtrsim 500\,\Omega$), the corresponding inductance is mostly kinetic such that $L \approx N^{\square} L_k^{\square}$. Also, $L$ is usually much larger than the capacitance, resulting in an impedance $Z = \sqrt{L/C} \gg Z_0$. Hence the name "high impedance circuit".

For a superconductor, one might expect that $R \to 0$, i.e, the resonator is lossless. However, as discussed in the previous section, quasiparticles and surface dielectric provide no negligible loss channels in real experiments such that $R \neq 0$. These intrinsic losses are described by the internal loss rate

$$\kappa_i = \frac{P_{loss}}{E_{tot}} = \frac{R}{L}, \tag{3.5}$$

where $E_{tot} = \frac{1}{2}LI^2$ is the total energy stored in the resonator and $P_{loss}$ is the energy dissipated per cycle.

The coupling of the resonator to the transmission line via the capacitance $C_c$ is an additional source of energy dissipation and analogous to Eq. 3.5, it can be described by a (coupling) loss rate $\kappa_r$. If $\omega_r C_c$ is small compared to the resonator impedance $Z_R \approx \sqrt{L/C}$, one can write [162]

$$\kappa_c = \frac{2Z_R Z_0 \omega_r^3 C_c^2}{\pi}. \tag{3.6}$$

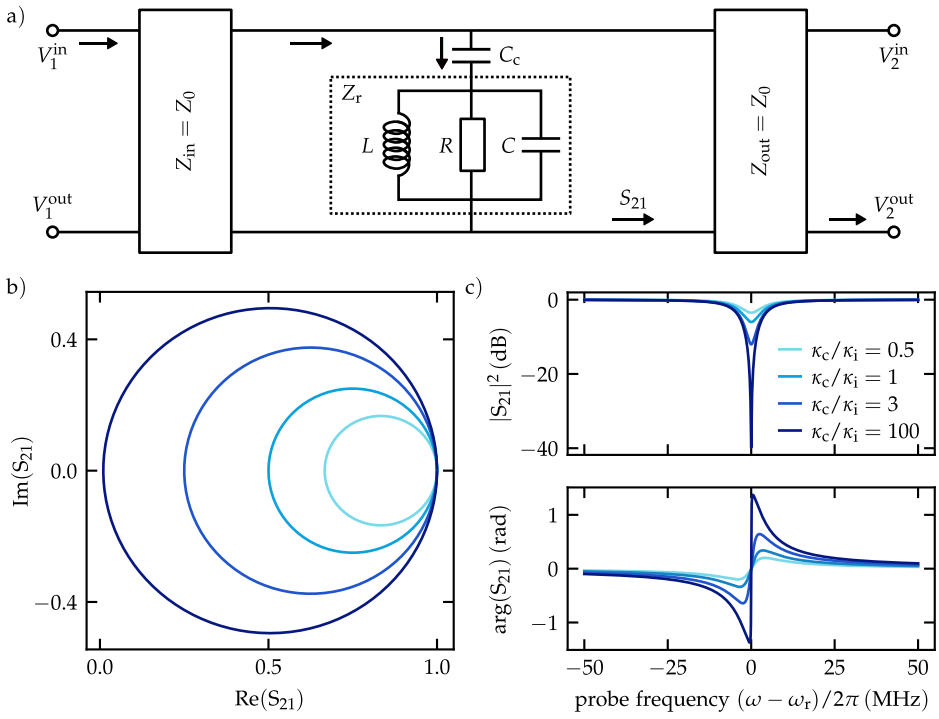


**Figure 3.1: Microwave response of a capacitively coupled notch-type resonator. a)** Schematic diagram of a two-port microwave network with a resonator load impedance $Z_R$ shunting the two conductors of a continuous transmission line. The in- and output-impedance of the transmission line is matched to the measurement lines ($Z_0 = 50\,\Omega$). Inserting the total resonator impedance into Eq. 3.3 yields the transmission $S_{21}^{reso}$ from port $V_1^{in}$ to port $V_2^{out}$, as given by Eq. 3.8. **b)** In the complex plane, the transmission parameter describes a circle starting and ending at $S_{21}$=1. The circle diameter approaches unity as $\kappa_c/\kappa_i \to \infty$. **c)** The amplitude of the transmitted signal forms a Lorentzian dip and the phase has a maximum roll off from $-\pi/2$ to $\pi/2$.

As expected, the coupling loss is proportional to the coupling capacitance. By adding up the different contributions, the total loss rate of the resonator can be defined as

$$\kappa_r = \kappa_i + \kappa_c = \omega_r \tan(\delta), \tag{3.7}$$

which is equal to the full width at half maximum of the resonance. Note that for comparing different resonators, the frequency independent loos tangent $\tan(\delta)$ (or quality factor $Q = 1/\tan(\delta)$) is typically introduced.

Combining Eq. 3.3 to 3.7 yields [162]

$$S_{21}^{reso} = 1 - S_{11}^{reso} = 1 - \frac{\kappa_c}{\kappa_r + 2i(\omega - \omega_r)} \tag{3.8}$$

for the complex transmission coefficient for the microwave network. As shown in Fig. 3.1b, $S_{21}^{\mathrm{reso}}$ corresponds to a circle in the complex plane, which is located at $1 - \kappa_c/2\kappa_r$ and has a diameter $\kappa_c/\kappa_r$. The corresponding amplitude signal $|S_{21}^{\mathrm{reso}}(\omega)||^2$ has a Lorentzian shape (Fig. 3.1c). All resonators investigated in this work are over coupled ($\kappa_c > \kappa_i$), meaning most energy is lost via $C_c$. This results in a large resonance circle and thus an overall strong resonator signal.

## 3.2 Asymmetric resonances

The derivation above and the resulting formula for the resonator transmission 3.8 are only valid if the impedances of the transmission line and the input and output ports are matched ( $Z_{\mathrm{in}} = Z_{\mathrm{out}} = Z_0$). In reality, however, this is usually not the case and asymmetric lineshapes can occur, e.g., due to an impedance mismatch between the sample holder PCB and the on-chip microstrip line (see Sec. 4.2.3).

Physically, this corresponds to a standing wave on the chip, which can be well approximated by a cavity with a low-Q mode [146, 163]. Then, one has to consider the case of two cavities coupled to each other, one ($\omega_r$) being the resonator and the other ($\omega_t$) being the transmission line. The Hamiltonian for this system is

$$\mathcal{H} = \hbar\omega_r \hat{r}\hat{r}^\dagger + \hbar\omega_t \hat{t}\hat{t}^\dagger + \hbar\Omega(\hat{r}\hat{t}^\dagger + \hat{t}\hat{r}^\dagger), \tag{3.9}$$

where $\hat{r}$ and $\hat{t}$ are the photon creation operators of the corresponding cavities and $\Omega$ is the coupling rate. The field transmission trough such a (quantum) system can be calculated via the input-output formalism developed by Collett and Gardiner [164], as sketched in the following.

Considering $\hat{t}_{1,\mathrm{in}}$ and $\hat{t}_{2,\mathrm{out}}$ as the input and output fields at the respective port of the transmission line cavity, one can write the quantum-mechanical Langevin equations of the corresponding mode as [146]

$$\frac{d}{dt}\hat{t} = -i\omega\hat{t} = -\frac{i}{\hbar}[\hat{t}, \mathcal{H}] - \frac{\kappa_t}{2}\hat{t} + \sqrt{\frac{\kappa_t}{2}}\hat{t}_{1,\mathrm{in}} + \sqrt{\frac{\kappa_t}{2}}\hat{t}_{2,\mathrm{in}} \tag{3.10a}$$

and

$$\frac{d}{dt}\hat{t} = -i\omega\hat{t} = -\frac{i}{\hbar}[t, \mathcal{H}] + \frac{\kappa_t}{2}\hat{t} - \sqrt{\frac{\kappa_t}{2}}\hat{t}_{1,\mathrm{out}} - \sqrt{\frac{\kappa_t}{2}}\hat{t}_{2,\mathrm{out}}, \tag{3.10b}$$

where $\kappa_t$ is the coupling to the input and output ports, which, for simplicity but without loss of generality, is assumed to be symmetrical. In practice, $\kappa_t \gg \kappa_r$ is the

linewidth of the transmission line mode. Assuming only one input field ($\hat{t}_{1,\mathrm{in}} = 0$) and using the commutation relation for bosonic operators yields

$$\hat{t} = \frac{\sqrt{2\kappa_\mathrm{t}}\hat{t}_{1,\mathrm{in}} - 2i\Omega\hat{r}}{\kappa_\mathrm{t} - 2i(\omega - \omega_\mathrm{t})} \tag{3.11a}$$

and

$$\hat{t} = \frac{2\kappa_\mathrm{t}\hat{t} - \sqrt{2\kappa_\mathrm{t}}\hat{t}_{1,\mathrm{in}} + \sqrt{2\kappa_\mathrm{t}}\hat{t}_{2,\mathrm{out}} + 2i\Omega\hat{r}}{\kappa_\mathrm{t} + 2i(\omega - \omega_\mathrm{t})}. \tag{3.11b}$$

For the second equation, the boundary condition $\hat{t}_{1,\mathrm{in}} + \hat{t}_{1,\mathrm{out}} = \hat{t}\sqrt{\kappa_\mathrm{t}/2}$ was used. For the resonator, it is sufficient to consider only a single port, which serves as a loss channel ($c_\mathrm{in} = 0$) with loss rate $\kappa_\mathrm{r}$. Solving the Langevin equations for the resonator mode then yields

$$\hat{r} = \frac{-2i\Omega\hat{t}}{\kappa_\mathrm{r} - 2i(\omega - \omega_\mathrm{r})}. \tag{3.12}$$

Combining the equations above and solving for $\hat{t}_{2,\mathrm{out}}$, the transmission parameter can be written as [146]

$$S_{21}^{\mathrm{reso}} = \frac{\langle\hat{t}_{2,\mathrm{out}}\rangle}{\langle\hat{t}_{1,\mathrm{in}}\rangle} = \frac{\kappa_\mathrm{t}/2}{\frac{\kappa_\mathrm{t}}{2} + i(\omega - \omega_\mathrm{t}) + \frac{\Omega^2}{\kappa_\mathrm{r} + i(\omega - \omega_\mathrm{r})}}. \tag{3.13}$$

It will become apparent in section 6.3 that the input-output formalism is a powerful tool to study also more complicated Hamiltonians. For the system described by Eq. 3.9 (Fig. 3.2(a)), the complex transmission can also be calculated by means of conventional network theory. Using a Norton equivalent circuit, Khalil *et.al.* showed that a complex coupling rate $\hat{k}_\mathrm{c} = |\kappa_\mathrm{c}|e^{i\Phi}$ can account for the impedance mismatch and found a equivalent expression for Eq. 3.13 that reads [165]

$$S_{21}^{\mathrm{reso}} = 1 - \frac{\kappa_\mathrm{c}e^{i\Phi}}{\kappa_\mathrm{r} + 2i(\omega - \omega_\mathrm{r})}. \tag{3.14}$$

Here, $\kappa_\mathrm{r} = \kappa_\mathrm{i} + \kappa_\mathrm{c}$ as above and $\kappa_\mathrm{c} = \mathrm{Re}(\hat{k}_\mathrm{c}) = 4\Omega^2/(\omega_\mathrm{r}\kappa_\mathrm{t})$ [146]. As shown in Fig. 3.2(b), the complex phase of $\hat{k}_\mathrm{c}$ corresponds to a rotation of the circle around the origin by an angle $\Phi$. Note that the diameter of the rotated circle is $|\hat{k}_\mathrm{c}|/\kappa_\mathrm{r}$ rather then $\mathrm{Re}(\hat{k}_\mathrm{c})/\kappa_\mathrm{r}$, and simply rotating the circle back on the real axis would therefore yield an incorrect result for $\kappa_\mathrm{i}$ [165].

When fitting Eq. 3.14 to real data, it is necessary to adept the formula to the experimental setup. Introducing additional prefactors that accounts for phase offset ($\alpha_0$) and the net attenuation and amplification ($a$), the final expression for

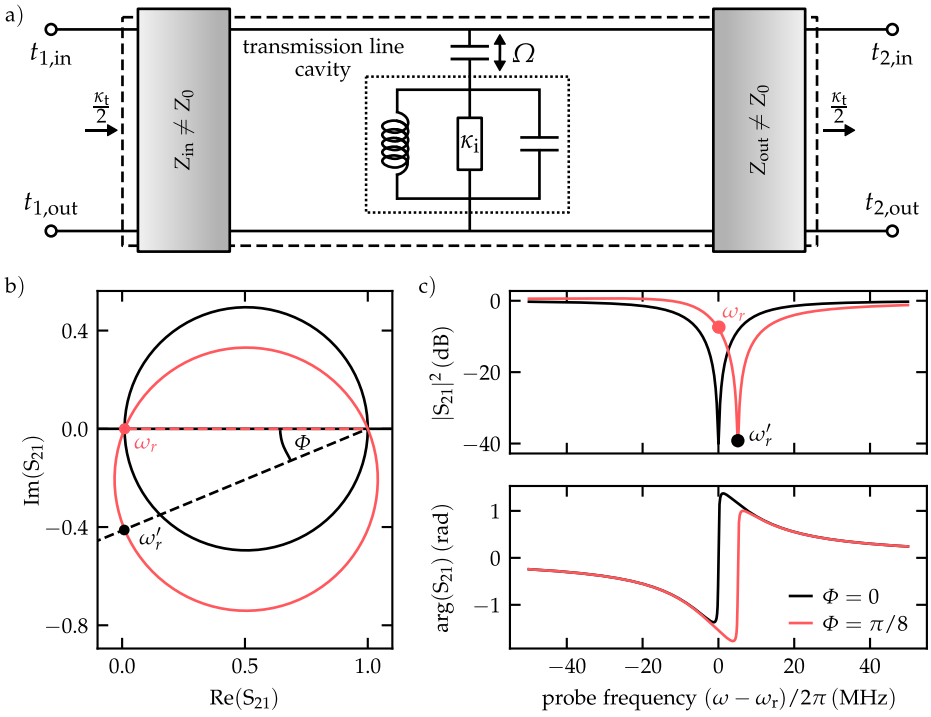


**Figure 3.2: Microwave network of a resonator with asymmetric response. a)** Schematic diagram of a two-port microwave network with a resonator load and a impedance mismatched transmission line ($Z_{\mathrm{in}} \approx Z_{\mathrm{out}} \neq Z_0$). The latter can be modeled by a single mode cavity that couples to the resonator with rate $\Omega$. The transmission of this network can be calculated via the input-output formalism, which connects the quantum dynamics of the circuit with the coupling rate $\kappa_t$ to the input and output ports (Eq. 3.13), or by means of conventional network theory (Eq. 3.14). **b)** Quantitatively, the impedance mismatched transmission line can be accounted for by a complex coupling rate $\hat{\kappa_c} = \kappa_c e^{i\Phi}$, which manifest in a rotation of the resonance circle by an angle $\Phi$ and a increase of the diameter by $\kappa_c/\mathrm{Re}(\kappa_c) = \csc(\Phi)$. **c)** Looking at the amplitude signal, the resonance frequency $\omega_r$ is no longer equal to the point of minimal transmission, i.e, the "center" of the resonance dip. Consequently both, the amplitude and phase signal, are asymmetric around the resonance.

the transmission coefficient of a resonator coupled to a mismatched tranmission line is [166]

$$S_{21}^{\text{reso}} = ae^{i\alpha_0}\left(1 - \frac{\kappa_c e^{i\Phi}}{\kappa_r + 2i(\omega - \omega_r)}\right). \tag{3.15}$$

This formula was used throughout this work to fit the resonator transmission in order to determine $\omega_r$ and $\kappa_i = \kappa_r - \kappa_c$

## 3.3 Bifurcation

In granular aluminum resonators, where kinetic inductance ratio (Eq. 3.15) usually approaches unity, the resonance behaviour is dominated by $L_k^{\square}$. At high measurement powers, where the resonator currents become increasingly large, the nonlinearity of the kinetic inductance (Eq. 2.23) thus has a significant influence on the resonator frequency. In particular, sweeping the measurement frequency $\omega$ through the resonator gives rise to classic Duffing oscillator dynamics [167].

In order to quantitatively understand this behavior, it is necessary to incorporate the resonance shift $\delta\omega_r = \omega_r - \omega_{r,0}$ due to the nonlineaer kinetic inductance into Eq. 3.15. For a kinetic inductance fraction $\alpha = 1$, the nonlinear frequency shift is given by [168]

$$\frac{\delta\omega_r}{\omega_{r,0}} = -\frac{1}{2}\frac{\delta L_k^{\square}}{L_k^{\square}} = -\frac{1}{2}\frac{I}{I_c} = -\frac{1}{2}\frac{E_{\text{tot}}}{E_c}, \tag{3.16}$$

where $I_c$ is the critical current and $E_c$ is on the order of the superconductor's condensation energy. The total energy $E_{\text{tot}}$ generally depends on the number of photons $\overline{n}$ in the resonator. However, it can also be related to the power dissipated in the resonator via Eq. 3.5. In the steady state power is conserved and therefore

$$P_{\text{loss}} = P_{\text{in}} - P_{\text{out}} = P_{\text{in}}\left(1 - |S_{11}|^2 - |S_{21}|^2\right), \tag{3.17}$$

where $P_{\text{in}}$ and $P_{\text{out}}$ are the resonator in- and output power, respectively. Ignoring impedance mismatch of the transmission line and recalling that $S_{21} = 1 - S_{11}$, one can combine Eq. 3.17 and 3.15 to find [168]

$$P_{\text{loss}} = P_{\text{in}}\left(\frac{2\kappa_c\kappa_i}{\kappa_r^2 + 4(\omega - \omega_r)^2}\right). \tag{3.18}$$

Here, $\omega_r$ is the unperturbed resonator frequency in the low power limit. With this expression and the definition of the internal loss rate (3.5), the frequency shift due to the kinetic inductance can be written as

$$\delta\omega_r = -\frac{2\kappa_c\omega_{r,0}}{\kappa_r^2 + 4(\omega-\omega_r)^2}\frac{P_{in}}{E_c} = \frac{\hbar\omega_r^3\overline{n}}{1+4(\omega-\omega_r)^2/\kappa_r^2}\frac{\omega_{r,0}}{E_c}. \tag{3.19}$$

where in the last step an expression for the average photon number on resonance

$$\overline{n} = \frac{2P_{in}}{\hbar\omega_r^3}\frac{\kappa_c}{\kappa_r^2} \tag{3.20}$$

was used. The consequence of the inverse dependence of $\delta\omega_r$ on the detuning $\omega-\omega_r$ in Eq. 3.19 can conceptional be understood as follows: Starting at frequencies below the resonance, the resonator currents increase as the detuning decrease. As a consequence, the nonlinear inductance causes the resonator to shift to lower frequency, increasing the currents even further. This results in a positive feedback loop that abruptly ends when the resonator jumps past the readout frequency to an point of equivalent input power on the other side of the resonance (see Fig. **??**). There, the feedback is no longer positive and the resonator drifts back to its original position. This behavior is usually referred to as bifurcation. In this regime, the expression for the transmission coefficient in Eq. 3.15 is no longer valid. Thus, for practical applications, resonators with a high kinetic inductance should be probed with low power signals (small average photon number). Note that the exact power where bifurcation becomes significant naturally depends on the magnitude of the kinetic inductance (Eq. 3.16)

# 4 Experimental methods

The experimental means used for the fabrication and measurements of the granular aluminum resonator samples are summarized in this chapter. First, details on the deposition and pattering processes are given and different methods for determining the sheet resistance of granular aluminum are compared. Second, the various components of the experimental setup are described, including a cryogenic refrigerator, DC and RF components and wiring as well as an appropriate housing for the studied samples. Next, methods for measuring and evaluating noise in superconducting resonators are outlined. Finally, electric field simulations of the resonator and the sample holder electrode are provided.

## 4.1 Sample design and fabrication

Experiments with superconducting quantum circuits require growing and pattering of appropriate films. Most of the techniques used in this process are adapted from the semiconductor industry and therefore well established. The samples measured in the context of this thesis were partially fabricated with commercial equipment available in the KIT Nanostructure Service Laboratory and partially with homemade tools.

### 4.1.1 Thin film preperation

In the first step of the sample preparation, a granular aluminum thin film is deposited on a 430 µmsapphire substrate using a reactive DC magnetron sputtering processes. The substrate is placed in a vacuum chamber filled with argon working gas, facing a ultra pure aluminum cathode surrounded by a ring shaped anode. When very high voltages on the order of hundreds of volts are applied between anode and cathode, free electrons start to flow and ionize the argon atoms, i.e., a plasma is ignited. The positively charged argon ions reach the aluminum target at very high velocity, removing cluster of aluminum atoms that evaporate towards the substrate. To increase the sputtering rate, magnets are placed behind the cathode

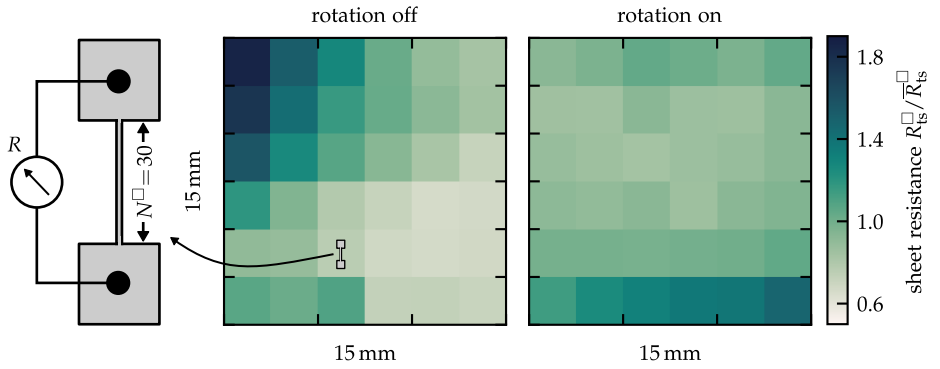


**Figure 4.1: Homogeneity of granular aluminum thin-films at room temperature.** Spatial distributions of the normal state sheet resistance $R_{\mathrm{n}}^{\square}$ for two 20 nm granular aluminum films deposited on $15 \times 15\,\mathrm{mm}^2$ chips with and without rotation. The sheet resistance $R/N^{\square}$ is determined by measuring the total resistance $R$ of the displayed test structure ($N^{\square} = 30$) at each spatial position. In samples that are not rotated during deposition there is a noticeable resistance gradient between two of the opposing corners.

to confine the plasma electrons on a spiral track close to the surface of the sputter target [169].

In order to grow granular films, oxygen gas is added to the chamber during the sputtering process. Then, some of the free aluminum atoms are oxidized into $\mathrm{AlO}_x$, while others form grains with a natural oxide barrier on the substrate, resulting in the peculiar structure detailed in section 2.2. If the partial pressure of the oxygen gas is increased, more oxygen gets implanted. As a consequence, the oxygen barriers in the granular film will be less transparent and the resistivity higher [3].

For the further processing, it is desirable to have a very homogeneous sample, such that circuits elements have comparable and also predictable properties. Because the sputter process is dynamic, gases are not necessary equally distributed within the chamber, and some regions of the sample are either lesser oxidized or thinner. To tackled this problem, a step motor was used to slowly rotate the substrate during deposition. The effectiveness of this approach was tested by measuring 36 dumbbell-shaped test structures made from the same granular aluminum film, equally distributed over a $15x15\,\mathrm{mm}^2$ area in the center of the chip.[1] Each test structure consists of two contact pads connected by a 5 µm wide and 150 µm long

[1] The total size of the sapphire substrate is $20x20\,\mathrm{mm}^2$, but the edges are neglected because they can not be processed properly. The $15x15\,\mathrm{mm}^2$ center area is typically cut into nine (identical) $5x5\,\mathrm{mm}^2$ chips

constriction, giving a total of $N^{\square} = 30$ squares of material (Fig. 4.1). The resistance between the pads is measured with a probe station at room temperature. Then, the sheet resistance of the film at the position of the test structure is determined by dividing this resistance value by the number of squares, $R_{\mathrm{ts}}^{\square} = R_{\mathrm{probe}}/30$. As shown in Fig. 4.1, the film grown under rotation is much more homogeneous, while the other sample shows a noticeable resistance gradient towards two corners.

The test structures described above are patterned with the same lithography methods as the microstrip resonator circuit employed throughout this work: After a thin film of granular aluminum was sputter deposited on a sapphire substrate, the whole film is covered with AZ5214 resist and the desired structures are defined by optical exposure through a chromium hard mask. Subsequently, the areas of the film not covered by the resist are removed by an argon-chlorine based inductively coupled plasma (ICP) dry etching process (see Appendix A for details on the fabrication parameters). Because the high kinetic inductance of granular aluminum is not necessarily wanted for the feedline, it is shunted with pure aluminum using a liftoff process. Finally, the backside of the substrate is coated with a thin layer of superconducting niobium in order to have a clean, well defined ground. [2]

### 4.1.2 Sample parameters

The results presented in this work were obtained from measurements on a total of thirteen resonators, distributed over five different samples: three samples (A-C) that only differ in the sheet resistance (and thickness) of the granular aluminum films, and two samples (D+E) that were fabricated as a stack of two layers with different sheet resistances. There, the lower layer has a $R_{\mathrm{n}}^{\square}$ well below $R_0 = 6.4\mathrm{k}\Omega$ and therefore becomes superconducting. The top layer has $R_{\mathrm{n}}^{\square} \gg R_0$ and instead becomes insulating below $T_{\mathrm{c}}$. One can easily achieve such a two layer structure by instantly increasing the oxygen partial pressure half way through the evaporation process.

Together, all samples host a total of thirteen ultra-compact $\lambda/2$ resonators with lengths between $300\,\mu\mathrm{m} - 500\,\mu\mathrm{m}$ at a constant width of $2\,\mu\mathrm{m}$. They are placed in the vicinity of a single, $280\,\mu\mathrm{m}$ wide transmission line running straight trough the center of the chip (compare Fig 4.2). The dominant coupling between the resonators and the transmission line is capacitive and chosen such that $\kappa_{\mathrm{c}}/\kappa_{\mathrm{i}} \ll 1$ ($\kappa_{\mathrm{r}} \sim \kappa_{\mathrm{c}}$).

[2] Niobium was chosen for the backside metallization over aluminum because it further suppresses quasiparticle dissipation due to a higher $T_{\mathrm{c}}$.

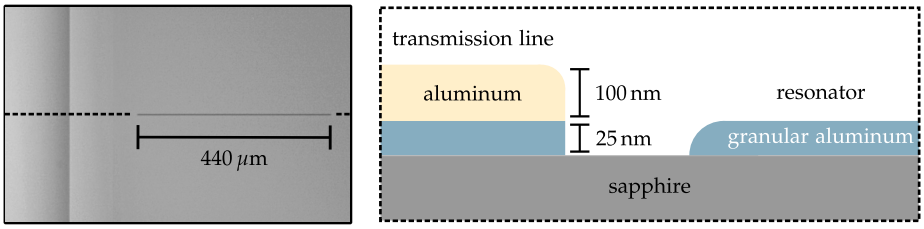


**Figure 4.2: Sample layout and structure**. Right panel: Optical photograph of a single 2 µm wide and 440 µm long resonator, capacitively coupled to the global on-chip transmission line. Right panel: Sketch of the sample cross-section. For the transmission line, the granular aluminum film is shunted by a pure aluminum layer to achieve a 50 Ω matching.

The thickness of all granular aluminum films is on the order of the coherence lenght ($\xi_{GL} \approx 10\,\text{nm} \sim t_z$ [34]), which places them in the two dimensional limit.

The frequency of the resonators predominantly depends on the kinetic inductance and therefore, on the sheet resistance (Eq. 2.17) of the film. As mentioned above, the resistance can be controlled by the oxygen partial pressure during the sputtering process. However, for large sheet resistances $R_n^{\square} > 1\,\text{k}\Omega$, the dependence of the sheet resistance on the oxygen partial pressure is exponential, which is problematic for the controllability and reproducibility, since small variations in humidity or temperature have a significant impact.

To make the process more controllable, both film thickness $t_z$ and the resistance $R_{sc}$ are monitored during the film deposition [100]. The former is measured via a quartz oscillator that is placed in close vicinity to the sample. If material is deposited on the quartz, its frequency changes proportional to the additional mass. The corresponding conversion factor can be calibrated using a profilometer. To monitor the resistance, thin stripes of silver are applied to two sides of the sapphire substrates prior to the evaporation of the granular aluminum films. These stripes are contacted via metallic clamps when the substrate is mounted in the sputter chamber.

Figure 4.3(a) shows the thickness and sheet resistance of sample B, measured during the deposition of the granular aluminum film. Above a critical thickness of a few nanometers the resistance $R_{sc}^{\square}$ of the sample can be described by a model for fine-grained polycrystalline thin films [170], trough which the final resistance at the desired thickness can already be estimated. By adjusting the oxygen pressure, the final resistance can thus still be influenced during deposition. Note that due to the quadratic shape of the sample, the measured resistance is approximately the sheet resistance, i.e., $R_{sc}^{\square} \approx R_{sc}$. While this gives a good estimated for the sheet resistance of the resonators, the measured value is influenced by the contact

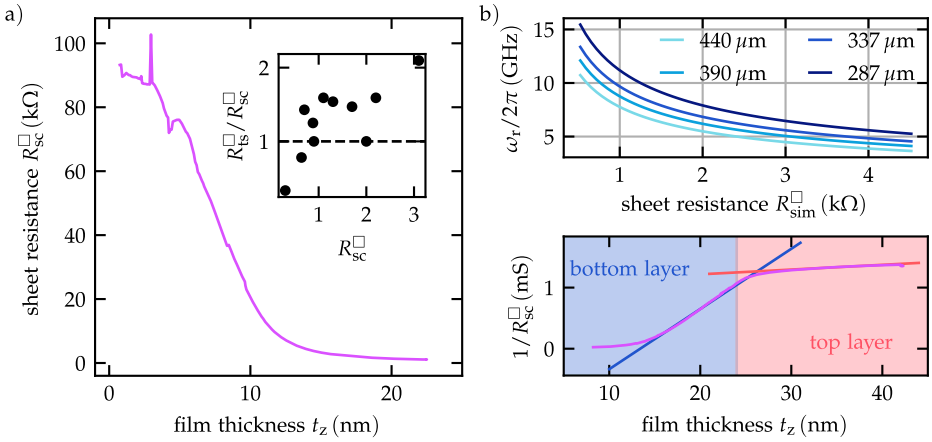


**Figure 4.3: Different methods for determining the sheet resistance of granular aluminum films.** **a)** *In situ* measurement of the sheet resistance during the sputter deposition. The inset shows, for different samples, the ratio between the resistance value $R_{sc}^{\square}$ extracted from the *in situ* measurement and the sheet resistance obtained from averaging over different on-chip test structures $R_{ts}^{\square}$ (see Fig. 4.1). **b)** Simulated resonance frequencies as a function of the normal state sheet resistance for resonators of different lengths. Comparing the measured to the simulated resonance frequencies yields a sheet resistance value $R_{sim}^{\square}$ for each individual resonator. **c)** Measured conductance curve for sample E, which consist of two granular aluminum layers. The ratio between the slope at the bottom (blue line) and the slope at the top (red line) layer is used to estimate the sheet resistance of the top layer from Eq. 4.1.

resistance between the film and the silver stripes as well as the conductance through the plasma.

A better estimate can be obtained from test structures (Fig. 4.1(a)) distributed over the chip after the film was processed optically. There, the increased number of squares gives additional statistical confidence and the contact resistance is neglectable. Indeed, a comparison between the average sheet resistance measured over different test structures $R_{ts}^{\square}$ and the corresponding resistance values obtained from the sputter chamber $R_{sc}^{\square}$ (inset of Fig 4.3(a)) reveals a noticeable discrepancy for multiple samples.

However, due to unavoidable inhomogeneities on the sub millimeter lenght-scale the exact sheet resistance of the resonator structures can also deviate from the test structure values. Therefore, a 3D planar high-frequency electromagnetic software (SONNET) is employed to compare the measured resonator frequencies $\omega_r$ with simulations of geometrically identical resonators with different sheet resistances $R_n^{\square}$ (Fig 4.3(b)). Finding the value where the simulated and measured resonance frequency agrees yields a good estimate for $R_n^{\square}$ of the particular resonator.

**Table 4.1:** Geometry (lenght $l_y$, film thickness $t_z$, constant width $w_x = 2\,\text{nm}$) and thin film properties for all measured resonators with a fundamental resonance frequency $\omega_r$. The sheet resistance of the film $R_n^\square$ can be obtained from test structures ($R_{ts}^\square$, averaged over chip) or simulations ($R_{sim}^\square$). If two values are stated, they correspond to the (superconducting) bottom and (insulating) top layer, respectively.

| Reso. | $\omega_r/2\pi$ (GHz) | $l_y$ (µm) | $t_z$ (nm) | $R_{ts}^\square$ (kΩ) | $R_{sim}^\square$ (kΩ) | $L_{k,sim}^\square$ (nH) |
|---|---|---|---|---|---|---|
| A1 | 10.565 | 406 | 25 | 0.5 | 0.59 | 0.45 |
| A2 | 10.740 | 390 | 25 | 0.5 | 0.61 | 0.47 |
| B1 | 5.494 | 505 | 22 | 1.4 | 1.39 | 1.05 |
| B2 | 6.154 | 440 | 22 | 1.4 | 1.49 | 1.14 |
| B3 | 6.793 | 390 | 22 | 1.4 | 1.53 | 1.17 |
| C1 | 4.069 | 406 | 30 | 3.5 | 3.97 | 3.03 |
| C2 | 4.663 | 337 | 30 | 3.5 | 4.32 | 3.30 |
| C3 | 5.780 | 287 | 30 | 3.5 | 3.76 | 2.87 |
| D1 | 8.006 | 505 | 24+18 | 0.9 | 0.65+12 | 0.5 |
| D2 | 9.010 | 440 | 24+18 | 0.9 | 0.69+12 | 0.53 |
| D3 | 9.995 | 390 | 24+18 | 0.9 | 0.71+12 | 0.54 |
| E1 | 7.839 | 505 | 23+17 | 0.9 | 0.68+190 | 0.52 |
| E2 | 8.872 | 440 | 23+17 | 0.9 | 0.72+190 | 0.55 |

For sample D and E, only the resistance of the superconducting bottom layer can be determined from simulations. The resistance of the top layer is extracted from the conductance vs. thickness curves measured during the sputter process. After fitting a straight line to the curve before and after changing the oxygen pressure (Fig. 4.3(c)), the resistance of the top layer can be calculated as

$$R_{top}^\square = \frac{m_{btm}}{m_{top}} R_{btm}^\square = \frac{m_{btm}}{m_{top}} R_{sim}^\square \tag{4.1}$$

where $m_i$ is the slope of the line corresponding to respective layer. Note that the transition from the superconducting to the insulating film is fluent rather then abrupt and the result of Eq. 4.1 strongly depends on the data segments chosen for the two fits. Therefore, the resistance values that can be obtained for the top layer are only a rough estimate.

The geometric characteristics of all granular aluminum resonators are listed in Table 4.1. Further properties of the films can be calculated from the resistivity $\rho = R_{sim}^\square t_z = R_n^\square t_z$ of the film. An estimate for the London penetration depth at low temperatures $T \ll T_c(\rho) \approx 2\,\text{K}$ is given by $\lambda_L \approx 1.05 \times 10^{-3}\sqrt{\rho/2} = 4.5 \pm 2.1\,\mu\text{m}$ [171]. This means that the films ($t \ll \lambda_L$) are transparent for AC and magnetic fields and the currents flow through the entire film when the resonator oscillates.

The penetration depth of DC electric fields it much more difficult to estimate due to the granular structure of the film, which is partly a dielectric. However, the lower limit should be given by the Thomas-Fermi length of a clean superconductor with similar properties. Such calculations yield $\lambda_{\mathrm{TF}} \approx \sqrt{2\lambda_{\mathrm{L}}^2 E_{\mathrm{F}}^* / (3c^2 m_{\mathrm{e}}^*)} = 2.1 \pm 0.1\,\mathrm{nm}$, which is on the order of the grain size. Here $E_{\mathrm{F}}^* \propto \rho^{-0.7}$ and $m_{\mathrm{e}}^* \propto \rho^{0.44}$ are the effective Fermi Energy and charge carrier mass as defined in Ref. [98], respectively. From $\lambda_{\mathrm{L}}$, on can also estimate the superconducting charge carrier density of the granular films $n_{\mathrm{s}} = m_{\mathrm{e}}^* / (2\mu_0 e^2 \lambda_{\mathrm{L}}^2) = (4.85 \pm 1.76) \times 10^{24}\,\mathrm{m}^{-1}$, which is orders of magnitude below pure aluminum.

One of the few available indicators for the degree of disorder in a thin film is the Ioffe-Regel parameter [172]

$$k_{\mathrm{F}} l = \hbar (3\pi^2)^{2/3} / (e^2 \rho n_{\mathrm{n}}^{1/3}), s \tag{4.2}$$

where $n_{\mathrm{n}}$ is the number of charge carries in the normal state, $l$ is the mean free path and $k_{\mathrm{F}}$ is the radius of the Fermi sphere. As pointed out in Ref. [173], superconductivity in granular aluminum is destroyed due to disorder for a critical value of $(k_{\mathrm{F}} l)_{\mathrm{c}} \sim 0.01$. Materials where disorder predominantly occurs on the atomic scale usually do no longer become superconducting below $(k_{\mathrm{F}} l)_{\mathrm{c}} \approx 1$. Using $n = 1/(\mu_{\mathrm{H}} \rho e)$, where $\mu_{\mathrm{H}} \propto \rho^{-0.5}$ is the Hall mobility of granular aluminum [96], yields values ranging from 0.14 to 0.8, meaning all films are highly disordered. Thus, one can expect the mechanisms described in Sec. 2.2.2 and Sec. 2.1.2 to become experimentally relevant.

## 4.2 Measurement environment

Superconducting quantum circuits have to be operated at cryogenic temperatures for two main reasons. First, the sample needs to be cooled down below the transition temperature $T_{\mathrm{c}}$ to enable the desired effects of superconductivity, including a (almost) dissipationless AC current. Second, the temperature of the system should be lower then all relevant energy scales, i.e., the resonator frequencies, to be able to observe quantum effects. Commercial cryostats reach base temperatures on the order of a few millikelvin, which places a physical lower limit for the resonator frequencies of about $1\,\mathrm{GHz} = 50\,\mathrm{mK}$. At the same time, the energy stored in the resonator should not be sufficient to break Cooper pairs into quasiparticle, meaning the resonator frequency must be well below the superconducting gap of (granular) aluminum $\Delta \sim 40\,\mathrm{GHz} - 80\,\mathrm{GHz}$. As a consequence, superconducting quantum circuits are typically operated in the microwave regime between $2\,\mathrm{GHz} - 20\,\mathrm{GHz}$.

Besides the physical motivation, this also has a rather practical reason: Components suitable for the microwave regime are commercially available.

### 4.2.1 Cryogenic setup

The low temperature experiments presented in this work were performed in a *Bluefors LD250* $^3$He/$^4$He dilution cryostat. Figure 4.4(b) illustrates the working principle of this multi stage cooling unit [174]. To pre-cool the cryostat to a few kelvin, a mechanical two stage pulse tube is used. [3] The advantage of this cryocooler is that all moving parts can be installed at roomt temperature and away from the fridge, such that vibrations do not interfere with the experiments.

In order to reach temperatures in the mK regime, a mixture of $^4$He and $^3$He is used as additional coolant. The mixture is continuously circulated in a closed cooling cycle where a Joule-Thomson valve further reduces its temperature via isenthalpic expansion. Below $\sim$ 870 mK, the mixture undergoes a spontaneous transition separating into two liquid phases that accumulate in the mixing chamber: A $^3$He rich phase with low density floats on top of a dilute phase with $\sim$ 7% $^3$He admixture, where the $^3$He atoms move through the superfluid $^4$He with nearly no resistance. On the still stage ($\sim$ 700 mK) the isotopes of the dilute phase are separated by thermal evaporation of $^3$He, which has a boiling point well below that of $^4$He. Using a turbomolecular pump, the $^3$He is extracted from the still and briefly pumped to room temperature, where it is cleaned by a cold trap before reentering the fridge. To compensate for the evaporated molecules, $^3$He of the rich phase has to flow to the diluted phase. The latent heat of this mixing process cools the cryostat.

In practice, cooling powers of about 10 µW can be reached, which allows for a base temperature of $\sim$ 10 mK. Limiting factors are the thermal connection between adjacent stages, heat input through the mixture and thermal radiation. The latter is suppressed by installing metallic shields at each stage. Additionally, the cryogenic chamber is evacuated to $\sim 10^{-6}$ mbar during the cool down process, which avoids direct heat transfer trough gas molecules. When cold, the fridge itself serves as a sufficient pump by trapping gases on its cold surfaces.

[3] An alternative are so-called 'wet' cryostats, where reservoirs of liquid nitrogen and $^4$He are used for pre-cooling. However, due to the additional effort necessary for their operation, such systems are less popular nowadays

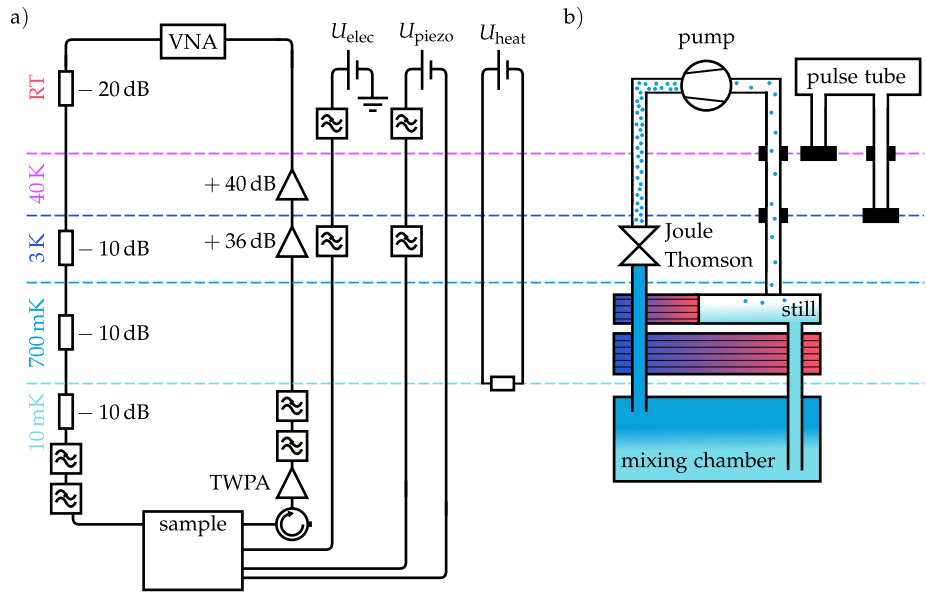


**Figure 4.4: Experimental and cryogenic measurement setup a)** Schematic containing all instruments, microwave components and wiring used in the spectroscopy measurements. The sample transmission $S_{21}$ is probed using a vector network analyzer (VNA), whose signal is attenuated before and amplified after the sample. Low pass filters are used to protect the quantum circuit from high energy radiation. Three independent voltage sources enable control over additional experimental parameters (see text for details). **b)** All experiments are performed inside a commercial dry dilution cryostat. A two stage pulse tube is used to pre-cool the system. A mixture of $^4$He and $^3$He circulating in a closed cooling cycle produces latent heat through the continuous phase transition of $^3$He molecules inside the mixing chamber, resulting in base temperatures down to 10 mK.

### 4.2.2 Microwave setup

All resonator experiments presented in this work rely on measuring the microwave transmission through the sample (Section 3). Experimentally, this task is fulfilled by a vector network analyzer (VNA), which generates a single-frequency microwave signal at its output-port and reference its amplitude and phase to the signal received at the input-port. By rapidly sweeping the frequency of the signal, this allows direct probing of the $S_{21}(\omega)$ parameter of a two-port network.

Coaxial cables guide the microwave signal from the VNA to the sample mounted at the base temperature of the cryostat (Fig. 4.4a)). To avoided heat transfer into the cryostat, these cables are made of a metal with a low thermal conductivity, e.g., stainless steel. To reduce the high power signal of the VNA to the few photons

necessary for probing quantum effects in superconducting circuit, attenuators are installed throughout the microwave lines. To manage the thermal load, they are distributed over various temperature stages. Each of them adds Johnson-Nyquist noise to the signal, which results in a final noise temperature

$$T_{\mathrm{n}} = T_1 + \sum_{i=1}^{N} \frac{T_{i+1}}{\prod_i^{j=1} a_j}, \tag{4.3}$$

where $T_i$ is the temperature of the $N$th stage ($T_1 = 10\,\mathrm{mK}$) and $a_j$ is the corresponding attenuation factor. According to Eq. 4.3, electronic noise is dominated by the temperature of the base, which is a another reason to keep it as low as possible. Together with the damping of the superconducting cables (Appendix B), the total attention of the cold cryostat sums up to $\sim 70\,\mathrm{dB}$ at 8 GHz, reducing the photon number by a factor of ten million. Before and after the sample, additional commercial (18 GHz cutoff) and home made low pass filter are installed to suppress parasitic, high-energy infrared radiation which is not filtered by the PTFE dielectric inside the attenautors and coaxial lines.

To be measurable by room temperature electronics, the output signal of the sample passes through an amplification chain on its way back to the VNA. The first amplifier, installed at base temperature, is a quantum-limited traveling-wave parametric amplifier (TWPA) [175]. It adds about $15 - 20\,\mathrm{dB}$ amplification at a very low noise level.[4] At 4 K and 70 K, two high-electron-mobility transistors (HEMT) are mounted to amplify the signal further.

### 4.2.3 Sample housing

The $5 \times 5\,\mathrm{mm}^2$ chips are installed in a custom-made, two piece copper sample holder (Fig. 4.5). There, SMP connectors feed the signal from the microwave lines to microstrip PCBs which are wire-bonded to the ends of the on-chip transmission line. Instead of gluing the chip to the sample holder, which is the most common method, it is fixated with four clamps, one at each corner. This allows the sample to be bent, which is useful for the investigation of two level defects [176].

For this purpose, a voltage controlled piezo-actuator is placed at the bottom of the sample holder by a custom made, H-shaped mount. A hole in the sample holder allows for contact between the piezo and the sample backside through a

[4] An additional microwave line is necessary to drive the TWPA, which is not shown in the sketch of the setup (Fig. 4.4)

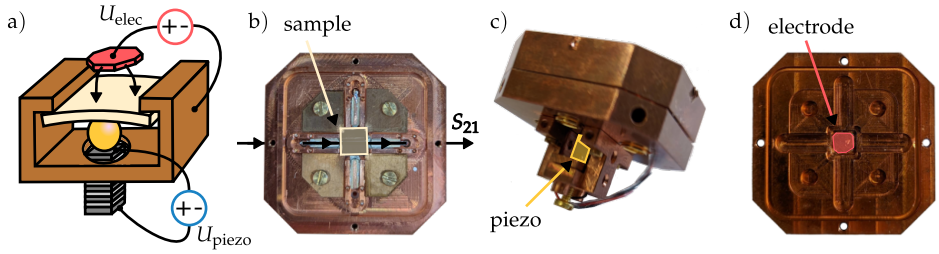


**Figure 4.5: Sample holder design and functionalities. a)** Sketch of the copper sample holder. A piezo actuator connected to a zircon sphere (purple) and a DC electrode (red) are used to apply strain to the sample as well as an global electric field. **b)** The sample chip is fixated inside the bottom housing of the sample holder by a clamp on each corner. Microstrip PCBs guide the microwave signal from the SMP connectors to the on-chip transmission line. **c)** Closed sample holder with H-shaped piezo mount screwed to the backside. **d)** Sample holder lid. The DC electrode is glued to the center pin of a SMA connector, which terminates inside a recess and is galvanically insulated from the rest of the (grounded) sample holder.

zircon sphere, which decouples the piezo from the electric ground and ensures a point-like contact. Prior to installing and cooling down the sample, this contact is tightened via a screw at the center of the piezo mount which can move the piezo stack (see Ref. [177] for details). Then, applying a voltage extends the piezo and thus puts strain on the sample (Eq. 2.48)

Also for TLS tuning experiments [178], a DC electrode is placed inside a recess of the sample holder lid, where it is glued to the center pin of a SMA connector (Fig. 4.5d). When the potential of this electrode is raised, an electric field is generated that points towards the grounded backside metalization of the sample and thus interferes with the resonator films. The voltages for the piezo $U_{\text{piezo}}$ and the electrode $U_{\text{elec}}$ are generated by two independent sources at room temperature (Fig. 4.4). For these DC lines, also appropriate low-pass filters (300 kHz $\pi-$ filter, 1 kHz T $-$ filter) are installed.

## 4.3 Noise measurement techniques

Generally, different methods and techniques for measuring low frequency noise (sample rate $\leq 500$ Hz) in superconducting quantum circuits exist. The state of the art setup for tracking the frequency fluctuations $\delta\omega_{\text{r}}(t)$ of a microwave resonators is the Pound loop [179]. This setups uses a power detector in combination with PID controller to constantly lock the measurement frequency to the resonance

frequency. These adjustments can directly be translated into the changes of the resonance frequency over time.

A more convenient alternative is using a VNA to continuously measure the phase response with the probe tone fixed to the average resonator frequency $\omega_0 = \overline{\omega}_\mathrm{r}$ (continuous wave mode). If the time dependent frequency fluctuations $\delta\omega_\mathrm{r}(t) = \omega_\mathrm{r}(t) - \omega_0$ are small compared to the internal loss $\delta\omega_\mathrm{r}/\kappa_\mathrm{i} \ll 1$, the phase response of the resonator can be approximated as

$$\begin{aligned} \arg\left(S_{21}^{\mathrm{reso}}(\omega)\right) &= -\arctan\left(2\frac{\omega-\omega_\mathrm{r}(t)}{\kappa_\mathrm{r}}\right) + \arctan\left(2\frac{\omega-\omega_\mathrm{r}(t)}{\kappa_\mathrm{i}}\right) \\ &\approx -2\frac{\omega-\omega_\mathrm{r}(t)}{\kappa_\mathrm{r}} + 2\frac{\omega-\omega_\mathrm{r}(t)}{\kappa_\mathrm{i}} \end{aligned} \tag{4.4}$$

and it is easy to see that a change in the measured phase response

$$\delta\phi(t) \approx \frac{\kappa_\mathrm{r}-\kappa_\mathrm{i}}{\kappa_\mathrm{r}\kappa_\mathrm{i}}\delta\omega_\mathrm{r}(t) \tag{4.5}$$

can be directly mapped to $\delta\omega_\mathrm{r}(t)$.

### 4.3.1 Frequency fluctuation tracking

For some samples studied in this work, frequency fluctuations on the order of the resonator linewidth ($\sim 0.1\kappa_\mathrm{r}$) are observed, where the linear approximation of the phase brakes down and yields ambiguous results. At the same time, the sole amplitude signal is insensitive to the direction of the shift (Fig. 4.6(a)). To overcome both problem, a alternative VNA measurement scheme was developed that uses the total (amplitude and phase) transmission data $S_{21}^{\mathrm{meas}}$. Its core principals are illustrated in Fig. 4.6(b). In the first step, the resonance circle $S_{21}^{\mathrm{reso}}(\omega)$ of the resonator under investigation is measured and fitted. It will serve as a lookup table for the actual measurement. In the second step, the timetrace is recorded by continuously measuring the complex transmission $S_{21}^{\mathrm{meas}}(\omega_0, t)$ with the frequency fixed to the average resonance frequency $\omega_0 = \overline{\omega_\mathrm{r}}$. There, the data acquisition rate is, to sufficient precision, equal to the inverse of the VNAs bandwidth. When the resonator frequency $\omega_\mathrm{r}(t)$ changes during the data recording, the resonance circle gets effectively rotated in the complex plane of the measurement frame, which places $S_{21}^{\mathrm{meas}}(\omega_0(t))$ somewhere on the circle trajectory. Because of additional noise that is not purely from a shift of the resonance frequency, e.g., from the amplification electronics, the measured data points are rather scattered along the circle trajectory. In the third step, these data point are projected on the prerecorded resonance circle, which is then inverted to find the corresponding resonator frequency

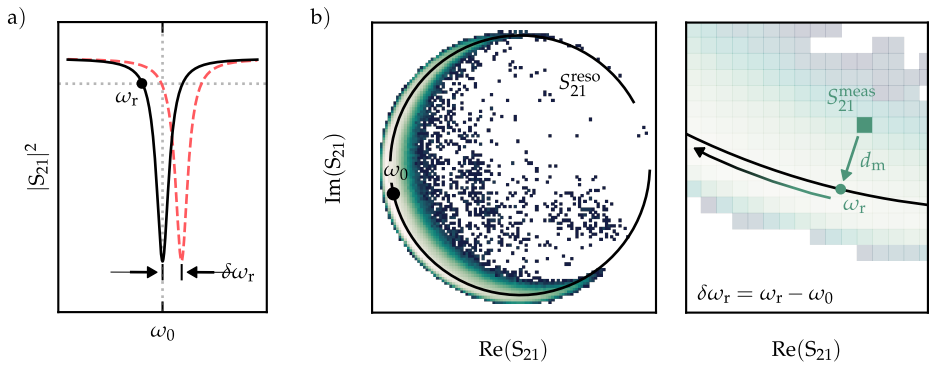


**Figure 4.6: Frequency tracking scheme. a)** Schematic drawing visualizing the measurement of the resonator frequency fluctuations $\delta\omega_r$ using only the amplitude of $S_{21}$. When recording at a fixed frequency $\omega_0$, a shift of the resonance frequency corresponds to a change in the measured amplitude signal $|S_{21}|^2$. Knowledge of the initial resonance shape (black line) allows mapping from the new $|S_{21}|^2$ value to the new center frequency of the resonator $\omega_r$. **b)** Since the amplitude signal is not sensitive to the direction of the frequency shift, the scheme is extended to the complex plane. Left panel: Distribution of the complex transmission data from a fixed frequency measurement at $\omega = \omega_0$. Left panel: Each data point is projected (over a distance $d_m$) on a prerecorded resonance circle $S_{21}^{reso}$ and subsequently mapped to the corresponding resonance frequency $\omega_r$.

$\omega_r(t)$. Mathematically, $\omega_r(t)$ is then defined as the frequency that minimizes the expression

$$\min_{\omega\in[\omega_0-\epsilon,\omega_0+\epsilon]} |S_{21}^{reso}(\omega) - S_{21}^{meas}(\omega_0, t)|, \tag{4.6}$$

where $2\epsilon$ is the frequency span of the prerecorded resonance circle. In the last step, the frequency fluctuations are calculated as $\delta\omega_r(t) = \omega_r(t) - \omega_0$.

### 4.3.2 Power spectral density

Once the frequency noise trace of a resonator is recorded, the question naturally arises how to properly analyses and quantify the data in order to draw physical conclusions and to allow for a comparison between different resonators and samples. The most simple approach is calculating the average noise power

$$\overline{P}_{\delta\omega_r} = \frac{\hbar}{N}\sum_{n=1}^{N} \delta\omega_{r,n}(t)^2 \tag{4.7}$$

of the signal, where N is the total number of measured data points $\delta\omega_{r,n}(t)$. While this can be a sufficient measure for the frequency (in-)stability of a resonator, it

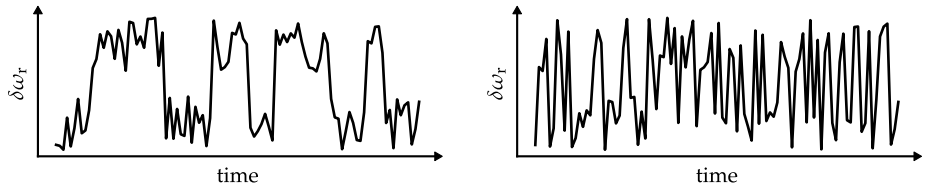


**Figure 4.7: Average noise power dilemma**. Example containing two artificial time series of frequency fluctuations $\delta\omega_r(t)$ with different spectral signatures but an identical average noise power.

completely neglects the temporal information of the signal, i.e, the order in and rate at which the data points $\delta\omega_{r,n}(t)$ were taken. As a consequence, two time series can have an identical same noise power despite an obvious difference in their spectral composition (Fig. 4.7).

Such limitations are overcome when looking at the power spectral density (PSD) instead, which quantifies the power of the frequency components composing a signal by means of Fourier analysis. For a discrete system with a finite number of samples ($N \nrightarrow \infty$), the PSD can be estimated from

$$S_{\delta\omega_r}(f) \simeq \frac{1}{Nf_s}\left|\sum_{n=1}^{N}\delta\omega_{r,n}(t)e^{i2\pi nf/f_s}\right|^2 = \frac{1}{Nf_s}\left|\sum_{n=1}^{N}\delta\hat{\omega}_{r,d}(f)\right|^2, \tag{4.8}$$

where $f_s$ is the sampling rate and $\delta\hat{\omega}_{r,d}(f)$ is the discrete-time Fourier transform. Conceptually, the PSD describes how much a signal is fluctuating on a certain timescale. While increasing the number of samples improves the approximation in Eq. 4.8 and, according to Nyquist–Shannon sampling theorem, allows resolving slower fluctuations, it does not reduce the variance of the PSD [180]. A popular algorithm that is employed for this purpose is Welch's method [181]. Therein, the original data set is split into L overlapping segments of length M, with the overlap typically chosen to be 50% (see Fig. 4.8 for a visualization of Welch's method). Then, a window function is applied to the individual segments. Throughout this work, the Hann(ing) window [182]

$$w(n) = 0.5 - 0.5\cos\left(\frac{2\pi n}{M-1}\right) \qquad 0 \leq n \leq M-1 \tag{4.9}$$

was used, though other windows are available which, here, yield identical results (Appendix C.2). After the segments are windowed, the periodogram, Eq. 4.8, of each segment is calculated by computing the discrete Fourier transform (DFT). There, the window function helps to avoid edge effects in the DFT, but affords more influence to the data at the center of the window then at the edges. The purpose of the overlap is to mitigate this loss of information. In the last step, all periodograms

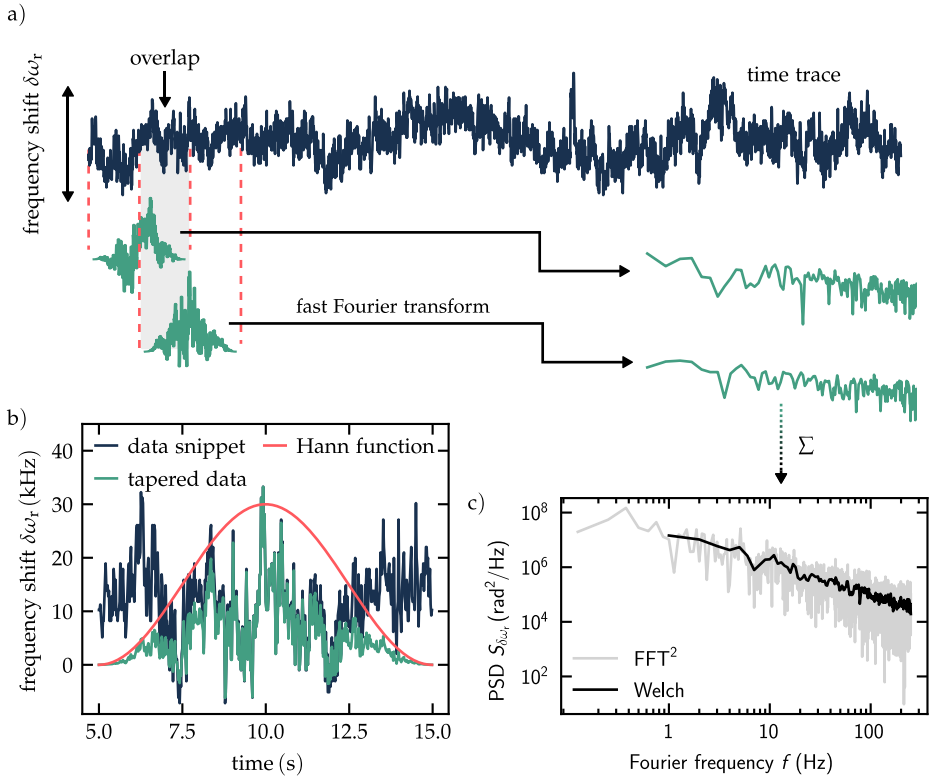


**Figure 4.8: Welch's method for calculating the power spectrum. a)** To calculate the power spectral density (PSD), a time signal (here: fluctuations of the resonance frequency $\delta\omega_r$) is first split into overlapping segments. **b)** Each data segment is then windowed by an appropriate function (here: Hann window), which reduces edge effect in the fasst Fourier transform (FFT) that is subsequently computed. **c)** Averaging over the square of all Fourier transforms yields the Welch PSD, which is much smoother then than simply calculating the FFT for the whole time series. The trade-off is a smaller spectral window.

are averaged, which finally reduces the variance. The spectral frequency range covered by the PSD calculated from Welch's method is,

$$\frac{1}{T_{\text{seg}}} < f < \frac{f_s}{2}, \tag{4.10}$$

where $T_{\text{seg}} = M/f_s$ is the measurement time of all data points within one segment. Thus, the lowest resolvable frequency is determined by the choice for M (or L), rather then the total measurement time $T_{\text{meas}} = N/f_s$.

Various type of noise can be differentiated by the shape of their power spectrum [11], which often follows a simple power law $S(f) = h^*_{-1}/f^n$. Here, $h^*_{-1}$ describes

the signal power at 1 Hz. Uncorrelated noise, which originates, e.g., from thermal noise of resistors, has a flat PSD ($n = 0$) and is refereed to as white noise [183]. In solid-state quantum devices, noise often decreases as $1/f$ ($n = 1$) [12], i.e, it has a higher power towards lower frequencies. Such signals are refereed to as pink noise [5], or, more commonly, as $1/f$ noise. Another special type of noise, which has a Lorentzian spectrum of the form

$$S(f) = \frac{4\tilde{I}^2\tau_0}{1 + (2\pi f\tau_0)^2} \tag{4.11}$$

is a random telegraph signal (RTS). The corresponding time series is characterized by random transitions between two or several distinct states with an average lifetime $\tau_0$ (left panel Fig. 4.7, see Sec.C.1 for mathematical details). In certain scenarios, such as donor traps in semiconductors [184] or TLS in dielectrics, $1/f$ noise is believed to originate from the superposition of multiple RTS fluctuators with varying lifetimes $\tau_0$ (see, e.g., Fig. 2.6(b)). In the opposite limit, a large number of fluctuators with (almost) identical $\tau$ still result in a noise spectrum which retains its Lorentzian shape, but the distinct states get smeared out in the time signal which becomes Gaussian instead. In this case, the RTS is commonly referred to as generation-recombination (g-r) noise, which in superconductors occurs due to the continuous formation and braking of Cooper pairs [128].

### 4.3.3 Allan deviation

A different tool that can equally be used to quantify the frequency instability of oscillators is the Allan deviation [185]. Historically, it has been developed for signal analysis as an improvement of the standard deviation (STD), which has the problem of monotonically increasing without limit when the data set contains non-white noise with a power law spectra. To find the Allan deviation, a time series of fractional frequency shifts $y(t) \equiv \delta\omega_\mathrm{r}$ is divided into M adjacent segments $y_\mathrm{k}(t)$ of duration $\tau$ (see Fig. 4.9). If $\overline{y}_\mathrm{k}$ is the average value of the $k$th segment, the Allan deviations of a finite data set can be estimated as

$$\sigma_\mathrm{y}(\tau) = \left[\frac{1}{2(M-1)}\sum_{k=1}^{M-1}(\overline{y}_{\mathrm{k}+1} - \overline{y}_\mathrm{k})^2\right]^{\frac{1}{2}}. \tag{4.12}$$

Note that squared difference is taken between adjacent values of $\overline{y}_\mathrm{k}$, compared to the STD, where one would subtract the total mean $\overline{y}_\mathrm{mean} = \sum\overline{y}_\mathrm{k}/M$ from each

[5] The noise color is chosen in analogy to the respective frequencies of visible light

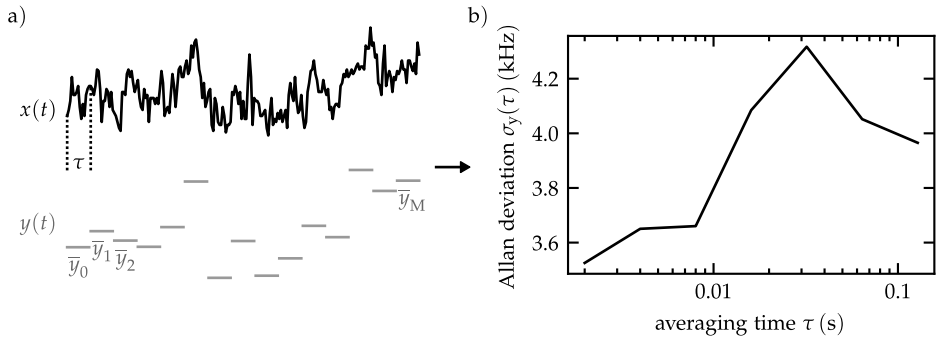


**Figure 4.9: Allan deviation. a)** Using Allan's technique to analyze the characteristics of a noisy signal, the corresponding time series is split into adjacent segments of identical lenght $\tau$. The average value of each segment is then used to calculate the Allan deviation according to Eq. 4.12. **b)** Varying the lenght of the segments, one obtains the noise level on different time scales, i.e., the noise spectrum.

value instead. By evaluating the Allan deviation for different $\tau$ values, the strength of the fluctuations on various time scales can be calculated. For a discrete time series, a natural choice is $\tau = n/f_s$, where $f_s$ is the sampling rate and $n \in [1, N/2]$ is limited by the total number of data points $N = nM$. In practice, the estimate of the Allan deviation, Eq. 4.12, can be greatly improved by using overlapping segments [186, 187]. This so-called 'overlapping Allan deviation' is the preferred estimator in electronics and telecommunication.

The Allan deviation(time domain) is related to the PSD (frequency domain) by the integral [188, 189]

$$\sigma_y^2(\tau) = \int_{-\infty}^{\infty} \frac{4\sin^4(\pi f\tau) S_y(f)}{(\pi f\tau)^2} df. \tag{4.13}$$

Comparing the two, the Allan deviation has the advantage of being more easily applicable to non-stationary processes. Additionally, it often allows for a clearer separation of random telegraph signals (RTS) from the noise background. However, it is usually easier to identify and understand different types of noise in from the power spectral density, which, at the same time, is less susceptible to artifacts in the measurement data. Nowadays, where computational power is no longer a limiting factor, the PSD is thus the preferred tool in most works, including this one.

## 4.4 Electric field simulations

When performing TLS field tuning experiments (Chapter 6) with the electrode built into the sample holder (Fig. 4.5), only the value of the applied voltage $U_{\mathrm{elec}} \in [-200\,\mathrm{V}, 200\,\mathrm{V}]$ is well known. However, for a physical interpretation of the data, knowledge of the corresponding electric field $\mathbf{E}_{\mathrm{elec}}(U_{\mathrm{elec}}, \mathbf{x})$ at $\mathbf{x}$, the position of the TLS, is required. For this reason, the electrostatic finite element solver *Maxwell* provided by the *ANSYS Electromagnetics Suite* (Release 2021 R2) was employed for (numerical) simulations of the field distribution. Figure 4.10(a) shows a cut view of the three-dimensional (3D) simulation model containing the sample holder, the DC electrode as well as the chip hosting the resonator(s) and a transmission line.

Since the thickness of the granular aluminum film is a factor of $\sim 10^4$ smaller then the distance between sample and DC electrode, a field simulation along the resonator film edge in the full 3D model would require a technically not feasible amount of memory. For this reason, the problem was mapped onto a two-dimensional (2D) model (Fig. 4.10b)), where the top electrode is replaced by an effective electrode which accounts for the actual field geometry. Using a coarse 3D simulation, one finds that the average potential at the effective electrode equates to $U^*_{\mathrm{elec}} \approx 0.3 U_{\mathrm{elec}}$, assuming that the charge number on the resonator is conserved and the transmission line is effectively grounded ($R_{\mathrm{TL}\to\mathrm{GND}} \approx 70\,\Omega$).

Figure 4.10c) shows the electric fields at the end of a resonator for $U_{\mathrm{elec}} = 1\,\mathrm{V}$ obtained from the 2D simulation, where the film as well as the ground plane on the other side of the sapphire substrate were treated as a perfect conductors. The corresponding absolute field values at a positional axis $x_{\mathrm{r}}$ along the film edge, where the fields are strongest, are plotted in Fig. 4.10c) (black line). Note that the choice for the shape of the film edge, while motivated by the dry etching process used in the sample fabrication [177], is arbitrary and can differ in reality, potentially leading to errors in the absolute field values. This does, however, not affect the significance of the findings and the general interpretation of the data, as discussed in Chapter 6.

Because the exact position of the TLS $x_{\mathrm{r}}$ is generally not known, it is convenient to only consider the maximum field strength at the film edge $E_{\mathrm{z}} = |\mathbf{E}_{\mathrm{elec}}(\mathbf{x}_{\mathrm{r}})|_{\mathrm{max}} = 3144\,m^{-1} \times U_{\mathrm{elec}}$ [6]. The advantage of this conversion is that the (parallel) electric

[6] Simply modeling the DC electrode and the ground below the sample as a plate capacitor partially field by the sapphire substrate dielectric ($\epsilon_{\mathrm{r}} \approx 11$) yields a global field strength of $E_{\mathrm{z}}/U_{\mathrm{elec}} = 1754.4\,m^{-1}$, on the same order of magnitude as the simulated value.

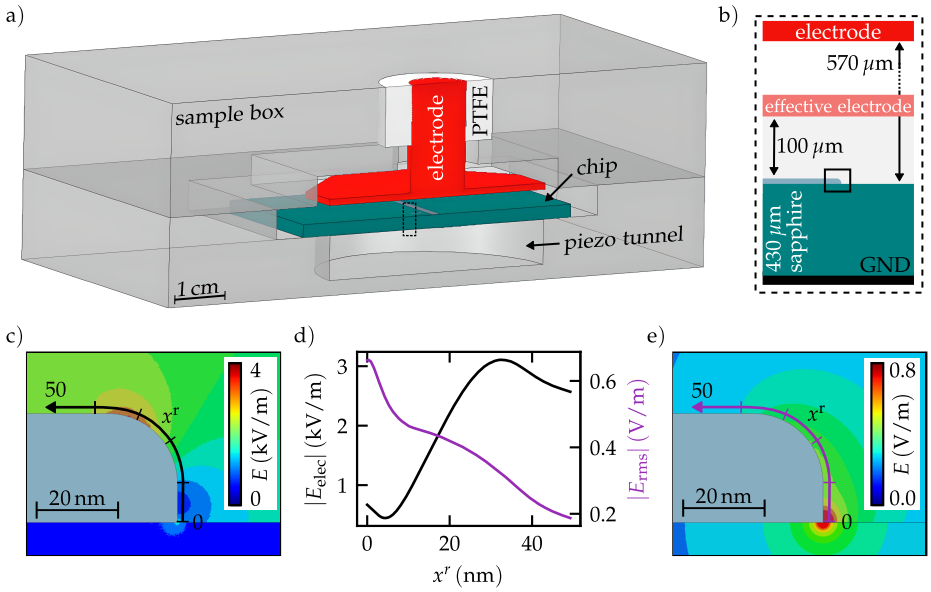


**Figure 4.10: Electric field simulation model and results. a)** Cut view of the 3D simulation model. The sample box hosts a sapphire chip with a single superconducting resonator and the global transmission line. **b)** Simplified 2D model used to simulate the electric field distribution along the edge of the resonator film. The voltage on the effective electrode $U^*_{\mathrm{elec}}(U_{\mathrm{elec}})$ is determined from the 3D simulation. **c)-e)** Absolute values of the electric field distributions $E_{\mathrm{elec}}$ (left) and $E_{\mathrm{rms}}$ (right) generated by the the sample box electrode ($U_{\mathrm{elec,simu}} = 1\,V$) or the root means square voltage of the resonator ($U_{\mathrm{rms,simu}} = 1\,\mu\mathrm{V}$), respectively. In d), the strength of the respective field in a distance of 3 nm from the film edge is shown.

dipole of the TLS directly appears in Eq. 2.48, instead of an effective coupling strength to the applied voltage ($p^* U_{\mathrm{elec}} \rightarrow 2dE_z$).

An alternative way to access the dipole moment of the TLS is from the strength of the coupling to the resonator (Eq. 2.52), which requires knowledge of the single photon mean field produced by the resonator modes ($\mathbf{E}_{\mathrm{rms}}(U_{\mathrm{rms}}, \mathbf{x})$). Since the quantity of interest is, again, the maximum field strength, it is sufficient to consider the static case where $U_{\mathrm{rms}}$ has the maximum vale. There, the capacitance between the resonator and the transmission line are negligible to first order ($C_c/C \lesssim 0.3$), thus the mean field can also be simulated in the 2D case. To calculate the corresponding voltage $U_{\mathrm{rms}}$, it is convenient to model the distributed resonator with lumped elements. For the $\lambda/2$ resonator used in this work, the current is maximum in the middle while the voltage between resonator and ground is maximum at both

ends. Thus, one can approximate the resonator as an inductance $L$ that is shunted to ground at both ends by an capacitance $C/2$, which yields [40]

$$U_{\mathrm{rms}} = \sqrt{\frac{\alpha}{8\pi}} \frac{\hbar\omega_{\mathrm{r}}}{e} \sqrt{\frac{Z}{Z_0}}. \tag{4.14}$$

for the root mean square voltage. Here, $\alpha$ is the fine structure constant and $Z = \omega_{\mathrm{r}} L_{\mathrm{k}}^{\square} l_{\mathrm{y}} / w_{\mathrm{x}}$ is the impedance of the $w_{\mathrm{x}} = 2\,\mathrm{nm}$ wide resonator stripe, resulting, on average, in $U_{\mathrm{rms}} \approx 15\,\mu\mathrm{V}$. For the simulation, the potential of the resonator is simply raised to $U_{\mathrm{rms}}$ while the voltage on the electrode is set to zero. The field distribution obtained for $U_{\mathrm{rms}} \approx 1\,\mu\mathrm{V}$ is shown in Fig. 4.10e), and the corresponding absolute field values as a function of $x_{\mathrm{r}}$ are plotted in Fig. 4.10(d) (purple line). The concentration of the field at the film corner facing the substrate ($x_{\mathrm{r}} = 0$) is typical for thin film circuits, and most of the observable TLS are expected to reside there [6].

# 5 Resonance frequency fluctuations

In this chapter, which is based on Ref. [190], measurements of the general properties of all granular aluminum resonators and their low frequency noise are presented. These quantities are studied for increasing temperatures, probing powers and with respect to the sheet resistance of the different sample. In addition, dissipative aspects of the resonator noise are investigated. The chapter is concluded by a discussion of different mechanisms that potentially explain the spectral distribution of the observed noise, which differs from noise spectra typically measured in more conventional resonators made out of (pure) aluminum or niobium.

## 5.1 Resonator frequencies and linewidths

As discussed in Sec. 2.3, the resonance frequency ($\omega_r$) and linewidth ($\kappa_r$) of microwave resonators made from superconducting films are influenced significantly be the presence and distribution of quasiparticles (QP) and two level systems (TLS) in the particular film. Consequently, studying these influences allows drawing conclusions about the structural and superconducting properties of the resonator material and its surface oxides.

In this work, to obtain all relevant resonator parameters ($\kappa_r, \kappa_c, \omega_r$), Eq. 3.15 is fitted to the measured resonance circle, as described in Ref. [166] (see also inset Fig. 5.1(a)). The loss rates measured for all resonators at an average resonator photon number $\overline{n} \sim 100$ and base temperature of T=25 mK are listed in Tab. 5.1, normalized by the respective resonance frequency. Because for all resonators, energy loss is dominated by the coupling to the transmission line ($\kappa_r \sim \kappa_c$), there is a rather large uncertainty when calculating the internal loss rate $\kappa_i = \kappa_r - \kappa_c$. Using the fact that $\kappa_i \ll \kappa_r$, one can merely make an estimate for the internal losses $\kappa_i/\omega_r = \mathcal{O}(10^{-5})$ of the studied granular aluminum resonators, which are in agreement with earlier measurements [3, 47, 48].

**Table 5.1:** Total ($\kappa_r$) and coupling ($\kappa_c$) loss rates of the resonators at an average photon number $\overline{n}$, normalized by their resonance frequency $\omega_r$. The dressed dielectric loss tangent $F\tan(\delta_0)$ is extracted from a fit of Eq. 2.49 to $\kappa_r(\overline{n})$, as shown in Fig. 5.1. Brackets indicate values with large errors $\sigma_x/x \leq 1$, $x$ being the measured quantity.

| Reso. | $\omega_r/2\pi$ (GHz) | $R_n^{\square}$ (k$\Omega$) | $\kappa_r/\omega_r \times 10^{-4}$ | $\kappa_c/\omega_r \times 10^{-4}$ | $F\tan(\delta_0) \times 10^{-5}$ |
|---|---|---|---|---|---|
| A1 | 10.565 | 0.59 | 2.22 | 2.09 | 1.93 |
| A2 | 10.740 | 0.61 | 2.51 | 2.43 | 0.73 |
| B1 | 5.494 | 1.39 | 3.35 | 3.33 | 1.0 |
| B2 | 6.154 | 1.49 | 3.73 | 3.65 | 1.89 |
| B3 | 6.793 | 1.53 | 3.85 | (3.85) | 1.61 |
| C1 | 4.069 | 3.97 | 1.49 | 1.38 | 2.88 |
| C2 | 4.663 | 4.32 | 1.75 | 1.64 | 5.21 |
| C3 | 5.780 | 3.76 | 2.61 | 2.47 | 2.98 |
| D1 | 8.006 | 0.65+12 | 2.16 | 2.15 | 2.0 |
| D2 | 9.010 | 0.69+12 | 3.29 | 3.26 | (12.93) |
| D3 | 9.995 | 0.71+12 | 2.97 | (2.97) | 1.75 |
| E1 | 7.839 | 0.68+190 | 2.01 | 1.88 | 1.3 |
| E2 | 8.872 | 0.68+190 | 0.5 | (0.67) | 1.32 |

### 5.1.1 Power dependence

A more robust quantity is the dielectric loss tangent $\tan(\delta_0)$, which quantifies how the resonator loss rate scales with the average number of photons $\overline{n}$, due to a bath of TLS in the resonator dielectric. This behavior is shown for resonator C1 in Fig. 5.1(a). Fitting Eq. 2.49 to the data yields $F\tan(\delta_0) = 2.88 \times 10^{-5}$ for the dielectric loss tangent dressed by the filling factor of the dielectric $F$. Assuming that the majority of TLS reside in a 4 nm thick, amorphous aluminum oxide layer ($\epsilon_r \sim 10$) on the resonators surface, finite element simulations within ANSYS Maxwell yields $F = 10^{-4}$, in agreement with values published for comparable resonator geometries [47]. With this, the TLS density can be estimated at $P_0 = 3\epsilon_r \tan(\delta_0)/(\pi d^2) \approx 2.5 \times 10^5\,\mathrm{GHz^{-1}\mu m^{-3}}$ ($P_V = P_0/V \approx 1 \times 10^6\,\mathrm{GHz^{-1}}$), choosing $d = 0.5\,e\text{Å}$ for the average TLS dipole moment. This density is significantly larger than values ranging from $200 - 1000\,\mathrm{GHz^{-1}\mu m^{-3}}$ typically quoted for bulk dielectrics [178, 191]. A possible explanation for this discrepancy was provided by Grünhaupt *et.al.* [47], suggesting that the quality of granular aluminum microstrip resonators is limited by excess quasiparticles, not by surface dielectric loss. Alternatively, one might assume that the resonator fields actually penetrate the whole superconducting film of the resonator ($t \ll \lambda_L$) [192], which for granular aluminum partially consists of

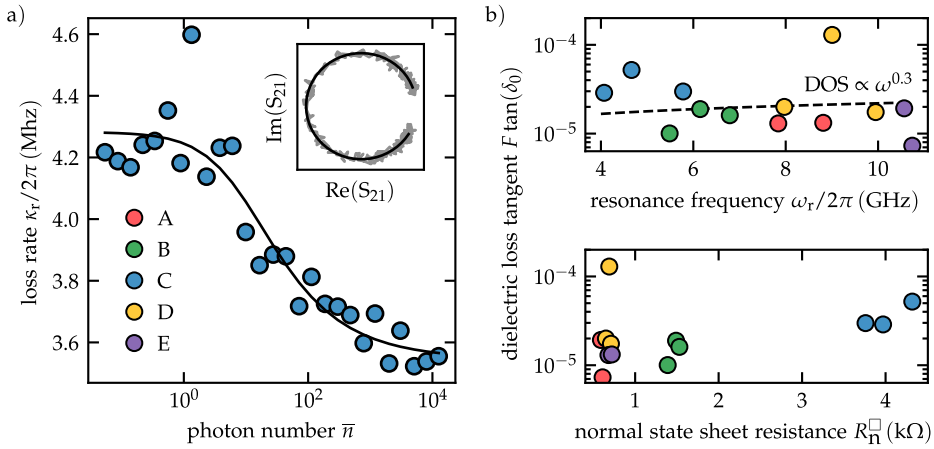


**Figure 5.1: Resonator loss tangent. a)** Photon number dependent loss rate $\kappa_r$ of resonator C1. Solid line is a fit to Eq. 2.49, which yields the dressed loss tangent $F\tan(\delta_0)$. Inset: To obtain the resonator parameters, Eq. 3.15 is fitted to the complex resonator transmission data. **b)** Dressed loss tangents for all resonators versus their respective normal state sheet resistance $R_n^{\square}$ and resonance frequency $\omega_r$. Dashed line indicates the expected scaling due to interacting TLS ($\mu = 0.3$).

an amorphous oxide. In this case, the participation ratio $F$ would be significantly larger, resulting in smaller values for the dielectric loss tangents and TLS densities.

The fitted loss tangents for all resonator are listed in Tab. 5.1 and plotted in Fig. 5.1(b) as a function of the resonance frequency and normal state sheet resistance, respectively. Within the error margin ($\sim 30\%$, error bars omitted for clarity), no noticeable frequency dependence can be observed. This potentially agrees with both, the STM which proposes a constant DOS ($\mu = 0$), or a model of weakly interacting TLS ($\mu = 0.3$). The weak frequency dependence of the latter is indicated by a dashed line. Regarding the dependence on the sheet resistance, a slightly higher loss tangent can be observed for the resonators from sample C, which is made from the film with the highest oxygen concentration. However, the difference is not significant enough to substantiate potential interpretations.

### 5.1.2 Temperature dependence

While increasing the sample temperature can actually reduces the dielectric loss through TLS (see Eq. 2.49 and Eq. 2.54), the total loss rate of the resonator will still increase due to thermally activated quasiparticle. Such behavior can be observed in Fig. 5.2(a), which shows the relative internal loss rate of resonator C1 measured for increasing sample temperatures. Since the theoretically expected behavior

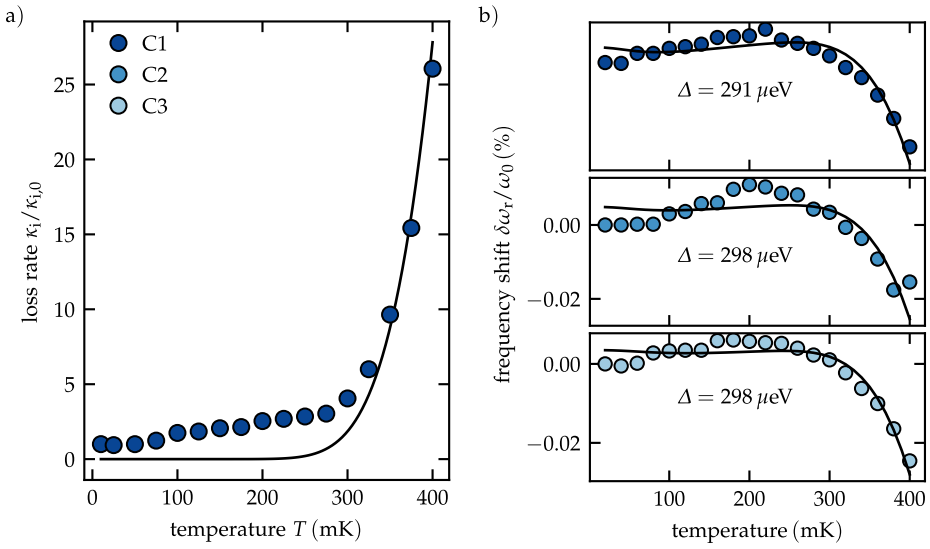


**Figure 5.2: Temperature dependent resonator behavior. a)** Relative change of the internal loss rate $\kappa_i$ of resonator C1 for increasing temperature. Solid line is a fit to Eq. 2.40. **b)** Simultaneously measured resonance frequency shift for resonators C1-C3 as a function of the sample temperature. The data can be modeled by Eq. 5.1.

described by Eq. 2.40 does not take into account nonequilibrium QP or TLS, the observed discrepancies at low temperatures are expected. At the same time, at higher temperatures, the total loss is no longer dominated by the coupling alone as $\kappa_i \to \kappa_c$ and the extracted values become more precise, resulting in a better agreement with the theoretical curve.

Together with the broadening of the resonance, one can observe a change of the resonance frequency when altering the sample temperature (see Fig. 5.2(b)). At low temperatures, the dielectric constant seen by the resonator is increased du to the resonant interaction with TLS. This effect gets diluted at higher temperatures where incoherent processes, induced by the TLS bath, start to play a role [22]. At even higher temperatures, the growing number of quasiparticles increases the kinetic inductance of the film significantly, resulting in a distinct shift of the resonance towards lower frequency [130]. Thus, the dependence $\delta\omega_r$ over the whole temperature range can be described by

$$\frac{\delta\omega_r(T)}{\omega_r} = \frac{\delta\omega_r^{QP}(T)}{\omega_r} + \frac{\delta\omega_r^{TLS}(T)}{\omega_r} + \frac{\delta\omega_r^{TLS}(T_0)}{\omega_r}, \tag{5.1}$$

where $T_0$ is a reference temperature, accounting for the fact that $\omega_r$ deviates from the unperturbed resonance frequency (which is generally unknown) at $T = 0$. The

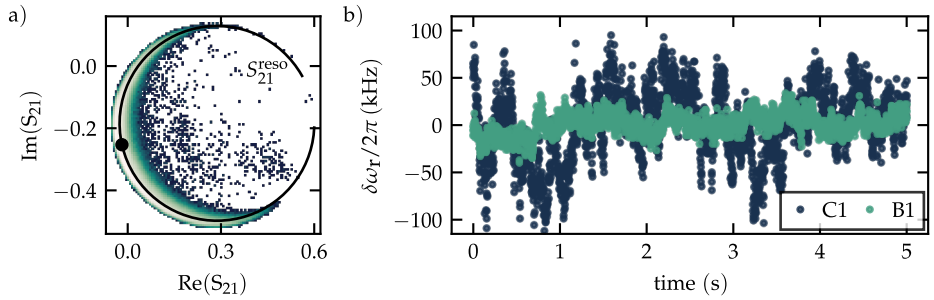


**Figure 5.3: Resonator noise data. a)** Raw complex transmission data from a fixed frequency measurement containing $\mathcal{O}(10^6)$ data points. Black line is a fit to the prerecorded resonance circle $S_{21,\,\text{reso}}(f)$. The data is processed by means described in Sec. 4.3.1 to obtain the resonator's frequency fluctuations. **b)** Extracts from the frequency fluctuation time series of resonator C1 and B1, recorded at a bandwidth of 500 Hz and an average photon number $\overline{n} \sim 2 \times 10^3$. Figure adapted from Ref. [190].

QP and TLS contributions are given by Eq. 2.41 and Eq. 2.50, respectively . Fitting Eq. 5.1 to data from resonators C1-C3 yields an average value of $\Delta = 296 \pm 3\,\mu\text{eV}$ for the superconducting gap of granular aluminum, in agreement, within 10%, with measurements on comparable films [47, 53, 99].

## 5.2 Resonator noise data

Frequency fluctuations of resonator A1, B1-B3 and C1-C3 were measured using the tracking method detailed in section 4.3.1. In short, the complex transmission coefficient $S_{21}$ was continuously measured at a fixed frequency $\omega_0 \equiv \overline{\omega}_r$. Figure 5.3(a) depicts the resulting distribution of data points in the complex plain. Using knowledge of the pre-measured resonance circle $S_{21}^{\text{reso}}(\omega)$, each data point ($S_{21}^{\text{meas}}(\omega_0, t)$) can be mapped to the corresponding resonance frequency $\omega_r(t)$ at that point in time, allowing to calculate the resonator noise as $\delta\omega_r(t) = \omega_r(t) - \omega_0$.

A typical noise time trace sets contains $\mathcal{O}(10^6)$ measurement points, taken at a rate of 500/s, which is sufficient to cover the relevant timescales while keeping the data overhead low. Extract of such data sets taken for resonator C1 and B1 are shown in Fig. 5.3(b). The evident difference in the time series is representative for the overall, qualitative picture: Compared with the other samples, the fluctuations of the resonance frequency $\delta\omega_r$ are much more pronounced in the resonators with the highest sheet resistances (C1-C3), where values up to $\delta\omega_r/\kappa_r = 0.1$ can be

**Table 5.2:** Average noise power $\overline{P}_{\delta\omega_r}$ of selected resonators, measured at $\overline{n} = 2 \times 10^3$.

| Reso. | A1 | B1 | B2 | B3 | C1 | C2 | C3 |
|---|---|---|---|---|---|---|---|
| $\overline{P}_{\delta\omega_r}$ ($10^{-25}$W) | 0.53 | 0.23 | 0.80 | 0.83 | 2.32 | 6.71 | 6.29 |

observed. Quantitatively, this is supported by the average noise powers measured for the different resonators (Tab. 5.2).

Upon closer inspection of Fig. 5.3(b), one finds that the resonator randomly switches between discrete positions in frequency space, which can be evidence for both, a multi-level RTS signal (g-r noise) or simply $1/f$ noise. To discriminate between the two, the power spectrum of the resonator noise will be studied in the subsequent sections.

## 5.3 Power spectral density

Figure 5.4(a) shows the fractional noise spectrum $S_y = S_{\delta\omega_r}/\omega_r^2$ of resonator C1, calculated from Welch's method. Similar to a pure aluminum resonator ($R_n \sim 0.3\,\Omega$) measured under identical conditions (Fig. 5.4(c), $T = 25\,\mathrm{mK}$, $\overline{n} \approx 5 \times 10^5$), the spectrum follows a distinct $1/f$ trend. The granular aluminum samples shows, however, a orders of magnitude higher noise amplitude. Additionally, in the region between 0.1 Hz and 10 Hz, its spectrum noticeably deviates from the $1/f$ trend. The spectral shape of these low frequency excess fluctuations is reminiscent of a Lorentzian, i.e., it indicates a RTS (see Sec. 4.3.2). At higher temperatures (Fig. 5.4(b)), the nose of the Lorentzian clearly shifts towards higher frequencies. To track this shift even when increasing temperatures up to 400 mK, the data acquisition rate was increased from 500/s to 4000/s for $T > 200\,\mathrm{mK}$.

Adding up the different contributions and, in addition, including a white noise floor[1], the full fractional noise spectrum can be modeled by

$$S_y = \frac{4I^2\tau_0}{1 + (2\pi f\tau_0)^2} + \frac{h_{-1}}{f} + h_0, \tag{5.2}$$

with the amplitude of the RTS $I$, the $1/f$ noise $h_{-1}$, and the white noise $h_0$, respectively.

[1] White noise can, e.g, originate from various electronic components, like amplifiers or attenautors, in the form of shot noise [193, 194]

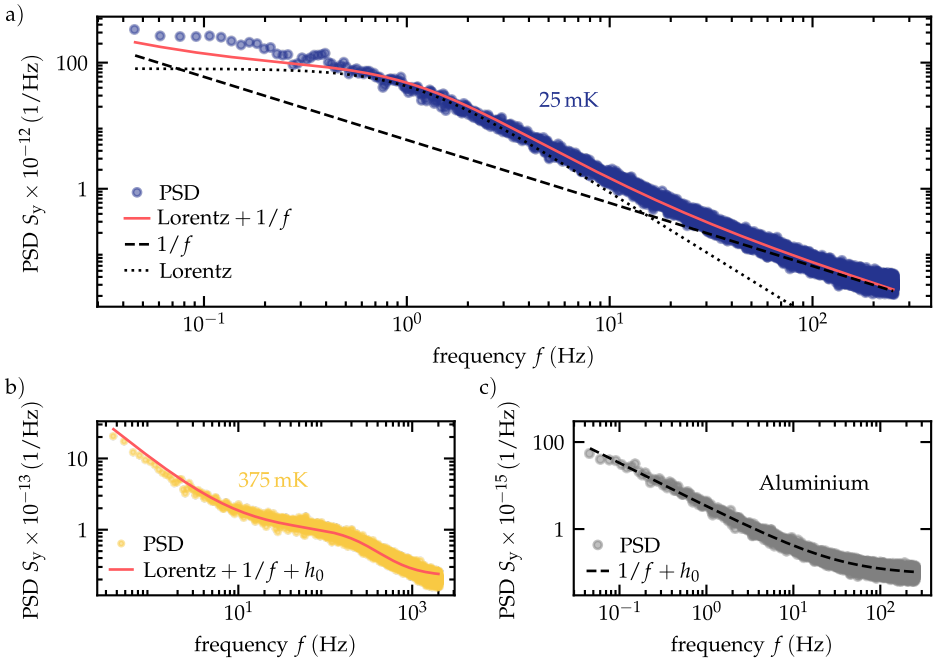


**Figure 5.4: Fractional noise spectra. a)** Low temperature (T=25 mK) fractional noise spectrum of resonator C1 shows a $1/f$ dependency (dashed line), masked by RTS excess noise below 10 Hz (dotted line). Solid line is a fit to Eq. 5.2. **b)** Noise spectrum of the same resonator at T=375 mK. **c)** For comparison: Noise spectrum of a microwave resonator made from pure aluminum ($\omega_r = 8.15$ GHz, $\kappa_r \sim 0.2$ Mhz) measured with the same experimental setup under identical conditions. Figure adapted from Ref. [190].

### 5.3.1 1/f noise background

By fitting Eq. 5.2 to the fractional noise spectrum, as shown by the solid red lines in Fig. 5.4(a) and (b), the individual contributions to the frequency fluctuations can be quantified and subsequently studied further. For this purpose, noise measurements were performed for different resonators while sweeping the sample temperatures and average resonator photon numbers $\overline{n}$. For the temperature sweeps, a constant high-power value of $\overline{n} \geq 2 \times 10^3$ was chosen, while the power sweeps were conducted at a constant base temperature of 10 mK.

The results for the $1/f$ noise amplitude $h_{-1}$ are plotted in Fig. 5.5. With respect to the photon number, one can observe a power law dependence where a comparison to $h_{-1} \propto 1/\overline{n}^{\beta}$ (solid lines) yields $\beta = 0.36\ (A1), 0.15 \pm 0.06\ (B1 - B3), 0.12 \pm 0.07\ (C1 - C3)$. The stated values were calculated from the mean of all resonators on the same sample. On the contrary, when the temperature is increased instead,

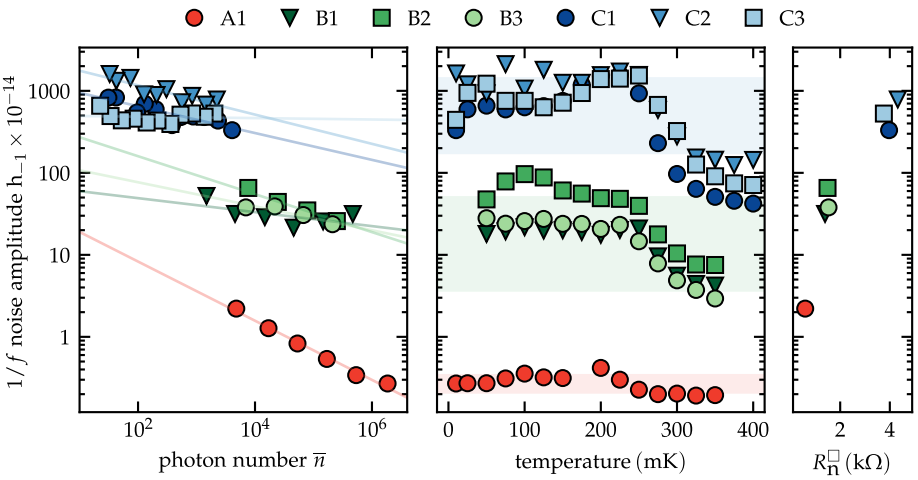


**Figure 5.5: $1/f$ noise amplitude.** First and second panel: $1/f$ noise amplitude $h_{-1}$ as a function of the photon number and the sample temperature. Straight lines are a fit to $1/\overline{n}^{\beta}$, shaded area indicate the standard deviation of all data points from the particular sample. Third panel: $1/f$ noise amplitude at $\overline{n} \sim 2 \times 10^3$ versus the sheet resistance of the respective resonator. Figure adapted from Ref. [190].

the $1/f$ noise does barely change within the standard deviation of the sample data (shaded area). Solely a slight decrease of $h_{-1}$ can be identified at high temperatures $> 250\,\mathrm{mK}$, which could be a consequence of the adjusted data acquisition rate in this temperature range and the resulting deformation of the overall noise power spectrum (Fig. 5.4(b)). Finally, comparing the amplitude of the pink noise at $\overline{n} = 2 \times 10^3$ between different samples reveals a noticeable correlation between $h_{-1}$ and the normal state resistance of the film.

The observed $1/f$ scaling of the resonator noise is a well described within the generalized tunneling model (Eq. 2.54). The model further predicts that the corresponding noise amplitude $h_{-1}$ scales with $\beta = 0.5$ at high photon numbers and $\beta \to 0$ as the photon number decreases [28], which overall agrees with the observed behavior. Also, the temperature independence of $h_{-1}$ is expected within the model, due to the relatively large photon numbers used in the temperature sweeps.

Regarding the overall noise level, granular aluminum structures appears to be much more susceptible to $1/f$ type fluctuations then resonators made from aluminum [195] (see also Fig. 5.4(c)) or comparable materials like Nb [27] or NbN [196], where

$S_y(1\,\mathrm{Hz})$ is typically on the order of $10^{-15}$.[2] This discrepancy reflects the unusually high loss tangents measured for the granular aluminum films (Sec. 5.1.1), and might similarly be explained by the participation of TLS from the amorphous $AlO_x$ within the film. Assuming that the number of TLS increases with the thickness of the inter-grain $AlO_x$ barrier, this picture could also offers an explanation for the increase of the $1/f$ amplitude with the films sheet resistance.

### 5.3.2 Random telegraph signal

For the amplitude $I$ and lifetime $\tau_0$ of the RTS signal, no clear dependence on $\overline{n}$ can be observed, despite photon numbers spanning over several orders of magnitude (Fig. 5.6). Unfortunately, resonators C1-C3 bifurcate if the number of photons gets to high and thus no data points are available for $\overline{n} \gg 10^3$. At the same time, samples A1 and B1-B3 miss data points at low photon numbers due to the fact that there, the increasing pink noise amplitude ($h_{-1}/1\,\mathrm{Hz} \gtrsim 4I^2\tau_0$) obscures the, in comparison, small RTS signal. However, comparing values between resonators at $\overline{n} \sim 2 \times 10^3$, where the data points overlap, reveals that the RTS fluctuations are more pronounced in the samples with the higher sheet resistance, which, again, agrees with the initial observations (Fig. 5.3(b)).

With regards to the sample temperature, $I$ behaves similar to the $1/f$ amplitude, i.e., it is approximately independent of $T$ over the whole range (Fig. 5.6(a)). However, one has to consider that $I \propto \delta\mathrm{RTS} \times \delta\omega_r/\delta\mathrm{RTS}$, where $\delta\omega_r/\delta\mathrm{RTS}$ is proportional to the coupling between the RTS fluctuators and the resonator and $\delta$RTS is the amplitude of the RTS process, which generally depends on the number of fluctuators, e.g., in the case of g-r noise, on the quasiparticle density [128]. Both quantities may have an opposite temperature dependency which cancel out for the overall contribution to $I$.

The RTS lifetime $\tau_0$, on the other hand, shows a strong temperature dependency above 200 mK, where, depending on the sample, it decreases by several orders of magnitude. The decreases is approximately exponential, following

$$\tau_0(T) \propto \mathrm{e}^{\frac{const.}{k_B T}}, \tag{5.3}$$

as indicated by the black line (Fig. 5.6(b)). Above 200 mK, $\tau_0$ saturates around 100 ms in almost all samples. Note that the onset of the dependence roughly coincides with the point where the thermal energy is on the order of the resonator frequencies ($k_B 200\,\mathrm{mk}/\hbar = \omega_r \approx 4\,\mathrm{GHz}$).

[2] In all these resonator noise measurements, also no traces of an RTS signal were found in the PSD.

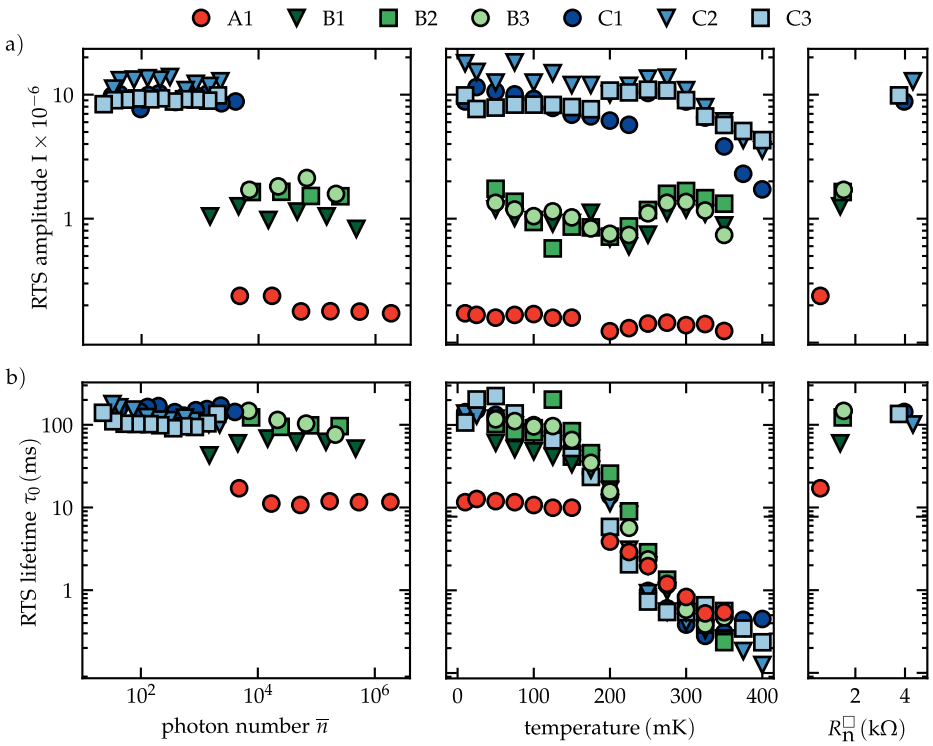


**Figure 5.6: Random telegraph signal amplitude and lifetime. a)** Amplitude $I$ and **b)** lifetime $\tau_0$ of the RTS as a function of the photon number $\overline{n}$ (measured at $T$=10 mK), sample temperature $T$ (measured at $\overline{n} = \overline{n}_{\mathrm{max.}}$) and resonator sheet resistance $R_{\mathrm{n}}^{\square}$ (measured at $T$=10 mK, $\overline{n} \approx 2 \times 10^3$). Solid line indicates an exponential temperature dependence of $\tau_0$ above 200 mK (not a fit). Figure adapted from Ref. [190].

## 5.4 Allan analysis

To support the finding presented in the previous section, the Allan deviation $\sigma_{\mathrm{y}}$ of the frequency fluctuations was calculated in addition to the PSD. In Fig. 5.7(a), $\sigma_{\mathrm{y}}(\tau)$ for data from resonator C1 at different temperatures is plotted. There, it is straightforward to identify the RTS as a distinct peak centered around $\tau_0$, while the $1/f$ component of the noise is actually flat in the Allan representation. As a consequence, it is comparably easy to directly observe the temperature dependent shift of $\tau_0$ from the data.

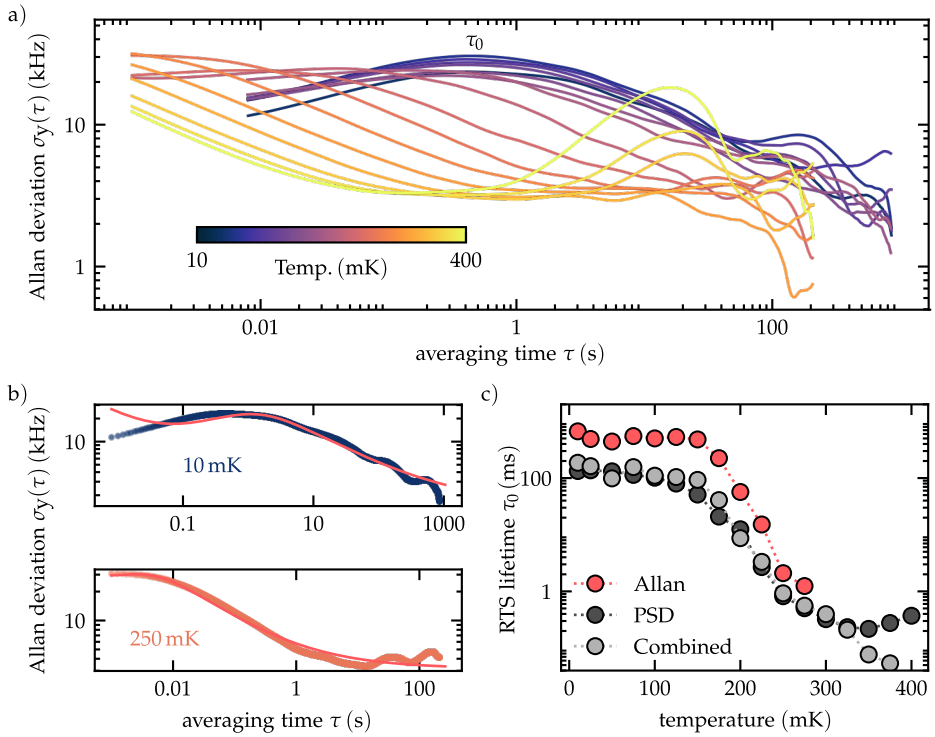


**Figure 5.7: Noise evaluation based on the Allan deviation. a)** Allan deviation $\sigma_\sigma(\tau)$ of resonator C1 plotted at different temperatures. Here, the point of highest deviation marks the lifetime $\tau_0$ of the RTS signal. **b)** Allan deviation at two specific temperatures, 10 mK and 250 mK. Solid lines are a fit to Eq. 5.4. **c)** Lifetime of the RTS $\tau$ as a function of temperature, extracted from noise measurements on C1 by fitting either the Allan deviation, the fractional noise spectrum (PSD) or both combined. Figure adapted from Ref. [190].

Using Eq. 4.13, the Allan deviation equivalent of the noise spectrum model (Eq. 5.2) can be written as [197, 198]

$$\sigma_y(\tau) = \frac{I\tau_0}{\tau}\left(4e^{-\tau/\tau_0} - e^{-2\tau/\tau_0} + 2\frac{\tau}{\tau_0} - 3\right)^{1/2} + \sqrt{2h_{-1}\log(2)} + \sqrt{\frac{h_0}{2\tau}}, \qquad (5.4)$$

using consistent naming for all noise parameters $(I, \tau_0, h_{-1}, h_0)$. A fit of Eq. 5.4 to the Allan deviation at 10 mK and 250 mK is shown in Fig. 5.7(b), to illustrate the agreement between theory and data. Further, the values for $\tau_0$ extracted from all fits on the temperature sweep data of C1 are shown in Fig. 5.7(c), together with the values obtained from fitting the PSD or PSD and Allan deviation combined. At low temperatures, all fits yield comparable $\tau_0$ values and, more importantly, show the same temperature dependency. At high temperatures, however, the fits to Eq. 5.4

do no longer converge properly due to a secondary peak appearing on the right side of $\sigma_y(\tau)$ (Fig. 5.7(a)). The amplitude of these peaks increases with temperature while the corresponding lifetime decreases. Since at temperatures above 300 mK thermally activated quasiparticle play a more prominent role, it is reasonable to assume that they are the origin of the secondary peaks (Eq. 2.32).

## 5.5 Dissipative properties

In addition to evaluating the time traces by means of Allan deviation or PSD, one can directly study the measured data points in the complex plane to identify whether the mechanism causing the noise $\delta\omega_r$ is dissipative. If so, the resonator loss rate should increase proportional to the frequency shift $\delta\omega_r \propto \delta\kappa_i$, meaning the measured data points follow a non-circular trajectory. Otherwise, all data points are expected to roughly overlap with the prerecorded resonance circle $S_{21,\,\mathrm{reso}}(f)$. An example for a mechanism that causes both, a shift of the resonance frequency as well as an increased internal loss in superconducting resonators, is the creation and recombination of quasiparticles (QPs), as discussed in section 2.3.1.

Figure 5.8(a) shows a typical set of resonator noise data in the complex plane (same as Fig. 5.3(a)), together with the prerecorded resonance circle (black line) and the expected trajectory of quasiparticles noise at $T = 100\,\mathrm{mK}$ (red line). It is apparent that the recorded data shows limited sings of dissipation, following the resonance circle rather then the quasiparticle path. An alternative way to visualize this behavior is shown in Fig. 5.8(b), where the projection distance $d_m = |S_{21,\,\mathrm{reso}}(\omega_0) - S_{21,\,\mathrm{meas}}(\omega_0)|$, i.e, length of the shortest path between each data point $n$ and the prerecorded resonance circle, is plotted over the corresponding frequency shift . There, a comparison between the measured distribution (turquoise) and the quasiparticles distribution predicted by theory (red) shows, again, a limited agreement for the relevant frequency shifts $\delta\omega_r/2\pi \geq 100\,\mathrm{kHz}$.

While the mapping distance should ideally be zero for all frequency values, this is never the case in practice, where additional sources of (predominantly amplitude) noise, e.g., from the amplifiers in the experimental setup, influence the measurement. Nevertheless, data points where $|d_m|$ equals more then 10% of the maximum mapping distance $\kappa_c/2\kappa_r$ (= radius of resonance circle) only make up a small percentage ($\sim$ 3%) of the overall data and the errors that can occur in the noise analysis from incorrectly projecting them on the resonance circle are likely negligible.

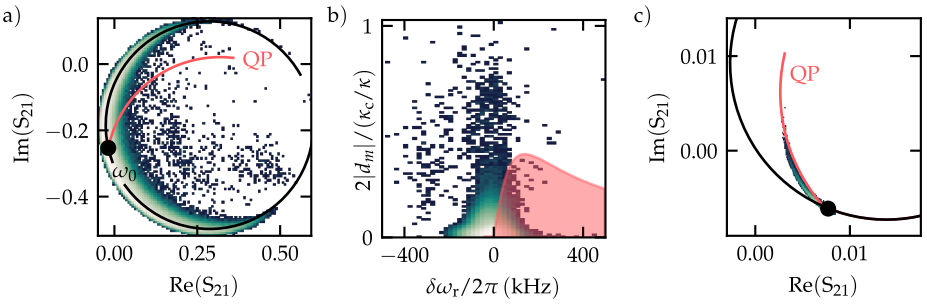


**Figure 5.8: Dissipative noise. a)** Noise data from resonator C1. Black line is a fit to the prerecorded resonance circle $S_{21,\,\mathrm{reso}}(f)$, red line indicates the trajectory expected for QP related noise. **b)** Shortest distance $d_m$ between each data point and the resonance circle, as a function of the corresponding frequency shift. Red area indicates the distribution expected for QP related noise. **c)** QP noise measured during a single cooldown of an additional resonator on sample A. Figure adapted from Ref. [190].

To verify that noise can indeed be dissipative, the noise data measured on an additional resonator of sample A is shown in Fig. 5.8(c). There, the data points tightly following the trajectory theoretically predicted by Eq. 2.39, suggesting that it suffered from particularly strong QP poisoning. Note that this behavior was only observed once, and never in any of the primarily analyzed resonators (Tab. 5.1). However, similar noise trajectories have been measured for aluminum resonators exposed to a photon flux, which is expected to continuously breaks Cooper pairs into QPs [17].

## 5.6 Discussion

While the measured $1/f$ likely originates from one or several TLS, the physical mechanism behind the RTS is less clear. At first, it seems natural to attribute both noise components to the same origin. Indeed, it has been shown in superconducting qubits [29, 30] as well as superconducting resonators [198] that a nearly resonant TLS can produce a dominant Lorentzian noise spectrum. However, a reduction of $I$ with $\overline{n}$ similar to $h_{-1}(\overline{n})$ would be expected as the resonator eventually decouples from the TLS, which is not observed in the data (Fig. 5.6). Further, due to the random nature of these defects, it is statistically unlikely to find a dominate TLS with nearly identical switching time for all resonator on a sample.

Earlier measurements studying the noise properties of narrow aluminum resonators demonstrated that QP generation and recombination also produces a Lorentzian

noise spectrum [128, 199]. In this case, the exponential decrease of the lifetime depicted in Fig. 5.6 would be expected naturally, as the QP density $n_{qp}$ increases with temperature and it becomes more likely to find a partner for recombination (Eq. 2.32). At the same time, the measured $\tau_0$ values are comparable to quasiparticle lifetimes previously observed in granular aluminum [47]. However, related studies showed that the response of a superconducting resonators to a change in the quasiparticle number $\delta\omega_r/\delta\text{RTS}$ is almost temperature independent and $\delta\text{RTS} \propto N_{qp}$ [14, 200] . Consequently, the noise amplitude $I$ should increase with temperature, contrary to its actual behavior shown in Fig. 5.6, where $I$ is approximately constant or even decreases with increasing temperature instead. In addition, the lack of dissipation associated with the fluctuations, as discussed in Sec. 5.5, speaks against a quasiparticle related origin.

The strong dependence of the RTS amplitude on the sheet resistance suggest that the origin of the RTS rather lies in the granular structure of the film, i.e., the interplay between the Josephson coupling and the Coulomb repulsion. While more exotic TLS and quasiparticle processes have been found in highly disordered samples approaching the SIT [47, 201–204] (see also Sec. 6.5), they are subjected to the same concerns brought forward for conventional atomic defects above. A scenario, that would, however, be imaginable is g-r noise due to trapped charges. If the sheet resistance of the films increases, one can make the argument that statistically, there must be some grains (or clusters of grains) that are no longer coherently coupled to the rest of the films [114]. Charges tunneling on and off these islands temporally alter the total kinetic inductance of the film, thus leading to frequency fluctuations. Moreover, because they do not contribute the resonator currents while trapped, they do not necessarily lead to dissipation, even if these charge where quasiparticles. From straightforward calculations (similar to Appendix B in Ref. [32]) one can show the fraction of grains that has to participate in charge trapping $N_{G,trap}/N_{G,tot} = 2\delta\omega_r/\omega_r = \mathcal{O}(10^{-6})$ should be directly proportional to the relative frequency shift. This could explain the increased RTS noise amplitudes in resonators with higher sheet resistances, i.e., samples closer to the SIT, where finding weakly coupled grains is more likely.

Another mechanism that becomes relevant in this regime are collective (phase) modes of the superconducting condensate, as discussed in Sec. 2.1.2. In granular aluminum, evidence of such modes has been found in THz spectroscopy [53, 76] and STM measurements [52]. With regards to frequency fluctuations, it was previously argued that modes extending down to zero frequency can be the thermally exited, leading to fluctuations also in higher energy modes due to mode-mode interaction [77]. However, the approximations made in the some of these calculation where rather crude, and more precise theories need to be developed [78, 205].

# 6 Experiments with applied electric fields

Two-level-systems in quantum circuits, particularly in fixed-frequency resonators, are usually studied indirectly by measuring noise and dissipation, as shown in the previous chapter. However, when the coupling between resonator and TLS is sufficiently large and the TLS is not far detuned from the resonator, observing a direct interaction is possible. In this chapter, such observations are reported for granular aluminum resonators, facilitated by electric and strain field tuning. A quantitative analysis of the most strongly coupled specimens reveals potentially novel TLS with anomalously large dipole moments residing near the surface of the films, particularly in oxygen rich samples. Consequently, the connection between these TLS and the resonators excess noise is studied. In the final discussion, different microscopic pictures for these unconventional TLS are considered.

## 6.1 Transmission spectrum

The standard experiment that allows to directly observe the interacting of TLS with a microwave resonator, according to Eq. 2.53, are measurement of the transmission coefficient $S_{21}^{reso}$ in a spectral window $\Delta\omega$ around the resonance frequency (resonator transmission). In this work, $\Delta\omega/2\pi = (\omega - \omega_\mathrm{r})/2\pi \in [-2\,\mathrm{MHz}, 2\,\mathrm{MHz}]$ was typically chosen, with a resolution of 401 individual frequency points. During such a measurement, electric and strain fields can be applied to the resonators using a DC electrode and piezo actuator (see Sec. 4.2.3 for details). These field modify the frequency of the TLS according to

$$\omega_\mathrm{TLS} = \frac{1}{\hbar}\sqrt{\Delta_\mathrm{TLS}^2 + (\epsilon_\mathrm{TLS} + 2dE_\mathrm{z} + \gamma^* U_\mathrm{piezo})^2}, \tag{6.1}$$

allowing them to be tuned through the resonances of the studied microwave resonators. Equation 6.1 is a modified version of Eq. 2.48, where the electric field vector $\mathbf{E}$ has been replaced by the maximum field value along the film edge $E_\mathrm{z}(U_\mathrm{elec})$, which linearly depends on the voltage $U_\mathrm{elec}$ applied to the DC electrode

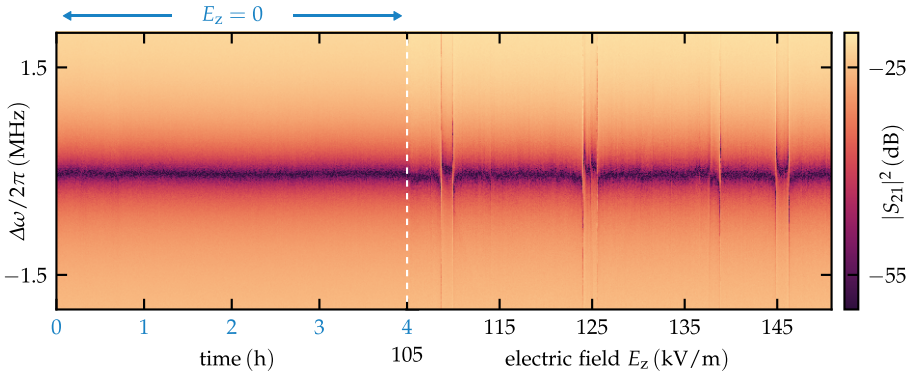


**Figure 6.1: Resonance behavior under electric fields.** Transmission amplitude $|S_{21}|^2$ in a $\Delta\omega/2\pi =$ 4 MHz window around resonator E1 versus the measurement time or electric field $E_z$. When an electric field is applied, pronounced anticrossings appear in the resonator spectrum.

(see Sec. 4.4 for details). Effectively, this field only couples to the perpendicular component of the TLS's electric dipole moment $d = |\mathbf{d}_{\mathrm{TLS}}| \cos(\theta)$, where $\cos(\theta) = \frac{\mathbf{E}\cdot\mathbf{d}_{\mathrm{TLS}}}{|\mathbf{E}||\mathbf{d}_{\mathrm{TLS}}|} < 1$. Thus, the dipole moments stated thought this chapter are only a lower estimate for the total dipole moment of the TLS $\mathbf{d}_{\mathrm{TLS}}$.

Since the conversion from the piezo voltage $U_{\mathrm{piezo}}$ to the strain field $\mathbf{S}$ is not so straightforward, the deformation potential is replaced by an effective coupling strength $\gamma^*$. For the field tuning experiments performed in the scope of this work, $E_z$ values up to 629 kV/m (40 $V_{\mathrm{piezo}}$) were applied, also in reverse polarity. Note that in the following discussion, the abbreviation TLS will be used as a general term to describe coherent quantum two level system, which not necessarily have to originate from atomic defect.

### 6.1.1 Electric fields

Figure 6.1 illustrates (using actual measurement data) how the resonator transmission changes when a static electric field is applied. For $E_z = 0$, the resonator remains relatively stable (Tab. 5.2) over the displayed four hour period. The qualitative picture changes noticeably once a increasing electric field is applied: At distinct field values $E_z^i$, avoided level crossings between the resonator and multiple TLS appear.

Within the experimental data, these TLS can be separated into two classes: strongly and moderately coupled. The strongly coupled TLS, which are the ones predominantly visible in Fig. 6.1, produce a gap large compared to the resonator linewidth

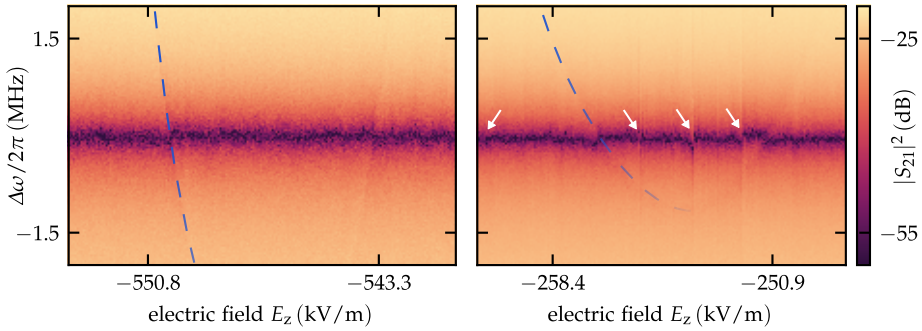


**Figure 6.2: Traces of moderately coupled two level systems.** Transmission amplitude $|S_{21}|^2$ in a $\Delta\omega/2\pi = 4\,\mathrm{MHz}$ window around resonator E1 versus $E_z$ in two selected field ranges. Dashed lines follow visible traces of two moderately coupled TLS (Eq. 6.1) with $d = \{1.9\,\mathrm{eÅ}, 1.18\,\mathrm{eÅ}\}$. White arrows indicate resonator-TLS anticrossings.

$\kappa$. An analysis of these TLS based on the corresponding anti-crossings will be presented in Sec. 6.3. The moderately coupled systems are less pronounced, but make up most ($> 98\%$) of the overall count of anticrossings. Such anticrossings are highlighted in Fig. 6.2. When, on rare occasions, the symmetry point of these TLS is close to $\omega_\mathrm{r}$ and their loss rate is low ($\gamma_{TLS} \lesssim 1\,\mathrm{MHz}$), the trace of the hyperbolic TLS spectrum (Eq. 6.1) is even directly visible in the transmission data. A fit to the two hyperbolas indicated by dashed lines in Fig. 6.2 yields TLS dipole moments of $d = \{1.0\,\mathrm{eÅ}, 1.18\,\mathrm{eÅ}\}$.

One can get an estimate for the field-density $P_\mathrm{E}$ of strongly to moderately coupled TLS in the different resonators by counting all visible avoided level crossings and hyperbolas and normalizing the count to the total range of the electric field sweep. Corresponding results from selected electric field sweeps are listed in Tab. 6.1. Note that a representative count was not possible for sample C, where anticrossings of moderate strength are obscured by the pronounced frequency fluctuations. In general, densities obtained this way are two orders of magnitudes larger then the respective field-densities $P_\mathrm{E,s}$ which only take into account strongly coupled TLS. However, both $P_\mathrm{E}$ and $P_\mathrm{E,s}$ strongly depend on the experimental implementation of the DC electrode and, more importantly, do not account for the increased visibility of TLS with larger dipole moments, i.e., hyperbolas with steeper slopes. A better estimate, suitable for comparison to other experiments with similar dielectric volumes, is given by the spectral TLS density

$$P_V = \sum_\mathbf{i} \frac{\Delta E_\mathrm{z,max}}{\tilde{d}_i}. \tag{6.2}$$

Here, i is the index over all observed TLS and $\tilde{d}_i$ is a visual estimate for their slope with respect to the electric field, which was tuned over a total range of $\Delta E_{z,max} = 1258\,\mathrm{kV/m}$. Selected spectral density values are also listed in Tab. 6.1. They are several orders of magnitude ($\sim 10^4$) smaller then the densities estimated from the loss tangent data, suggesting that the reported TLS have only a minor effect on the total dielectric loss, which instead, is likely dominated by a bath of weakly coupled TLS that are not directly observable.

**Table 6.1:** Measured TLS densities with respect to the electric field ($P_E$) and the energy spectrum ($P_V$), separately listed for all resonators with different sheet resistance values $R_n^{\square}$. The $P_{E,s}$ only counts strongly coupled TLS. On sample C, TLS counting was hindered by the pronounced frequency fluctuations.

| Reso. | $R_n^{\square}\,(\mathrm{k}\Omega)$ | $P_E\,(\mathrm{MW/m})^{-1}$ | $P_V\,(\mathrm{GHz})^{-1}$ | $P_{E,s}\,(\mathrm{MV/m})^{-1}$ |
|---|---|---|---|---|
| A1 | 0.59 | $\sim 140$ | $\sim 21$ | 1.6 |
| A2 | 0.61 | - | - | 0.4 |
| B1 | 1.39 | $\sim 290$ | $\sim 34$ | 2.0 |
| B2 | 1.49 | $\sim 250$ | $\sim 27$ | 2.4 |
| B3 | 1.53 | - | - | 2.0 |
| C1 | 3.97 | - | - | 4.0 |
| C2 | 4.32 | - | - | 4.8 |
| C3 | 3.76 | - | - | 4.0 |
| D1 | 0.65+12 | $\sim 220$ | $\sim 25$ | 2.4 |
| D2 | 0.69+12 | $\sim 260$ | $\sim 43$ | 1.6 |
| D3 | 0.71+190 | - | - | 2.0 |
| E1 | 0.68+190 | $\sim 450$ | $\sim 29$ | 4.4 |
| E2 | 0.72+190 | $\sim 410$ | $\sim 33$ | 3.2 |

### 6.1.2 Strain fields

When mechanical strain is applied to the samples instead of an electric field, the qualitative picture remains the same, as shown in Fig. 6.3(a). However, the prevalence of pronounced anticrossing from strongly coupled TLS is noticeably reduced in these experiments. This could either be due to a reduced sensitivity of these TLS to strain tuning, or the strain field generated per Volt applied to the piezo is comparably low, i.e, $\gamma^* V_{piezo} \ll dE_z$. Further, strain measurements are always hysteretic due to piezo creep. As a consequence, measurements with electric fields, which also allow determining the TLS' electric dipole, were favored in this work.

In addition to the occurrence of anticrossings, the strain field also results in a linear shift $\delta\omega_r$ of the resonator frequency, as shown in Fig. 6.3(b) for resonator

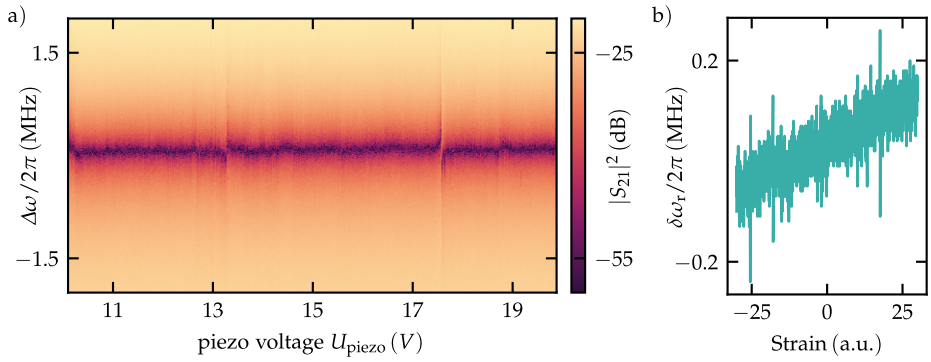


**Figure 6.3: Resonator strain tuning experiments. a)** Transmission amplitude $|S_{21}|^2$ in a$\Delta\omega/2\pi =$ 4 MHz window around resonator E1 versus the voltage $U_{\text{piezo}}$ applied to the piezo actuator. **b)** Resonance frequency $\omega_r$ shifting as a function of the piezo voltage.

E1. For this sample, a maximum frequency difference of 200 kHz over the whole measurement range ($\Delta U_{\text{piezo}} = 80$ V) can be observed. A possible explanation for this behavior comes from the strong dependency of the film's transport properties on the inter-grain coupling, which naturally changes when the sample is bent. Because the dependency on the strain is linear rather than random, it seems likely that only a single pair of neighboring grains, which dominates the transport of the resonator currents [34], is relevant in this process.

## 6.2 Resonator broadening

Due to their (typically) short lifetimes, TLS tuned on resonance present a very effective loss channel, resulting in a measurable resonance broadening. This effect has long been used to reveal and study TLS traces (Eq. 6.1) over a large frequency range using tunable qubits [25, 135]. While such traces are generally not accessible with fixed-frequency resonators, measuring the increase of $\kappa_r$ provides a single measure for the identification of an TLS anticrossing (instead of having to inspect the whole resonator spectrum), which is advantageous when additional experimental parameters.

In Fig. 6.4 the dependency of the TLS-resonator interaction on the average resonator photon number is studied. At low photon numbers ($\overline{n} = \mathcal{O}(10^2)$), a roughly 50% increase of the resonator's loss rate, i.e., resonator broadening, is visible at two distinct electric field values. As the photon number increases, the corresponding peaks become progressively less pronounced. At $\overline{n} > 10^4$ they are no longer

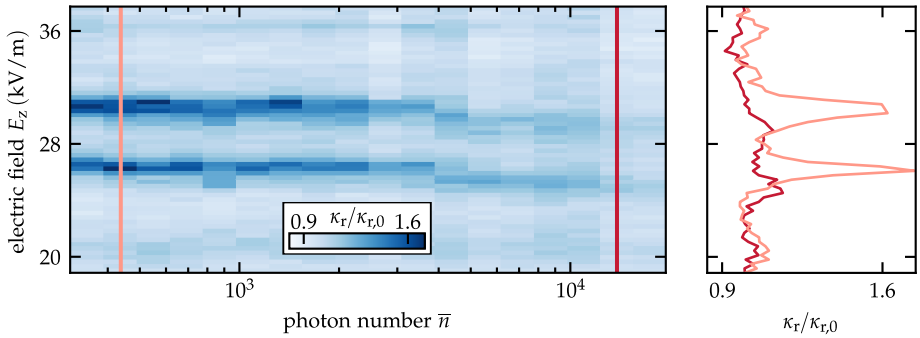


**Figure 6.4: Power dependence of the resonator TLS coupling.** Normalized loss rate $\kappa_r/\kappa_{r,0}$ of resonator E1 as a function of the electric field $E_z$ and the average resonator photon number $\overline{n}$. Near an anti-crossing, $\kappa_r$ is enhanced significantly. At higher photon numbers ($\overline{n} > 10^3$) the enhancement progressively gets washed out and eventually disappears.

visible and $\kappa_r$ is approximately constant over the observed electric field range. Such behavior is only expected for a quantum two-level-system, who can absorb one single photon at a time. Thus, as the number of photons circulating in the resonator surpass a certain threshold, it is no longer sensitive towards loosing a single one of them to the TLS. Consequently, there is strong evidence that the observed anticrossings indeed stem from coherent TLS and are not due to, for example, on chip resonances, which could absorb more than one photon and would not disappear as $\overline{n}$ increases. Note that, for the same reasons, the anticrossings are only visible in the resonator spectrum if the data is measured at low photon numbers, typically $\overline{n} \leq 500$.

In a second experiment, the resonator broadening in a wide electric field range was monitored for over 50 hours (Fig. 6.5). The measured TLS resonances, i.e., the electric field values $E_z^i$ at which $\kappa_r$ is increased, fluctuate noticeable over this period. One can observe a telegraphic-like switching pattern for one of the TLS, sudden jumps to a different frequencies or slow drifting. This, together with the presence of correlated TLS resonance fluctuations, seen ,e.g., at $E_z > 42\,\mathrm{kV/m}$ between hours eleven and thirteen, are the expected signatures of interacting TLS [27, 28, 30, 206].

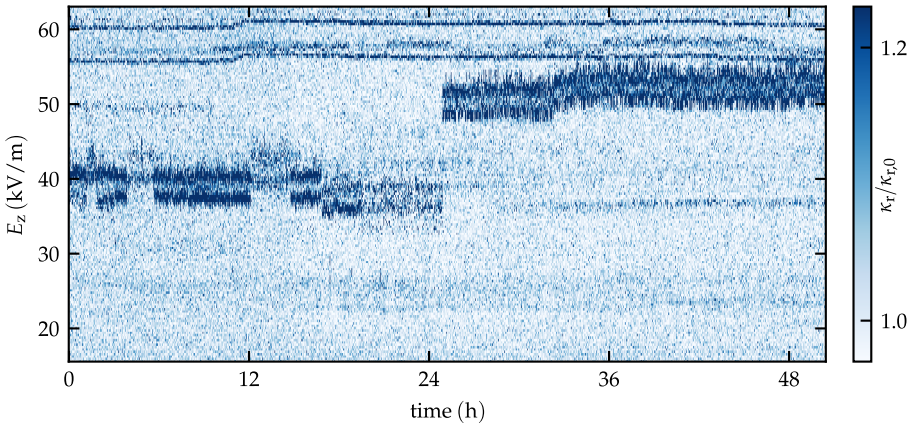


**Figure 6.5: Temporal stability of several TLS.** Normalized loss rate $\kappa_r/\kappa_{r,0}$ of resonator E1 as a function of the electric field $E_z$ measured over a two day period. The data reveal various types of temporal fluctuations discussed in the text.

## 6.3 Anticrossing analysis

By applying input-output theory to the combined Hamiltonians of Eq. 2.52 and Eq. 3.9, one can obtain an analytical expression for the transmission spectrum of an asymmetric resonator strongly coupled to a two-level-system [146]. Adopting the form of Eq.3.15, this expression reads

$$S_{21}^{\text{anti}}(\omega, E_z) = ae^{i\alpha_0}\left(1 - \frac{\frac{\kappa_c}{2}e^{i\Phi}}{\frac{\kappa_r}{2} + i(\omega-\omega_r) + \frac{g^2}{i\left(\omega - \frac{1}{\hbar}\sqrt{\Delta_{\text{TLS}}^2 + (\epsilon_{\text{TLS}}+2dE_z)^2}\right) + \frac{\gamma_{\text{TLS}}}{2}}}\right), \tag{6.3}$$

including the dependency of the TLS frequency on $E_z$. By fitting this formula to an anticrossing, all relevant TLS parameters can be extracted. There, the quantities of particular interest are the coupling strength between resonator and TLS $g$, the parallel component of the TLS dipole moment $d$ as well as the TLS linewidth $\gamma_{TLS}$, which relates to the coherence time of the TLS as $T_2 = 2/\gamma_{TLS}$.

From the eleven fitting parameters used in Eq. 6.3, six describe the resonator ($[a, \alpha_0, \kappa_c, \Phi, \kappa_r, \omega_r]$) and five characterize the TLS that is tuned through the resonance ($[g, \Delta_{\text{TLS}}, \epsilon_{\text{TLS}}, d, \gamma_{TLS}]$). Having such a large number of free parameters, the analysis is rather susceptible to overfitting. To avoid such behavior, fitting is performed in two steps. First, a reduced model $|S_{21}^{\text{anti}}(\omega, g=0)| = |S_{21}^{\text{reso}}(\omega)|$ is

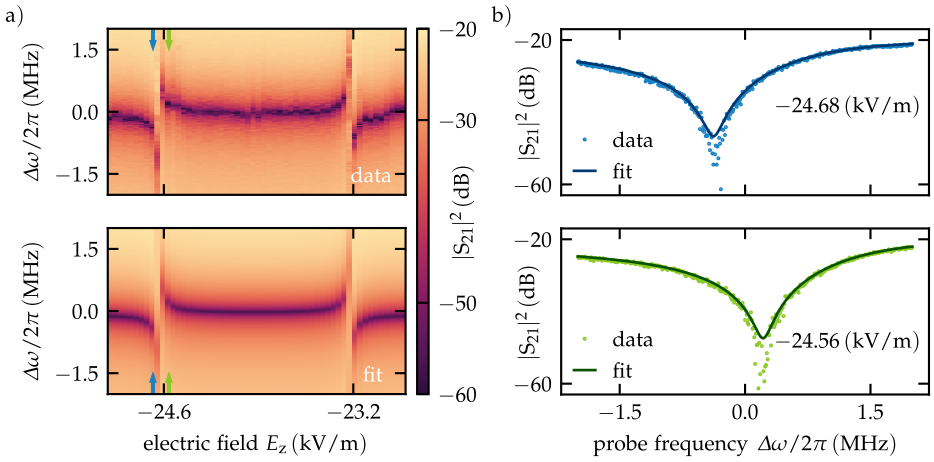


**Figure 6.6: Anticrossing analysis a)** Top panel: Transmission amplitude of resonator E1 interacting with a strongly coupled TLS that is tuned through resonance by the applied electric field $E_z$. Bottom panel: Fit of Eq. 6.3 to the experimental data. Colored arrows mark the individual traces displayed in b).

fitted to the bare resonance at a selected electric field value where all strongly coupled TLS are far detuned from the resonator. The parameters obtained this way are then fixed for all further analysis performed on that particular resonator. In the second step, the full model $|S_{21}^{\text{anti}}(\omega, E_{\text{elec}})|$ is fitted to the 2D amplitude transmission data in the vicinity of the anticrossing of interest.

For both steps, a standard non-linear least squares method is used. In addition to this two step process, only symmetric anticrossing pairs were selected for fitting, which practically fixes the value of $\Delta$. The results of a typical fit are shown in Fig. 6.6. As illustrated by the cuts through the 2D data, the minimum of the transmission shows deviations from the unperturbed resonance ($\Delta\omega = 0$) with opposite signs, as expected on the two sides of an anticrossing. Note that due to the logarithmic scale, deviations between data and fit near the transmission minimum appear exaggerated.

### 6.3.1 TLS parameters

In total, 86 fits were performed on all pronounced anticrossings measured during two cooldowns of all samples (see D.2 for a extended selection of anticrossing fits and D.1 for tables containing all relevant fit parameters). Figure 6.7(a) shows the corresponding distribution of TLS linewidths, ranging from 0.2 to 80 MHz.

With an average linewidth value $\overline{\gamma}_{\mathrm{TLS}}/2\pi \approx 14\,\mathrm{MHz}$ corresponding to a coherence times of hundreds of nanoseconds, this range is, while rather broad, comparable to TLS lifteimes found in similar studies on superconducting qubits [178, 207] and distributed microwave resonators [143, 146, 147].

The values obtained for the coupling strength $g$ and the parallel dipole moment $d$ are plotted in Fig. 6.7(c). There is a strong correlation between the two quantities ($r = 0.62$), as expected for $g \propto E_{\mathrm{rms}} d$.[1] Using Eq. 6.2, the average spectral density of the strongly coupled TLS can be calculated to be $\overline{P}_{\mathrm{V},g} \approx 0.01\,(\mathrm{GHz})^{-1}$, which is, again, much lower than the respective density including moderately coupled TLS (Tab. 6.1).

The shaded area in Fig. 6.7(c) indicates the parameter space, in terms of dipole moment and coupling strength, that would be expected for conventional atomic defect type TLS [21, 22]. The numerous experiments studying those systems typically find TLS with electric dipoles $\mathbf{d}_{\mathrm{AD}}$ below a maximum value of roughly 2 eÅ [6, 23, 148, 208–211]. Here, in granular aluminum, the most strongly coupled TLS show, however, order of magnitude larger dipole moments up to 40 eÅ, suggesting an alternative microscopic origin.[2]

Further, looking at the difference between the TLS measured on the individual samples, one can make several noteworthy observations. First, in Fig. 6.7(c), TLS with a coupling strength of $g/2\pi > 2\,\mathrm{MHz}$ are only observed on samples without an insulating top layer (A-C). This supports the assumption that these novel TLS are (also) located near the film surface. Since resonant modes, i.e, the oscillating charge carriers, preferably exist in the lower, superconducting layer, the resonator fields are reduced inside the insulating top layer. Consequently, TLS near the film-air interface are exposed to reduced values of $E_{\mathrm{rms}}$. Second, as illustrated by Fig. 6.7(d), the number of strongly coupled TLS increases with the normal state sheet resistance $R_{\mathrm{n}}$ (indicated by darker color shades), i.e, the transparency of the inter-grain oxide barrier. Considering the field distribution discussed above, this trend partially holds true even for the insulating layers. In particular, the TLS density in sample E is noticeable higher then in sample A, despite an almost identical superconducting layer. Similarly, the average TLS dipole moment ($\overline{d}$) and coupling strength ($\overline{g}$) are

[1] The TLS linewidth is also correlated with both, the coupling strength $g$ ($r = 0.75$) and the dipole moment $d$ ($r = 0.39$). There, the stronger correlation with $g$ seems to rather be an artifact of the fitting procedure then of an physical origin, given that $\kappa_{\mathrm{r}} < \gamma_{TLS}$, i.e, the resonator can not be the main loss channel of the TLS.

[2] Note that $d$ is only a lower estimate for the electric dipole of the measured TLS, assuming it is parallel to the electric field. Thus, even when allowing for large errors in Fig. 6.7(c), this overall conclusion still holds.

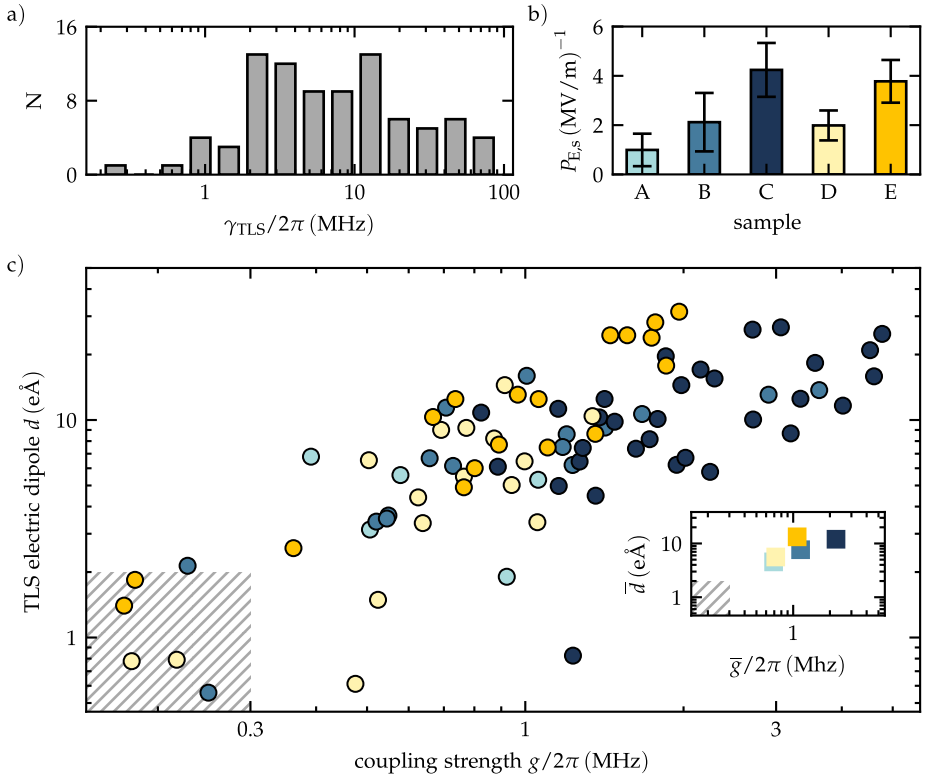


**Figure 6.7: Properties of all individually analyzed TLS (N=86). a)** Histogram of all measured TLS linewidths $\gamma_{TLS}$. **b)** Field density $P_{E,s}$ of strongly coupled TLS found on the individual samples ($A$ : 0.6 kΩ, $B$ : 1.5 kΩ, $C$ : 4.1 kΩ, $D$ : $E$ : $0.7 + 12$ kΩ, $E$ : $0.7 + 190$ kΩ). Error bars indicate variations between different resonators and cooldowns. **c)** Distribution of the extracted resonator-TLS coupling strengths $g$ and parallel TLS dipole moments $d$. Single layer samples are colored in shades of blue, two-layer samples in shades of yellow. Darker shades indicate higher sheet resistance. Hatched area marks the parameter space expected for conventional atomic defects type TLS. Inset shows the average values for $d$ and $g$ measured on each sample.

higher in samples with higher sheet resistance (see inset Fig. 6.7(c)). Considering the selection process of only fitting pronounced anticrossings, this effect could be correlated with the differences in the TLS densities. Either way, one can attest a prevalence of TLS with large dipole moments to films with increasing oxygen concentrations.

### 6.3.2 TLS location

For the anticrossing analysis presented so far, the actual position of the TLS along the film edge was disregarded. Instead, all TLS were expected to be subjected to the maximum field $E_z$. This allowed for a direct conversion of the measured, effective coupling strength $p^* = 2dE_z/U_{\mathrm{elec}}$, to the parallel electric dipole moment $d$ (see Sec. 4.4 for details). However, treating the problem in a more general way, one has to write the following equation for the parallel TLS dipole moment

$$d_{\mathrm{p}^*} = \frac{p^* U_{\mathrm{elec}}}{2|\mathbf{E}_{\mathrm{elec}}(U_{\mathrm{elec}}, x_{\mathrm{r}})|}, \tag{6.4}$$

where $x_{\mathrm{r}}$ is the TLS' position along the film edge. While the distribution of the electric field is known from simulations (Fig. 4.10d)), the problem in Eq. 6.4 is to obtain $x_{\mathrm{r}}$. For this purpose it is necessary to use additional experimental data, i.e., the extracted coupling strength. Considering that near the symmetry point of the TLS hyperbola $\hbar\omega_{\mathrm{TLS}} = \Delta_{\mathrm{TLS}}$, it follows from Eq. 2.51 that

$$d_{\mathrm{g}} = \frac{\hbar g}{|\mathbf{E}_{\mathrm{rms}}(U_{\mathrm{rms}}, x_{\mathrm{r}})|}, \tag{6.5}$$

where $d_{\mathrm{g}}$ is the component of the TLS' electric dipole moment parallel to the resonator field. Because $\mathbf{E}_{\mathrm{rms}} \parallel \mathbf{E}_{\mathrm{elec}}$ at the film surface, $d_{\mathrm{g}}$ and $d_{\mathrm{p}^*}$ should be identical for each individual TLS and one can explicitly solve Eq. 6.4 and Eq. 6.5 for $x_{\mathrm{r}}$ by minimizing

$$\min_{x_{\mathrm{r}} \in [0,50]} |d_{\mathrm{g}}(x_{\mathrm{r}}) - d^*_{\mathrm{p}}(x_{\mathrm{r}})|. \tag{6.6}$$

The resulting distribution of TLS positions is plotted in Fig. 6.8(a). Contrary to an earlier work resolving the positions of conventional defect type TLS at the various interfaces of a coplanar waveguide qubit circuit [6], the TLS studied here do not concentrate at the bottom film edge ($x_{\mathrm{r}} = 0$). Instead, they are rather equally distributed along the film edge, while some even reside on the top surface. Whether this discrepancy originates in the different nature of these TLS or the different field distribution remains unknown. Also note that, because of the assumptions necessary for Eq. 6.6, the analysis is limited to the film-air interface.

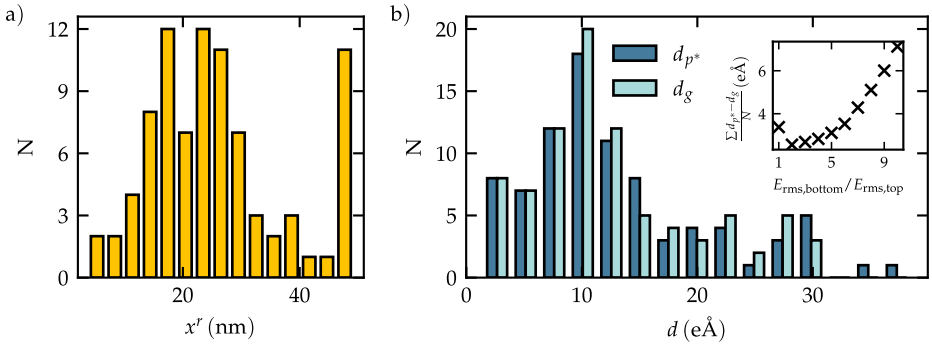


**Figure 6.8: Resolving TLS locations through electric field matching. a)** Histogram of the TLS positions along the film edge obtained from Eq. 6.6. **b)** Comparison between the distributions of TLS dipole moments calculated either from the coupling to the electrodes electric field ($d_{\mathrm{p}}^*$) or the coupling to the resonator ($d_{\mathrm{g}}$), using knowledge of the TLS location $x_{\mathrm{r}}$. Inset shows the overlap between the distributions as a function of the resonator field amplitude seen by the TLS in the two-layer sample ($E_{\mathrm{rms,top}}$), relative to $E_{\mathrm{rms,top}} = E_{\mathrm{rms}}$. The histograms in a) and b) are generated for $E_{\mathrm{rms,top}} = E_{\mathrm{rms,bottom}}/2$.

Reinserting the obtained $x_{\mathrm{r}}$ values into Eq. 6.4 and Eq. 6.5 yields two distributions for the TLS dipole moments, $d_{\mathrm{p}^*}(x_{\mathrm{r}})$ and $d_{\mathrm{g}}(x_{\mathrm{r}})$, which, for consistency, should be identical. Figure 6.8(b) shows these distributions. There, discrepancies at large dipole values could be explained by local variations of the field due to the nanoscopic structure of the film. For a good agreement, one also has to consider that the TLS residing in the top layer of sample D and E are likely subjected to smaller resonator fields. The inset in Fig. 6.8(b) shows the mean deviation between the two distributions, assuming a reduction of the $E_{\mathrm{rms}}$ field for all TLS from the two layer samples. The deviation is smallest for $E_{\mathrm{rms,top}} = E_{\mathrm{rms,bottom}}/2$, but remains reasonable up to a factor of ten when compared to the average dipole moment $\overline{d} = 15\,\mathrm{eÅ}$.

Finally, the two methods for obtaining the dipole moments from the slope of the TLS hyperbola, either using the maximum electric field ($d$) or considering the field distribution and TLS location ($d_{\mathrm{p}}^*$), should be compared. Taking $E_{\mathrm{rms,top}} = E_{\mathrm{rms,bottom}}$, the mean deviation can be calculated to $\sum_{n=1}^{86} |d - d_{\mathrm{p}}^*|/N = 2\,\mathrm{eÅ}$, which is even smaller than the deviation between $d_{\mathrm{p}}^*$ and $d_{\mathrm{g}}$. This result not only validates the initial approach to evaluate all TLS at the position with the maximum field, but also attests to the solidity of the presented data.

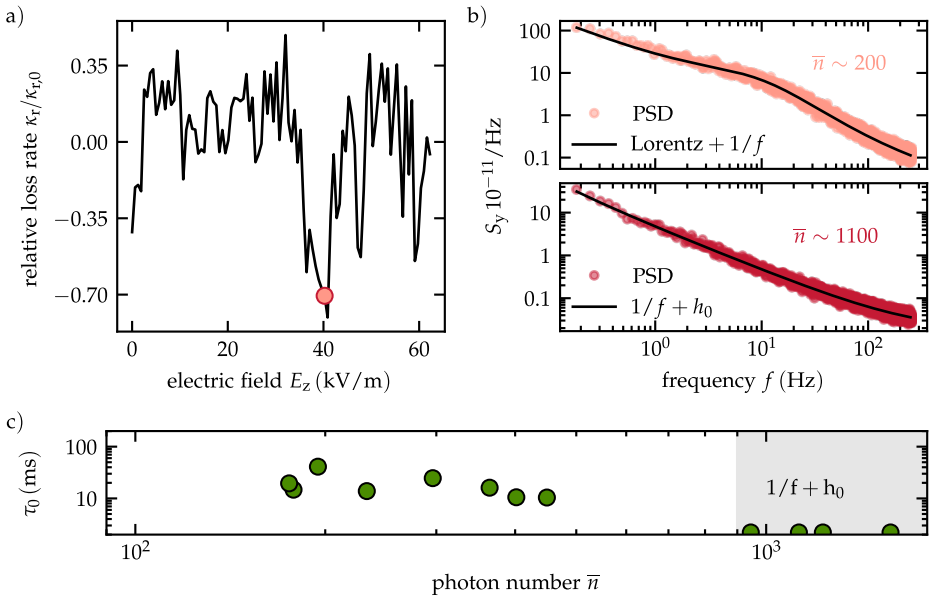


**Figure 6.9: Noise spectroscopy of a strongly coupled TLS. a)** Loss rate $\kappa_r$ of resonator C3 as a function of the electric field. The red dot indicates the field value chosen for the noise spectroscopy. **a)** Fractional noise spectrum in the vicinity of an anticrossing ($E_z = 40.24\,\mathrm{kV/m}$), recorded at different resonator photon numbers $\overline{n}$. Solid line is a fit to Eq. 5.2. **a)** Average lifetime $\tau_0$ of the RTS signal manifesting as a Lorentzian in b), as a function of $\overline{n}$. For photon numbers $\overline{n} \leq 10^3$, the Lorentzian disappears ($\tau_0 = 0$) and the noise spectrum is well described by $1/f$ noise over a white noise floor.

## 6.4 Field dependent frequency fluctuations

In Sec. 6.2, the strong temporal instability of the strongly coupled TLS were revealed, including signatures of random telegraph signals (RTS). To study these fluctuations further, the techniques presented in Sec. 5 were utilized in combination with the DC electrode. The corresponding experiment is conceptualized as follows. First, the resonator linewidth is monitored for a range of electric field values to identify TLS anticrossings by a reduction in $\kappa_r$ (Fig. 6.9(a)). Second, a specific electric field value in the vicinity of one anticrossing, where the influence of the TLS on the resonator is significant enough is chosen. It is crucial not to tune the TLS to close to the resonator, because then the two systems hybridize an the resonator can no longer be measured individually (Eq. 2.53). Third, the low frequency noise of the resonator (strongly coupled to a particular TLS) is recorded.

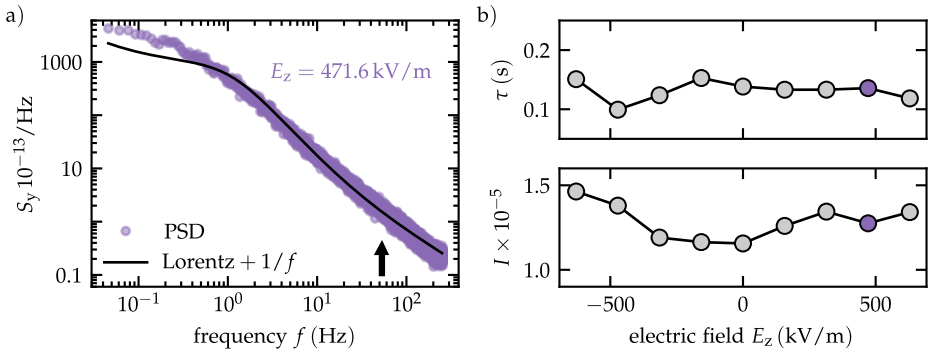


**Figure 6.10: Resonator noise spectrum versus electric field. a)** Fractional noise spectrum of resonator C3 under an applied electric field, similar to data taken at $E_z = 0$ (Fig. 5.4). Solid line is a fit to Eq. 5.2 and the arrow indicates the position of the TLS Lorentzian peak measured in Fig. 6.9. **b)** Amplitude $I$ and lifetime $\tau_0$ of the resonator RTS as a function of the electric field.

Figure 6.9(b) shows the corresponding fractional noise spectra of resonator C3, measured at two different photon numbers. To avoid a drift of the TLS resonance during the resonator frequency tracking, the overall measurement time was greatly reduced, resulting in a smaller spectral window. For $\overline{n} = \mathcal{O}(10^2)$, the noise spectrum shows clear signatures of an RTS on top of a $1/f$ noise background. A fit to Eq. 4.2 yields a average lifetime of the RTS fluctuations on the order of 10 ms, approximately independent of $\overline{n}$ at low photon numbers (fig. 6.9(c)). This result is close in value to earlier measurements revealing the fluctuation rate of TLS coupled to superconducting qubits [212]. It is, however, smaller than the $\tau_0$ values of the field-independent RTS fluctuations found across all samples (Fig. 5.6(b)). As expected, at high photon numbers $\overline{n} \gtrsim 10^3$, the resonator decouples from the TLS and the noise spectrum reverts to a $1/f$ noise between 1 Hz an 100 Hz. This contradicts the behavior of the fluctuations studied in Sec. 5, which remain unchanged even at very high photon numbers $\overline{n} > 10^4$ (Fig. 5.6(a)).

To further investigate a possible connection between the observed TLS and the power independent RTS, the (full) resonator noise spectrum was measured at nine field values equally spaced within $\Delta E_{z,\mathrm{max}}$, including $E_z = 0$. The results are summarized in Fig. 6.10. Not only does the RTS consistently appear in the noise spectrum at all field values, but its characteristics (amplitude $I$, lifetime $\tau_0$) also remain virtually unchanged. It is thus unlikely that the physical process causing these fluctuations couples to the resonator via a electric dipole-dipole type interacting, like TLS typically do, because a sufficiently large field would eventually tune the dipole away from the resonator. Note that an interpretation assuming a different coupling mechanism, e.g, due to localized charges modifying

the current transport channels within the resonator film, could also be in line with the observed power independence of the excess fluctuations studied in Sec. 5.

## 6.5 Discussion

As mentioned above, the majority of TLS measured in this work is only moderately coupled to both the resonator and the DC field, and can well be attributed to an atomic defect (AD) type origin. However, some TLS, which appear as very pronounced anticrossings, show anomalously large dipole moments and require a different macroscopic picture. Some potential candidates are illustrated in Fig. 6.11 and will be discussed in the following.

In two very recent publications, TLS with electric dipole moments of similar size have been observed in amorphous silicon [213] as well as tantalum [214] by applying a low frequency electric-field bias, which results in frequency dependent resonator loss due to a Landau-Zener type interaction [215]. The authors of Ref. [213] interpreted their findings in the scope of a two-TLS model [216]. There, TLS are separated, similar to this work, into a weakly and a strongly interacting variety, where the latter can have very large electric dipole moments. For these large TLS, an Efros-Shklovskii-type mechanism due to phonon mediated TLS-TLS interaction creates a gap in their energy spectrum at the relevant energies if the system is in the equilibrium [217, 218]. While, consequently, they are usually not observed in experiments with static fields (like the ones presented here), it has been shown that granularity can modifies the phonon spectrum [219, 220], which might hinder TLS-TLS interactions and lift the gap. For this mechanism to be effective, such TLS, which might be formed by tunneling nanoclusters (TN) containing hundreds of atoms [221], have to sit between the grain boundaries rather than on the surface of the film. Since the expected static field penetration depth on the order of the Thomas-Fermi lenght $\lambda > \lambda_{\mathrm{TF}} \simeq 2\,\mathrm{nm}$ is comparable to the thickness of the films, i.e, the global field $E_z$ does not only penetrate the surface oxide but also the oxide between the grains, this picture does not contradict our findings.

However, the increased densities of strongly coupled TLS in films with higher sheet resistances (Fig. 6.7(b)) suggest that the underlying physics is rather related to the suppression of superconductivity in these films than structural phenomena, which are less sensitive to changes in $R_{\mathrm{n}}$. A potential candidate in this regard are quasiparticles (QP) that have been trapped within local minima of the gap $\delta\Delta$, which can arise, e.g., from weak magnetic impurities or film inhomogeneities [52, 98]. Within this trap, the QP only has few bound states and as a results, behaves similar to a TLS (see Fig. 6.11). Such behavior has recently been reported for

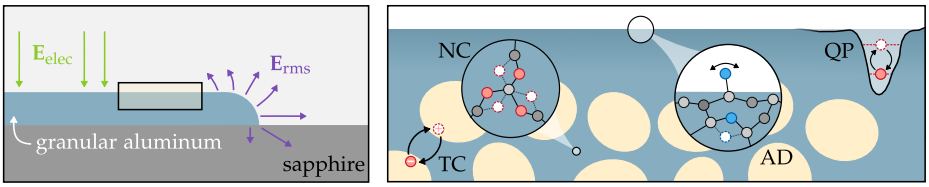


**Figure 6.11: Potential TLS candidates near the surface of a granular aluminum thin film.** Left panel: Illustrative side view of the sample showing the relevant electric fields. Right panel: Sketch of the granular aluminum film surface, illustrating conventional atomic defects (AD, blue) as well as potential candidates with larger dipole moments (red). The latter includes charges trapped on or between grains (TC), tunneling nanoclusters of atoms (NC), or quasiparticles trapped in spatial variations of the superconducting gap (QP).

disordered niobium nitride (NbN) films [201], where the measured dipoles were on the order of 1 eÅ. Due to the, in comparison to granular aluminum, increased coherence length ($\xi_{0,\mathrm{grAl}} \approx 2\xi_{0,\mathrm{NbN}}$) but reduced charge carrier of NbN, one can expect wider ($\sim \xi_0^3$) traps which are also shielded by less charges in granular aluminum, allowing for much larger dipole sizes. At the same time, the traps ($\delta\Delta/k_\mathrm{B} \approx 500\,\mathrm{mK}$) can be expected to be shallower in granular aluminum, which has a smaller gap than NbN ($\Delta_\mathrm{grAl} \approx 0.2\Delta_\mathrm{NbN}$). As a consequence, the spectral distribution of the TLS frequencies, which approximately scales as $\Delta\xi_0^2$, should be comparable in both materials.

In Ref. [201], quasiparticle TLS were, among other things, identified because they rearranged under mild thermal cycling, a behavior that is not expected for atomic defects. Such studies were also performed in the course of this work (see D.3), but did not yield conclusive results. There, the problem was that due to the extensive frequency fluctuations of the strongly coupled TLS (Fig. 6.5), one can not reliably distinguish between thermal rearrangement and temporal instabilities. At the same time, these fluctuations could be explained by the expected shallower $\delta\Delta$, which would be more susceptible to thermal reconfiguration. Finally, note that the QP traps, which naturally occur on the film surface, could also exist in the insulating layer covering sample D and E, where superconductivity might still exist locally [99, 114, 222].

Historically, a popular concept to explain very strongly coupled TLS are tunneling charges (TC). So far, evidence for there existence has been found in Josephson junctions [223, 224] and Nb+Pt resonators [149]. In granular aluminum films, it is easy to believe that localized charges occur naturally when the the sample approaches the SIT and the Coulomb repulsion surpasses the Josephson coupling [114] (see also Sec. 2.2.2). One can estimate that by simply hopping between

adjacent grains which are separated by a $\sim 2-3\,\mathrm{nm}$ thick oxide barrier, a single Cooper pair could from dipoles exceeding $100\,\mathrm{e\AA}$. In reality, the dipole would, of course, appear noticeably smaller due to electrical shielding by the surrounding condensate. While this simple estimation yields dipoles on the same scale as those observed, the problem with the trapped charges is that the typical grain charging energy on the order of several Kelvin does not agree with the observed TLS frequencies. However, theoretical calculation have shown that hopping charges can be dressed by phononic states of neighboring grains [225] or virtual tunneling processes [118], renormalizing the TLS energy.

The localization of charges near the SIT is directly linked to local fluctuations of the phase of the superconducting order parameter, which favors the emergence of phase modes. In particular, the random distribution of grains and barrier widths in granular aluminum naturally gives rise to a broad distribution for the local phase stiffness $J_{ij} = E_\mathrm{J}$ [76], spawning low-energy phase modes with an effective dipole moment (Eq. 2.14). Physically, such modes could be thought of as Cooper pairs coherently hopping across several grains [78]. The expected localization lenght of these modes on the order of the coherence lenght ($\xi_\mathrm{GL} \approx 10\,\mathrm{nm}$) should provide sufficiently large dipole moments. Note, however, that it is not entirely clear whether a interaction between the collective modes of the Cooper pair condensate and the resonator mode would necessarily have to be of a dipole-dipole type [77].

Since a few strongly coupled TLS are also observed in the strain tuning experiments, one has to consider how the potential candidates discussed above would couple to a strain field: Within the two-TLS model, this coupling is not only assumed but also detailed [216]. For trapped quasiparticles, it seems reasonable to assume that stress locally modifies the phonon spectrum and thus the landscape of gap fluctuations. Similarly, bending the sample modifies the distance and thus coupling between grains, leading to modified tunneling probabilities (i.e., phase stiffness) for trapped charges. Note that both these effect might also play a role in the observed change to the (AC) transport properties of the films with applied strain (Fig. 6.3(b)).

# 7 Conclusion

The goal of this thesis was to answer the following two questions: *"Do noise and dissipation in granular aluminum resonators increase with the sheet resistance of the sample?"* and *"Can (excess) TLS be directly measured in granular aluminum films?"*. Both these question could be answered affirmatively. For this purpose, multiple granular aluminum films were sputtered at different oxygen partial pressures and subsequently structured into resonant microwave circuit using standard lithographic techniques. There, different mechanism to determine the sheet resistance of the sample were implemented, ensuring a confident estimate. The superconducting samples with the highest oxygen concentration were fabricated to have sheet resistance values close to the superconductor to insulator transition. To be able to also study films on the insulating side of this transition, two samples were fabricated with an additional, insulating top layer.

To measure the noise properties of the resonators, a frequency tracking technique using the complex sample transmission together with a pre-recorded resonance circle was developed. With this tool, time series of the resonator's frequency fluctuations were measured and subsequently analyzed by means of the power spectral density and the Allan deviation. Compared to pure aluminum resonators, the granular aluminum samples showed much higher $1/f$ noise amplitudes and, in addition, signatures of a random telegraph signal (RTS) in the noise spectrum. In particular, the strength of these excess fluctuations increased with the sheet resistance of the respective resonator film. Further, the $1/f$ noise amplitude showed a power law dependence on the resonator photon number $\overline{n}$, in agreement with two-level-system (TLS) theory. When the sample temperature was increased instead, an abrupt reduction of the RTS lifetime was observed.

Subsequently, a custom made sample holder was employed to apply electrical and mechanical fields to the resonator films. Measuring the sample transmission while sweeping the strength of these fields revealed a large number of anticrossings, i.e., signatures of resonator-TLS interaction. The majority of anticrossings only showed signs of a week interaction and overall agrees with the standard TLS picture of tunneling atoms. However, a comprehensive analysis of the more pronounced anticrossings based on a quantum mechanical Jaynes–Cummings model revealed a

potentially novel type of TLS with anomalously large dipole moments reaching (measured) values up to 40 eÅ. Studying and comparing multiple samples showed that more of these TLS are observed if the sheet resistance of the film is increased.

In conclusion, the findings presented in this work demonstrate both the potential, but also the limitations of using granular aluminum in quantum circuits, where the investigated losses can, e.g, compromise the quality of a detector signal or introduce additional decoherence in nearby qubits. Possible mechanisms explaining the measurement data were extensively discussed at the end of the respective chapter. There, the universally observed dependence on the sheet resistance favors explanations that are linked to the granular structure of the material as well as the vicinity to the superconductor to insulator transition (SIT). While this would render efforts to mitigate loss and dissipation in highly oxidized samples almost impossible, it offers a unique possibility to study some of the mechanisms governing the SIT in granular materials, which are not yet comprehensively understood.

To definitively answer the question of the origin of the excess telegraph fluctuations and the giant TLS, additional theoretical and experimental effort is required in the future. For example, one could further discriminate between different TLS candidates by applying magnetic fields to the samples. In particular, TLS due to trapped quasiparticles are expected to have a strong dependency on the magnetic field due to its influence on the superconducting gap [201]. At the same time, a distributed resonator geometry like those presented in Ref. [143] or Ref. [148] might be useful to study granular aluminum films on the insulating side of the SIT more extensively. However, to draw fundamental, physical conclusions from the experimental results, additional theories have to be developed, e.g., concerning the microwave dynamic of trapped charges and collective modes near the SIT. In the meantime, the different measurement methods and evaluation tools gathered for this work offer a blueprint for similar investigations of related materials, providing further insights into the peculiarities of superconductivity in disordered films as well as their value for superconducting microwave applications.

# Bibliography


[1] M. Kjaergaard, M. E. Schwartz, J. Braumüller, P. Krantz, J. I.-J. Wang, S. Gustavsson, and W. D. Oliver: *Superconducting Qubits: Current State of Play*. Annual Review of Condensed Matter Physics **11** (2020), 369–395. DOI: 10.1146/annurev-conmatphys-031119-050605 (cit. on p. 1).

[2] W. D. Oliver and P. B. Welander: *Materials in superconducting quantum bits*. MRS Bulletin **38** (2013), 816–825. DOI: 10.1557/mrs.2013.229 (cit. on p. 1).

[3] H. Rotzinger, S. T. Skacel, M. Pfirrmann, J. N. Voss, J. Münzberg, S. Probst, P. Bushev, M. P. Weides, A. V. Ustinov, and J. E. Mooij: *Aluminium-oxide wires for superconducting high kinetic inductance circuits*. Superconductor Science and Technology **30** (2017), 025002. DOI: 10.1088/0953-2048/30/2/025002 (cit. on pp. 1, 2, 13, 14, 30, 38, 57).

[4] A. Melville, G. Calusine, W. Woods, K. Serniak, E. Golden, B. M. Niedzielski, D. K. Kim, A. Sevi, J. L. Yoder, E. A. Dauler, and W. D. Oliver: *Comparison of dielectric loss in titanium nitride and aluminum superconducting resonators*. Applied Physics Letters **117** (2020), 124004. DOI: 10.1063/5.0021950 (cit. on p. 1).

[5] A. Dutta et al.: *Study of material loss channels in tantalum microwave superconducting resonators. Quantum 2.0 Conference and Exhibition (2022), paper QTu2A.25*. Quantum 2.0. Optica Publishing Group, 2022, QTu2A.25. DOI: 10.1364/QUANTUM.2022.QTu2A.25 (cit. on p. 1).

[6] A. Bilmes, A. Megrant, P. Klimov, G. Weiss, J. M. Martinis, A. V. Ustinov, and J. Lisenfeld: *Resolving the positions of defects in superconducting quantum bits*. Scientific Reports **10** (2020), 3090. DOI: 10.1038/s41598-020-59749-y (cit. on pp. 1, 56, 79, 81).

[7] M. V. P. Altoé et al.: *Localization and Mitigation of Loss in Niobium Superconducting Circuits*. PRX Quantum **3** (2022), 020312. DOI: 10.1103/PRXQuantum.3.020312 (cit. on p. 1).

[8] J. Van Damme, T. Ivanov, P. Favia, T. Conard, J. Verjauw, R. Acharya, D. P. Lozano, B. Raes, J. Van de Vondel, A. M. Vadiraj, M. Mongillo, D. Wan, J. De Boeck, A. Potočnik, and K. De Greve: *Argon milling induced decoherence mechanisms in superconducting quantum circuits*. 2023. arXiv: 2302.03518[physics, physics:quant-ph]. DOI: 10.48550/arXiv.2302.03518 (cit. on p. 1).

[9] C. R. H. McRae, H. Wang, J. Gao, M. R. Vissers, T. Brecht, A. Dunsworth, D. P. Pappas, and J. Mutus: *Materials loss measurements using superconducting microwave resonators*. Review of Scientific Instruments **91** (2020), 091101. DOI: 10.1063/5.0017378 (cit. on p. 1).

[10] J. Zmuidzinas: *Superconducting Microresonators: Physics and Applications*. The Annual Review of Condensed Matter Physics **3** (2012), 169–214. DOI: 10.1146/annurev-conmatphys-020911-125022 (cit. on pp. 1, 19, 21, 29).

[11] S. Kogan: *Electronic Noise and Fluctuations in Solids*. Cambridge: Cambridge University Press, 1996. DOI: 10.1017/CBO9780511551666 (cit. on pp. 1, 51).

[12] E. Paladino, Y. M. Galperin, G. Falci, and B. L. Altshuler: $1/f$ *noise: Implications for solid-state quantum information*. Reviews of Modern Physics **86** (2014), 361–418. DOI: 10.1103/RevModPhys.86.361 (cit. on pp. 1, 52).

[13] A. Fragasso, S. Schmid, and C. Dekker: *Comparing Current Noise in Biological and Solid-State Nanopores*. ACS Nano **14** (2020), 1338–1349. DOI: 10.1021/acsnano.9b09353 (cit. on p. 1).

[14] J. Gao, J. Zmuidzinas, A. Vayonakis, P. Day, B. Mazin, and H. Leduc: *Equivalence of the Effects on the Complex Conductivity of Superconductor due to Temperature Change and External Pair Breaking*. Journal of Low Temperature Physics **151** (2008), 557–563. DOI: 10.1007/s10909-007-9688-z (cit. on pp. 1, 11, 19, 70).

[15] J. M. Martinis, M. Ansmann, and J. Aumentado: *Energy Decay in Superconducting Josephson-Junction Qubits from Nonequilibrium Quasiparticle Excitations*. Physical Review Letters **103** (2009), 097002. DOI: 10.1103/PhysRevLett.103.097002 (cit. on p. 1).

[16] C. M. Wilson and D. E. Prober: *Quasiparticle number fluctuations in superconductors*. Physical Review B **69** (2004), 094524. DOI: 10.1103/PhysRevB.69.094524 (cit. on p. 1).

[17] P. J. de Visser, J. J. A. Baselmans, J. Bueno, N. Llombart, and T. M. Klapwijk: *Fluctuations in the electron system of a superconductor exposed to a photon flux*. Nature Communications **5** (2014), 3130. DOI: 10.1038/ncomms4130 (cit. on pp. 1, 69).

[18] A. Bespalov, M. Houzet, J. S. Meyer, and Y. V. Nazarov: *Theoretical Model to Explain Excess of Quasiparticles in Superconductors*. Physical Review Letters **117** (2016), 117002. DOI: 10.1103/PhysRevLett.117.117002 (cit. on pp. 1, 19).

[19] K. Serniak, M. Hays, G. de Lange, S. Diamond, S. Shankar, L. D. Burkhart, L. Frunzio, M. Houzet, and M. H. Devoret: *Hot Nonequilibrium Quasiparticles in Transmon Qubits*. Physical Review Letters **121** (2018), 157701. DOI: 10.1103/PhysRevLett.121.157701 (cit. on pp. 1, 19).

[20] M. McEwen et al.: *Resolving catastrophic error bursts from cosmic rays in large arrays of superconducting qubits*. Nature Physics **18** (2022), 107–111. DOI: 10.1038/s41567-021-01432-8 (cit. on pp. 1, 19).

[21] W. A. Phillips: *Two-level states in glasses*. Reports on Progress in Physics **50** (1987), 1657. DOI: 10.1088/0034-4885/50/12/003 (cit. on pp. 1, 22, 24, 25, 79).

[22] C. Müller, J. H. Cole, J. Lisenfeld, C. E. Professor, and S. Washburn: *Towards understanding two-level-systems in amorphous solids: insights from quantum circuits*. Rep. Prog. Phys **82** (2019), 31. DOI: 10.1088/1361-6633/ab3a7e (cit. on pp. 1, 22, 60, 79).

[23] J. M. Martinis, K. B. Cooper, R. McDermott, M. Steffen, M. Ansmann, K. D. Osborn, K. Cicak, S. Oh, D. P. Pappas, R. W. Simmonds, and C. C. Yu: *Decoherence in Josephson Qubits from Dielectric Loss*. Physical Review Letters **95** (2005), 210503. DOI: 10.1103/PhysRevLett.95.210503 (cit. on pp. 1, 24, 79).

[24] T. Capelle, E. Flurin, E. Ivanov, J. Palomo, M. Rosticher, S. Chua, T. Briant, P. F. Cohadon, A. Heidmann, T. Jacqmin, and S. Deléglise: *Probing a Two-Level System Bath via the Frequency Shift of an Off-Resonantly Driven Cavity*. Physical Review Applied **13** (2020). DOI: 10.1103/PHYSREVAPPLIED.13.034022 (cit. on p. 1).

[25] J. Lisenfeld, C. Müller, J. H. Cole, P. Bushev, A. Lukashenko, A. Shnirman, and A. V. Ustinov: *Measuring the Temperature Dependence of Individual Two-Level Systems by Direct Coherent Control*. Physical Review Letters **105** (2010), 230504. DOI: 10.1103/PhysRevLett.105.230504 (cit. on pp. 2, 75).

[26] R. Barends et al.: *Coherent Josephson Qubit Suitable for Scalable Quantum Integrated Circuits*. Physical Review Letters **111** (2013), 080502. DOI: 10.1103/PhysRevLett.111.080502 (cit. on p. 2).

[27] J. Burnett, L. Faoro, I. Wisby, V. L. Gurtovoi, A. V. Chernykh, G. M. Mikhailov, V. A. Tulin, R. Shaikhaidarov, V. Antonov, P. J. Meeson, A. Y. Tzalenchuk, and T. Lindström: *Evidence for interacting two-level systems from the 1/f noise of a superconducting resonator*. Nature Communications **5** (2014), 4119. DOI: 10.1038/ncomms5119 (cit. on pp. 2, 27, 28, 64, 76).

[28] L. Faoro and L. B. Ioffe: *Interacting tunneling model for two-level systems in amorphous materials and its predictions for their dephasing and noise in superconducting microresonators*. Physical Review B **91** (2015), 014201. DOI: https://doi.org/10.1103/PhysRevB.91.014201 (cit. on pp. 2, 27, 64, 76).

[29] J. J. Burnett, A. Bengtsson, M. Scigliuzzo, D. Niepce, M. Kudra, P. Delsing, and J. Bylander: *Decoherence benchmarking of superconducting qubits*. npj Quantum Information **5** (2019), 54. DOI: 10.1038/s41534-019-0168-5 (cit. on pp. 2, 28, 69).

[30] S. Schlör, J. Lisenfeld, C. Müller, A. Bilmes, A. Schneider, D. P. Pappas, A. V. Ustinov, and M. Weides: *Correlating Decoherence in Transmon Qubits: Low Frequency Noise by Single Fluctuators*. Physical Review Letters **123** (2019), 190502. DOI: 10.1103/PhysRevLett.123.190502 (cit. on pp. 2, 28, 69, 76).

[31] P. K. Day, H. G. LeDuc, B. A. Mazin, A. Vayonakis, and J. Zmuidzinas: *A broadband superconducting detector suitable for use in large arrays*. Nature **425** (2003), 817–821. DOI: 10.1038/nature02037 (cit. on pp. 2, 18).

[32] F. Valenti et al.: *Interplay Between Kinetic Inductance, Nonlinearity, and Quasiparticle Dynamics in Granular Aluminum Microwave Kinetic Inductance Detectors*. Physical Review Applied **11** (2019), 054087. DOI: 10.1103/PhysRevApplied.11.054087 (cit. on pp. 2, 13, 70).

[33] T. T. Hongisto and A. B. Zorin: *Single-Charge Transistor Based on the Charge-Phase Duality of a Superconducting Nanowire Circuit*. Physical Review Letters **108** (2012), 097001. DOI: 10.1103/PhysRevLett.108.097001 (cit. on p. 2).

[34] J. N. Voss, Y. Schön, M. Wildermuth, D. Dorer, J. H. Cole, H. Rotzinger, and A. V. Ustinov: *Eliminating Quantum Phase Slips in Superconducting Nanowires*. ACS Nano **15** (2021), 4108–4114. DOI: 10.1021/acsnano.0c08721 (cit. on pp. 2, 13, 40, 75).

[35] P. Winkel, I. Takmakov, D. Rieger, L. Planat, W. Hasch-Guichard, L. Grünhaupt, N. Maleeva, F. Foroughi, F. Henriques, K. Borisov, J. Ferrero, A. V. Ustinov, W. Wernsdorfer, N. Roch, and I. M. Pop: *Nondegenerate Parametric Amplifiers Based on Dispersion-Engineered Josephson-Junction Arrays*. Physical Review Applied **13** (2020), 024015. DOI: 10.1103/physrevapplied.13.024015 (cit. on pp. 2, 13).

[36] Y. Schön, J. N. Voss, M. Wildermuth, A. Schneider, S. T. Skacel, M. P. Weides, J. H. Cole, H. Rotzinger, and A. V. Ustinov: *Rabi oscillations in a superconducting nanowire circuit*. npj Quantum Materials **5** (2020), 1–5. DOI: 10.1038/s41535-020-0220-x (cit. on pp. 2, 13).

[37] D. Rieger, S. Günzler, M. Spiecker, P. Paluch, P. Winkel, L. Hahn, J. K. Hohmann, A. Bacher, W. Wernsdorfer, and I. M. Pop: *Granular aluminium nanojunction fluxonium qubit*. Nature Materials (2022), 1–6. DOI: 10.1038/s41563-022-01417-9 (cit. on pp. 2, 13).

[38] A. Gyenis, A. Di Paolo, J. Koch, A. Blais, A. A. Houck, and D. I. Schuster: *Moving beyond the Transmon: Noise-Protected Superconducting Quantum Circuits*. PRX Quantum **2** (2021), 030101. DOI: 10.1103/PRXQuantum.2.030101 (cit. on p. 2).

[39] L. Grünhaupt, M. Spiecker, D. Gusenkova, N. Maleeva, S. T. Skacel, I. Takmakov, F. Valenti, P. Winkel, H. Rotzinger, W. Wernsdorfer, A. V. Ustinov, and I. M. Pop: *Granular aluminium as a superconducting material for high-impedance quantum circuits*. Nature Materials **18** (2019), 816–819. DOI: 10.1038/s41563-019-0350-3 (cit. on pp. 2, 13).

[40] M. Devoret, S. Girvin, and R. Schoelkopf: *Circuit-QED: How strong can the coupling between a Josephson junction atom and a transmission line resonator be?**. Annalen der Physik **519** (2007), 767–779. DOI: 10.1002/andp.200751910-1109 (cit. on pp. 2, 56).

[41] K. Borisov, D. Rieger, P. Winkel, F. Henriques, F. Valenti, A. Ionita, M. Wessbecher, M. Spiecker, D. Gusenkova, I. M. Pop, and W. Wernsdorfer: *Superconducting granular aluminum resonators resilient to magnetic fields up to 1 Tesla*. Applied Physics Letters **117** (2020), 120502. DOI: 10.1063/5.0018012 (cit. on pp. 2, 13).

[42] A. J. Landig, J. V. Koski, P. Scarlino, U. C. Mendes, A. Blais, C. Reichl, W. Wegscheider, A. Wallraff, K. Ensslin, and T. Ihn: *Coherent spin–photon coupling using a resonant exchange qubit*. Nature **560** (2018), 179–184. DOI: 10.1038/s41586-018-0365-y (cit. on p. 2).

[43] C. Bonizzoni, A. Ghirri, M. Atzori, L. Sorace, R. Sessoli, and M. Affronte: *Coherent coupling between Vanadyl Phthalocyanine spin ensemble and microwave photons: towards integration of molecular spin qubits into quantum circuits*. Scientific Reports **7** (2017), 13096. DOI: 10.1038/s41598-017-13271-w (cit. on p. 2).

[44] B. Sacépé, M. Feigel'man, and T. M. Klapwijk: *Quantum breakdown of superconductivity in low-dimensional materials*. Nature Physics **16** (2020), 734–746. DOI: 10.1038/s41567-020-0905-x (cit. on p. 2).

[45] A. T. Bollinger, G. Dubuis, J. Yoon, D. Pavuna, J. Misewich, and I. Božović: *Superconductor–insulator transition in La2 - xSr x CuO4 at the pair quantum resistance*. Nature **472** (2011), 458–460. DOI: 10.1038/nature09998 (cit. on p. 2).

[46] Y. Zhou et al.: *Quantum phase transition from superconducting to insulating-like state in a pressurized cuprate superconductor*. Nature Physics **18** (2022), 406–410. DOI: 10.1038/s41567-022-01513-2 (cit. on p. 2).

[47] L. Grünhaupt, N. Maleeva, S. T. Skacel, M. Calvo, F. Levy-Bertrand, A. V. Ustinov, H. Rotzinger, A. Monfardini, G. Catelani, and I. M. Pop: *Loss Mechanisms and Quasiparticle Dynamics in Superconducting Microwave Resonators Made of Thin-Film Granular Aluminum*. Physical Review Letters **121** (2018), 117001. DOI: 10.1103/PhysRevLett.121.117001 (cit. on pp. 2, 13, 19, 57, 58, 61, 70).

[48] W. Zhang, K. Kalashnikov, W.-S. Lu, P. Kamenov, T. DiNapoli, and M. Gershenson: *Microresonators Fabricated from High-Kinetic-Inductance Aluminum Films*. Physical Review Applied **11** (2019), 011003. DOI: 10.1103/PhysRevApplied.11.011003 (cit. on pp. 2, 13, 25, 57).

[49] Q. He, P. OuYang, M. Dai, H. Guan, J. Hu, S. He, Y. Wang, and L. F. Wei: *Lumped element granular aluminum resonators with high kinetic inductances*. AIP Advances **11** (2021), 065204. DOI: 10.1063/5.0046910 (cit. on pp. 2, 13).

[50] B. Sacépé, T. Dubouchet, C. Chapelier, M. Sanquer, M. Ovadia, D. Shahar, M. Feigel'man, and L. Ioffe: *Localization of preformed Cooper pairs in disordered superconductors*. Nature Physics **7** (2011), 239–244. DOI: 10.1038/nphys1892 (cit. on p. 2).

[51] T. Dubouchet, B. Sacépé, J. Seidemann, D. Shahar, M. Sanquer, and C. Chapelier: *Collective energy gap of preformed Cooper pairs in disordered superconductors*. Nature Physics **15** (2019), 233–236. DOI: 10.1038/s41567-018-0365-8 (cit. on p. 2).

[52] F. Yang, T. Gozlinski, T. Storbeck, L. Grünhaupt, I. M. Pop, and W. Wulfhekel: *Microscopic charging and in-gap states in superconducting granular aluminum*. Physical Review B **102** (2020), 104502. DOI: 10.1103/PhysRevB.102.104502 (cit. on pp. 2, 13, 15, 70, 85).

[53] F. Levy-Bertrand et al.: *Electrodynamics of granular aluminum from superconductor to insulator: Observation of collective superconducting modes*. Physical Review B **99** (2019), 094506. DOI: 10.1103/PhysRevB.99.094506 (cit. on pp. 2, 13, 14, 16, 17, 61, 70).

[54] U. S. Pracht, M. Scheffler, M. Dressel, D. F. Kalok, C. Strunk, and T. I. Baturina: *Direct observation of the superconducting gap in a thin film of titanium nitride using terahertz spectroscopy*. Physical Review B **86** (2012), 184503. DOI: 10.1103/PhysRevB.86.184503 (cit. on p. 2).

[55] D. Sherman, B. Gorshunov, S. Poran, N. Trivedi, E. Farber, M. Dressel, and A. Frydman: *Effect of Coulomb interactions on the disorder-driven superconductor-insulator transition*. Physical Review B **89** (2014), 035149. DOI: 10.1103/PhysRevB.89.035149 (cit. on p. 2).

[56] H. Kamerlingh Onnes: *The resistance of pure mercury at helium temperatures*. Commun. Phys. Lab. Univ. Leiden **120** (1911) (cit. on p. 5).

[57] W. Meissner and H. Franz: *Messungen mit Hilfe von flüssigem Helium. IX. Supraleitfähigkeit von Carbiden and Nitriden*. Zeitschrift für Physik **65** (1930), 30–54. DOI: 10.1007/BF01397407 (cit. on p. 5).

[58] W. Meissner, H. Franz, and H. Westerhoff: *Messungen mit Hilfe von flüssigem Helium. XXII Widerstand von Metallen, Legierungen und Verbindungen*. Annalen der Physik **409** (1933), 593–619. DOI: 10.1002/andp.19334090602 (cit. on p. 5).

[59] F. H. Horn and W. T. Ziegler: *Superconductivity and Structure of Hydrides and Nitrides of Tantalum and Columbium1,2*. Journal of the American Chemical Society **69** (1947), 2762–2769. DOI: 10.1021/ja01203a056 (cit. on p. 5).

[60] G. F. Hardy and J. K. Hulm: *The Superconductivity of Some Transition Metal Compounds*. Physical Review **93** (1954), 1004. DOI: 10.1103/PhysRev.93.1004 (cit. on p. 5).

[61] P. W. Anderson: *Theory of dirty superconductors*. Journal of Physics and Chemistry of Solids **11** (1959), 26–30. DOI: 10.1016/0022-3697(59)90036-8 (cit. on p. 5).

[62] F. London and H. London: *Supraleitung und diamagnetismus*. Physica **2** (1935), 341–354. DOI: 10.1016/S0031-8914(35)90097-0 (cit. on pp. 5, 7).

[63] V. L. Ginzburg and L. D. Landau: "On the Theory of Superconductivity". *On Superconductivity and Superfluidity: A Scientific Autobiography*. Ed. by V. L. Ginzburg. Berlin, Heidelberg: Springer, 2009, pp. 113–137. DOI: 10.1007/978-3-540-68008-6_4 (cit. on pp. 5, 6).

[64] A. B. Pippard and W. L. Bragg: *An experimental and theoretical study of the relation between magnetic field and current in a superconductor*. Proceedings of the Royal Society of London. Series A. Mathematical and Physical Sciences **216** (1953), 547–568. DOI: 10.1098/rspa.1953.0040 (cit. on p. 5).

[65] J. Bardeen, L. N. Cooper, and J. R. Schrieffer: *Theory of Superconductivity*. Physical Review **108** (1957), 1175–1204. DOI: 10.1103/PhysRev.108.1175 (cit. on pp. 5, 8).

[66] D. C. Mattis and J. Bardeen: *Theory of the Anomalous Skin Effect in Normal and Superconducting Metals*. Physical Review **111** (1958), 412–417. DOI: 10.1103/PhysRev.111.412 (cit. on pp. 5, 11, 18).

[67] W. Meissner and R. Ochsenfeld: *Ein neuer Effekt bei Eintritt der Supraleitfähigkeit*. Naturwissenschaften **21** (1933), 787–788. DOI: 10.1007/BF01504252 (cit. on p. 6).

[68] L. D. Landau: *On the theory of phase transitions. I*. Phys. Z. Sowjet. **11** (1937) (cit. on p. 6).

[69] N. N. Bogoljubov: *On a new method in the theory of superconductivity*. Il Nuovo Cimento (1955-1965) **7** (1958), 794–805. DOI: 10.1007/BF02745585 (cit. on p. 8).

[70] L. Gor'kov: *Microscopic derivation of the Ginzburg-Landau equations in the theory of superconductivity*. Journal of Experimental and Theoretical Physics **36** (1959), 1364–1367 (cit. on p. 8).

[71] P. Raychaudhuri and S. Dutta: *Phase fluctuations in conventional superconductors*. Journal of Physics: Condensed Matter **34** (2021), 083001. DOI: 10.1088/1361-648X/ac360b (cit. on p. 8).

[72] C. Timm: *Theory of Super Conductivity (Lecture Notes Wintersemester 2017/2018)*. 2023. URL: https://tu-dresden.de/mn/physik/itp/cmt/ressourcen/dateien/skripte/Skript_Supra.pdf?lang=de (cit. on p. 9).

[73] G. Seibold, L. Benfatto, and C. Castellani: *Application of the Mattis-Bardeen theory in strongly disordered superconductors*. Physical Review B **96** (2017), 144507. DOI: 10.1103/PhysRevB.96.144507 (cit. on p. 9).

[74] M. Ma and P. A. Lee: *Localized superconductors*. Physical Review B **32** (1985), 5658–5667. DOI: 10.1103/PhysRevB.32.5658 (cit. on p. 9).

[75] T. Cea, D. Bucheli, G. Seibold, L. Benfatto, J. Lorenzana, and C. Castellani: *Optical excitation of phase modes in strongly disordered superconductors*. Physical Review B **89** (2014), 174506. DOI: 10.1103/PhysRevB.89.174506 (cit. on p. 10).

[76] U. S. Pracht, T. Cea, N. Bachar, G. Deutscher, E. Farber, M. Dressel, M. Scheffler, C. Castellani, A. M. García-García, and L. Benfatto: *Optical signatures of the superconducting Goldstone mode in granular aluminum: Experiments and theory*. Physical Review B **96** (2017), 094514. DOI: 10.1103/PhysRevB.96.094514 (cit. on pp. 10, 13, 70, 87).

[77] M. V. Feigel'man and L. B. Ioffe: *Microwave Properties of Superconductors Close to the Superconductor-Insulator Transition*. Physical Review Letters **120** (2018), 037004. DOI: 10.1103/PhysRevLett.120.037004 (cit. on pp. 10, 70, 87).

[78] A. V. Khvalyuk and M. V. Feigel'man. private communications (2023) (cit. on pp. 10, 70, 87).

[79] D. Sherman, U. S. Pracht, B. Gorshunov, S. Poran, J. Jesudasan, M. Chand, P. Raychaudhuri, M. Swanson, N. Trivedi, A. Auerbach, M. Scheffler, A. Frydman, and M. Dressel: *The Higgs mode in disordered superconductors close to a quantum phase transition*. Nature Physics **11** (2015), 188–192. DOI: 10.1038/nphys3227 (cit. on p. 10).

[80] T. Cea, C. Castellani, G. Seibold, and L. Benfatto: *Nonrelativistic Dynamics of the Amplitude (Higgs) Mode in Superconductors*. Physical Review Letters **115** (2015), 157002. DOI: 10.1103/PHYSREVLETT.115.157002/FIGURES/3/MEDIUM (cit. on p. 10).

[81] M. Tinkham: *Energy Gap Interpretation of Experiments on Infrared Transmission through Superconducting Films*. Physical Review **104** (1956), 845–846. DOI: 10.1103/PhysRev.104.845 (cit. on p. 10).

[82] R. E. Glover and M. Tinkham: *Conductivity of Superconducting Films for Photon Energies between 0.3 and 40kT*. Physical Review **108** (1957), 243–256. DOI: 10.1103/PhysRev.108.243 (cit. on p. 10).

[83] P. Drude: *Zur Elektronentheorie der Metalle*. Annalen der Physik **306** (1900), 566–613. DOI: 10.1002/andp.19003060312 (cit. on p. 10).

[84] M. Tinkham: *Introduction to superconductivity*. 2nd ed. Mineola, NY: Dover Publications, 2004. 454 pp. (cit. on p. 12).

[85] J. Bardeen: *Critical Fields and Currents in Superconductors*. Reviews of Modern Physics **34** (1962), 667–681. DOI: 10.1103/RevModPhys.34.667 (cit. on p. 12).

[86] P. V. Christiansen, E. B. Hansen, and C. J. Sjöström: *Negative self-inductance in superconducting thin wires and weak links*. Journal of Low Temperature Physics **4** (1971), 349–389. DOI: 10.1007/BF00628738 (cit. on p. 12).

[87] S. Anlage, H. Snortland, and M. Beasley: *A current controlled variable delay superconducting transmission line*. IEEE Transactions on Magnetics **25** (1989), 1388–1391. DOI: 10.1109/20.92554 (cit. on p. 12).

[88] B. Abeles, R. W. Cohen, and G. W. Cullen: *Enhancement of Superconductivity in Metal Films*. Physical Review Letters **17** (1966), 632–634. DOI: 10.1103/PhysRevLett.17.632 (cit. on pp. 13, 14).

[89] B. Abeles, R. W. Cohen, and W. R. Stowell: *Critical Magnetic Fields of Granular Superconductors*. Physical Review Letters **18** (1967), 902–905. DOI: 10.1103/PhysRevLett.18.902 (cit. on p. 13).

[90] R. W. Cohen and B. Abeles: *Superconductivity in Granular Aluminum Films*. Physical Review **168** (1968), 444–450. DOI: 10.1103/PhysRev.168.444 (cit. on pp. 13, 15).

[91] B. Abeles: *Effect of charging energy on superconductivity in granular metal films*. Physical Review B **15** (1977), 2828–2829. DOI: 10.1103/PhysRevB.15.2828 (cit. on pp. 13, 16).

[92] G. Deutscher, H. Fenichel, M. Gershenson, E. Grünbaum, and Z. Ovadyahu: *Transition to zero dimensionality in granular aluminum superconducting films*. Journal of Low Temperature Physics **10** (1973), 231–243. DOI: 10.1007/BF00655256 (cit. on pp. 13, 15).

[93] G. Deutscher, M. Gershenson, E. Grünbaum, and Y. Imry: *Granular Superconducting Films*. Journal of Vacuum Science and Technology **10** (1973), 697–701. DOI: 10.1116/1.1318416 (cit. on pp. 13, 15).

[94] G. Deutscher and R. Rosenbaum: *Granular aluminum SQUID's*. Applied Physics Letters **27** (1975), 366–368. DOI: 10.1063/1.88479 (cit. on p. 13).

[95] D. Abraham, G. Deutscher, R. Rosenbaum, and S. Wolf: *Magnetic Penetration Depth in Granular Al-Al2O3 films*. Journal de Physique Colloques **39** (1978). DOI: 10.1051/jphyscol:19786264Ãŕ (cit. on p. 13).

[96] B. Bandyopadhyay, P. Lindenfeld, W. L. McLean, and H. K. Sin: *Hall effect in granular aluminum*. Physical Review B **26** (1982), 3476. DOI: 10.1103/PhysRevB.26.3476 (cit. on pp. 13, 17, 43).

[97] R. C. Dynes, J. P. Garno, G. B. Hertel, and T. P. Orlando: *Tunneling Study of Superconductivity near the Metal-Insulator Transition*. Physical Review Letters **53** (1984), 2437–2440. DOI: 10.1103/PhysRevLett.53.2437 (cit. on p. 13).

[98] N. Bachar, S. Lerer, A. Levy, S. Hacohen-Gourgy, B. Almog, H. Saadaoui, Z. Salman, E. Morenzoni, and G. Deutscher: *Mott transition in granular aluminum*. Physical Review B **91** (2015), 041123. DOI: 10.1103/PHYSREVB.91.041123/FIGURES/3/MEDIUM (cit. on pp. 13, 17, 43, 85).

[99] U. S. Pracht, N. Bachar, L. Benfatto, G. Deutscher, E. Farber, M. Dressel, and M. Scheffler: *Enhanced Cooper pairing versus suppressed phase coherence shaping the superconducting dome in coupled aluminum nanograins*. Physical Review B **93** (2016), 100503. DOI: 10.1103/PhysRevB.93.100503 (cit. on pp. 13, 17, 61, 86).

[100] M. Wildermuth, L. Powalla, J. N. Voss, Y. Schön, A. Schneider, M. V. Fistul, H. Rotzinger, and A. V. Ustinov: *Fluxons in high-impedance long Josephson junctions*. Applied Physics Letters **120** (2022), 112601. DOI: 10.1063/5.0082197 (cit. on pp. 13, 40).

[101] L. Grünhaupt: *Granular aluminium superinductors*. PhD thesis. Karlsruhe Institute of Technology, 2019. DOI: 10.5445/KSP/1000097320 (cit. on p. 13).

[102] B. Josephson: *Possible new effects in superconductive tunnelling*. Physics Letters **1** (1962), 251–253. DOI: 10.1016/0031-9163(62)91369-0 (cit. on p. 13).

[103] V. L. Ginzburg: *On surface superconductivity*. Physics Letters **13** (1964), 101–102. DOI: 10.1016/0031-9163(64)90672-9 (cit. on p. 14).

[104] M. H. Cohen and D. H. Douglass: *Superconductive Pairing Across Electron Barriers*. Physical Review Letters **19** (1967), 118–121. DOI: 10.1103/PhysRevLett.19.118 (cit. on pp. 14, 15).

[105] R. H. Parmenter: *Size Effect in a Granular Superconductor*. Physical Review **166** (1968), 392–396. DOI: 10.1103/PhysRev.166.392 (cit. on p. 15).

[106] V. Z. Kresin and Y. N. Ovchinnikov: *Shell structure and strengthening of superconducting pair correlation in nanoclusters*. Physical Review B **74** (2006), 024514. DOI: 10.1103/PhysRevB.74.024514 (cit. on p. 15).

[107] A. M. García-García, J. D. Urbina, E. A. Yuzbashyan, K. Richter, and B. L. Altshuler: *BCS superconductivity in metallic nanograins: Finite-size corrections, low-energy excitations, and robustness of shell effects*. Physical Review B **83** (2011), 014510. DOI: 10.1103/PhysRevB.83.014510 (cit. on p. 15).

[108] Z. Lindenfeld, E. Eisenberg, and R. Lifshitz: *Possibility of electron pairing in small metallic nanoparticles*. Physical Review B **84** (2011), 064532. DOI: 10.1103/PhysRevB.84.064532 (cit. on p. 15).

[109] J. Mayoh and A. M. García-García: *Strong enhancement of bulk superconductivity by engineered nanogranularity*. Physical Review B **90** (2014), 134513. DOI: 10.1103/PhysRevB.90.134513 (cit. on p. 15).

[110] I. S. Beloborodov, A. V. Lopatin, V. M. Vinokur, and K. B. Efetov: *Granular electronic systems*. Reviews of Modern Physics **79** (2007), 469. DOI: 10.1103/RevModPhys.79.469 (cit. on p. 16).

[111] P. W. Anderson: *Lectures on The Many-Body Problems*. Vol. 2. New York: Academic Press, 1964 (cit. on p. 16).

[112] V. Ambegaokar and A. Baratoff: *Tunneling Between Superconductors*. Physical Review Letters **10** (1963), 486–489. DOI: 10.1103/PhysRevLett.10.486 (cit. on p. 16).

[113] B. Abeles, P. Sheng, M. Coutts, and Y. Arie: *Structural and electrical properties of granular metal films*. Advances in Physics **24** (1975), 407–461. DOI: 10.1080/00018737500101431 (cit. on p. 16).

[114] K. B. Efetov: *Phase transition in granulated superconductors*. Soviet Physics - JETP **51** (1980). URL: https://www.osti.gov/biblio/7061039 (cit. on pp. 16, 17, 70, 86).

[115] Y. Shapira and G. Deutscher: *Semiconductor-superconductor transition in granular Al-Ge*. Physical Review B **27** (1983), 4463–4466. DOI: 10.1103/PhysRevB.27.4463 (cit. on p. 16).

[116] B. G. Orr, H. M. Jaeger, A. M. Goldman, and C. G. Kuper: *Global phase coherence in two-dimensional granular superconductors*. Physical Review Letters **56** (1986), 378–381. DOI: 10.1103/PhysRevLett.56.378 (cit. on p. 16).

[117] H. M. Jaeger, D. B. Haviland, A. M. Goldman, and B. G. Orr: *Threshold for superconductivity in ultrathin amorphous gallium films*. Physical Review B **34** (1986), 4920–4923. DOI: 10.1103/PhysRevB.34.4920 (cit. on p. 16).

[118] S. Chakravarty, S. Kivelson, G. T. Zimanyi, and B. I. Halperin: *Effect of quasiparticle tunneling on quantum-phase fluctuations and the onset of superconductivity in granular films*. Physical Review B **35** (1987), 7256–7259. DOI: 10.1103/PhysRevB.35.7256 (cit. on pp. 16, 87).

[119] V. Ambegaokar, U. Eckern, and G. Schön: *Quantum Dynamics of Tunneling between Superconductors*. Physical Review Letters **48** (1982), 1745–1748. DOI: 10.1103/PhysRevLett.48.1745 (cit. on p. 16).

[120] H. M. Jaeger, D. B. Haviland, B. G. Orr, and A. M. Goldman: *Onset of superconductivity in ultrathin granular metal films*. Physical Review B **40** (1989), 182–196. DOI: 10.1103/PhysRevB.40.182 (cit. on p. 17).

[121] M. Watanabe, H. Shimada, S.-i. Kobayashi, and Y. Ootuka: *Superconductor-Insulator Transition in Granular Films of Tin*. Journal of the Physical Society of Japan **66** (1997), 1419–1426. DOI: 10.1143/JPSJ.66.1419 (cit. on p. 17).

[122] I. S. Beloborodov, K. B. Efetov, A. V. Lopatin, and V. M. Vinokur: *Effects of fluctuations and Coulomb interaction on the transition temperature of granular superconductors*. Physical Review B **71** (2005), 184501. DOI: 10.1103/PhysRevB.71.184501 (cit. on p. 17).

[123] V. J. Emery and S. A. Kivelson: *Importance of phase fluctuations in superconductors with small superfluid density*. Nature **374** (1995), 434–437. DOI: 10.1038/374434a0 (cit. on p. 17).

[124] G. Deutscher: *New Superconductors: From Granular To High Tc*. Singapore: World Scientific Publishing Co. Pte. Ltd., 2006. 350 pp. (cit. on p. 17).

[125] M. Boissonneault, J. M. Gambetta, and A. Blais: *Dispersive regime of circuit QED: Photon-dependent qubit dephasing and relaxation rates*. Physical Review A **79** (2009), 013819. DOI: 10.1103/PhysRevA.79.013819 (cit. on p. 18).

[126] J.-J. Chang and D. J. Scalapino: *Kinetic-equation approach to nonequilibrium superconductivity*. Physical Review B **15** (1977), 2651–2670. DOI: 10.1103/PhysRevB.15.2651 (cit. on p. 19).

[127] S. Rajauria, L. M. A. Pascal, P. Gandit, F. W. J. Hekking, B. Pannetier, and H. Courtois: *Efficiency of quasiparticle evacuation in superconducting devices*. Physical Review B **85** (2012), 020505. DOI: 10.1103/PhysRevB.85.020505 (cit. on p. 19).

[128] P. J. de Visser, J. J. A. Baselmans, S. J. C. Yates, P. Diener, A. Endo, and T. M. Klapwijk: *Microwave-induced excess quasiparticles in superconducting resonators measured through correlated conductivity fluctuations*. Applied Physics Letters **100** (2012), 162601. DOI: 10.1063/1.4704151 (cit. on pp. 19, 52, 65, 70).

[129] A. P. Vepsäläinen, A. H. Karamlou, J. L. Orrell, A. S. Dogra, B. Loer, F. Vasconcelos, D. K. Kim, A. J. Melville, B. M. Niedzielski, J. L. Yoder, S. Gustavsson, J. A. Formaggio, B. A. VanDevender, and W. D. Oliver: *Impact of ionizing radiation on superconducting qubit coherence*. Nature **584** (2020), 551–556. DOI: 10.1038/s41586-020-2619-8 (cit. on p. 19).

[130] J. Gao: *The Physics of Superconducting Microwave Resonators*. PhD thesis. California Institute of Technology, 2008. DOI: 10.7907/RAT0-VM75 (cit. on pp. 20, 21, 60).

[131] J. P. Turneaure, J. Halbritter, and H. A. Schwettman: *The Surface Impedance of Superconductors and Normal Conductors: The Mattis-Bardeen Theory*. Journal of Superconductivity **4** (1991) (cit. on p. 21).

[132] R. C. Zeller and R. O. Pohl: *Thermal Conductivity and Specific Heat of Noncrystalline Solids*. Physical Review B **4** (1971), 2029–2041. DOI: 10.1103/PhysRevB.4.2029 (cit. on pp. 22, 27).

[133] R. B. Stephens: *Low-Temperature Specific Heat and Thermal Conductivity of Noncrystalline Dielectric Solids*. Physical Review B **8** (1973), 2896–2905. DOI: 10.1103/PhysRevB.8.2896 (cit. on p. 22).

[134] P. w. Anderson, B. I. Halperin, and c. M. Varma: *Anomalous low-temperature thermal properties of glasses and spin glasses*. The Philosophical Magazine: A Journal of Theoretical Experimental and Applied Physics **25** (1972), 1–9. DOI: 10.1080/14786437208229210 (cit. on p. 22).

[135] J. Lisenfeld, G. J. Grabovskij, C. Müller, J. H. Cole, G. Weiss, and A. V. Ustinov: *Observation of directly interacting coherent two-level systems in an amorphous material*. Nature Communications **6** (2015), 6182. DOI: 10.1038/ncomms7182 (cit. on pp. 24, 27, 75).

[136] H. M. Carruzzo, A. Bilmes, J. Lisenfeld, Z. Yu, B. Wang, Z. Wan, J. R. Schmidt, and C. C. Yu: *Distribution of two-level system couplings to strain and electric fields in glasses at low temperatures*. Physical Review B **104** (2021), 134203. DOI: 10.1103/PhysRevB.104.134203 (cit. on p. 24).

[137] R. W. Simmonds, M. S. Allman, F. Altomare, K. Cicak, K. D. Osborn, J. A. Park, M. Sillanpää, A. Sirois, J. A. Strong, and J. D. Whittaker: *Coherent interactions between phase qubits, cavities, and TLS defects*. Quantum Information Processing **8** (2009), 117–131. DOI: 10.1007/s11128-009-0095-z (cit. on p. 24).

[138] I. I. Rabi: *Space Quantization in a Gyrating Magnetic Field*. Physical Review **51** (1937), 652–654. DOI: 10.1103/PhysRev.51.652 (cit. on p. 24).

[139] H. Wang, M. Hofheinz, J. Wenner, M. Ansmann, R. C. Bialczak, M. Lenander, E. Lucero, M. Neeley, A. D. O'Connell, D. Sank, M. Weides, A. N. Cleland, and J. M. Martinis: *Improving the coherence time of superconducting coplanar resonators*. Applied Physics Letters **95** (2009), 233508. DOI: 10.1063/1.3273372 (cit. on p. 25).

[140] J. M. Sage, V. Bolkhovsky, W. D. Oliver, B. Turek, and P. B. Welander: *Study of loss in superconducting coplanar waveguide resonators*. Journal of Applied Physics **109** (2011), 063915. DOI: 10.1063/1.3552890 (cit. on p. 25).

[141] D. P. Pappas, M. R. Vissers, D. S. Wisbey, J. S. Kline, and J. Gao: *Two Level System Loss in Superconducting Microwave Resonators*. IEEE Transactions on Applied Superconductivity **21** (2011), 871–874. DOI: 10.1109/TASC.2010.2097578 (cit. on p. 25).

[142] J. Goetz, F. Deppe, M. Haeberlein, F. Wulschner, C. W. Zollitsch, S. Meier, M. Fischer, P. Eder, E. Xie, K. G. Fedorov, E. P. Menzel, A. Marx, and R. Gross: *Loss mechanisms in superconducting thin film microwave resonators*. Journal of Applied Physics **119** (2016), 015304. DOI: 10.1063/1.4939299 (cit. on p. 25).

[143] J. D. Brehm, A. Bilmes, G. Weiss, A. V. Ustinov, and J. Lisenfeld: *Transmission-line resonators for the study of individual two-level tunneling systems*. Applied Physics Letters **111** (2017), 112601. DOI: 10.1063/1.5001920 (cit. on pp. 25, 26, 79, 90).

[144] S. Hunklinger and W. Arnold: "Ultrasonic Properties of Glasses at Low Temperatures". *Physical Acoustics*. Ed. by W. P. Mason and R. N. Thurston. Vol. 12. Academic Press, 1976, pp. 155–215. DOI: 10.1016/B978-0-12-477912-9.50008-4 (cit. on p. 25).

[145] J. Gao, M. Daal, A. Vayonakis, S. Kumar, J. Zmuidzinas, B. Sadoulet, B. A. Mazin, P. K. Day, and H. G. Leduc: *Experimental evidence for a surface distribution of two-level systems in superconducting lithographed microwave resonators*. Applied Physics Letters **92** (2008), 152505. DOI: 10.1063/1.2906373 (cit. on p. 25).

[146] B. Sarabi: *Cavity Quantum Electrodynamics of Nanoscale Two-Level Systems*. PhD thesis. University of Maryland, 2014. URL: https://drum.lib.umd.edu/handle/1903/16186 (cit. on pp. 25, 32, 33, 77, 79).

[147] B. Sarabi, A. N. Ramanayaka, A. L. Burin, F. C. Wellstood, and K. D. Osborn: *Cavity quantum electrodynamics using a near-resonance two-level system: Emergence of the Glauber state*. Applied Physics Letters **106** (2015), 172601. DOI: 10.1063/1.4918775 (cit. on pp. 26, 79).

[148] B. Sarabi, A. N. Ramanayaka, A. L. Burin, F. C. Wellstood, and K. D. Osborn: *Projected Dipole Moments of Individual Two-Level Defects Extracted Using Circuit Quantum Electrodynamics*. Physical Review Letters **116** (2016), 167002. DOI: 10.1103/PhysRevLett.116.167002 (cit. on pp. 26, 79, 90).

[149] J. Burnett, L. Faoro, and T. Lindström: *Analysis of high quality superconducting resonators: consequences for TLS properties in amorphous oxides*. Superconductor Science and Technology **29** (2016), 044008. DOI: 10.1088/0953-2048/29/4/044008 (cit. on pp. 27, 28, 86).

[150] T. Lindström, J. E. Healey, M. S. Colclough, C. M. Muirhead, and A. Y. Tzalenchuk: *Properties of superconducting planar resonators at millikelvin temperatures*. Physical Review B **80** (2009), 132501. DOI: 10.1103/PhysRevB.80.132501 (cit. on p. 27).

[151] P. Macha, S. H. W. van der Ploeg, G. Oelsner, E. Il'ichev, H.-G. Meyer, S. Wünsch, and M. Siegel: *Losses in coplanar waveguide resonators at millikelvin temperatures*. Applied Physics Letters **96** (2010), 062503. DOI: 10.1063/1.3309754 (cit. on p. 27).

[152] L. Faoro and L. B. Ioffe: *Internal Loss of Superconducting Resonators Induced by Interacting Two-Level Systems*. Physical Review Letters **109** (2012), 157005. DOI: 10.1103/PhysRevLett.109.157005 (cit. on p. 27).

[153] J. Gao, J. Zmuidzinas, B. A. Mazin, H. G. LeDuc, and P. K. Day: *Noise properties of superconducting coplanar waveguide microwave resonators*. Applied Physics Letters **90** (2007), 102507. DOI: 10.1063/1.2711770 (cit. on p. 27).

[154] R. Barends, H. L. Hortensius, T. Zijlstra, J. J. A. Baselmans, S. J. C. Yates, J. R. Gao, and T. M. Klapwijk: *Contribution of dielectrics to frequency and noise of NbTiN superconducting resonators*. Applied Physics Letters **92** (2008), 223502. DOI: 10.1063/1.2937837 (cit. on p. 27).

[155] S. Kumar, J. Gao, J. Zmuidzinas, B. A. Mazin, H. G. LeDuc, and P. K. Day: *Temperature dependence of the frequency and noise of superconducting coplanar waveguide resonators*. Applied Physics Letters **92** (2008), 123503. DOI: 10.1063/1.2894584 (cit. on p. 27).

[156] A. P. van der Wel, E. A. M. Klumperink, J. S. Kolhatkar, E. Hoekstra, M. F. Snoeij, C. Salm, H. Wallinga, and B. Nauta: *Low-Frequency Noise Phenomena in Switched MOSFETs*. IEEE Journal of Solid-State Circuits **42** (2007), 540–550. DOI: 10.1109/JSSC.2006.891714 (cit. on p. 27).

[157] E. Geva and J. L. Skinner: *Theory of Single-Molecule Optical Line-Shape Distributions in Low-Temperature Glasses*. The Journal of Physical Chemistry B **101** (1997), 8920–8932. DOI: 10.1021/jp971722o (cit. on p. 27).

[158] A. N. Ramanayaka, B. Sarabi, and K. D. Osborn: *Evidence for universal relationship between the measured 1/f permittivity noise and loss tangent created by tunneling atoms*. 2015. arXiv: 1507.06043[cond-mat]. DOI: 10.48550/arXiv.1507.06043 (cit. on p. 28).

[159] J. M. Gambetta, J. M. Chow, and M. Steffen: *Building logical qubits in a superconducting quantum computing system*. npj Quantum Information **3** (2017), 1–7. DOI: 10.1038/s41534-016-0004-0 (cit. on p. 29).

[160] X. Gu, A. F. Kockum, A. Miranowicz, Y.-x. Liu, and F. Nori: *Microwave photonics with superconducting quantum circuits*. Physics Reports. Microwave photonics with superconducting quantum circuits **718-719** (2017), 1–102. DOI: 10.1016/j.physrep.2017.10.002 (cit. on p. 29).

[161] D. M. Pozar: *Microwave engineering*. 4th ed. Hoboken, NJ: John Wiley & Sons, 2012. 732 pp. (cit. on pp. 29, 30).

[162] J. Braumüller: *Quantum simulation experiments with superconducting circuits*. PhD thesis. Karlsruhe Institute of Technology, 2018. DOI: 10.5445/KSP/1000081315 (cit. on pp. 30, 31).

[163] C. Deng, M. Otto, and A. Lupascu: *An analysis method for transmission measurements of superconducting resonators with applications to quantum-regime dielectric-loss measurements*. Journal of Applied Physics **114** (2013), 054504. DOI: 10.1063/1.4817512 (cit. on p. 32).

[164] C. W. Gardiner and M. J. Collett: *Input and output in damped quantum systems: Quantum stochastic differential equations and the master equation*. Physical Review A **31** (1985), 3761–3774. DOI: 10.1103/PhysRevA.31.3761 (cit. on p. 32).

[165] M. S. Khalil, M. J. A. Stoutimore, F. C. Wellstood, and K. D. Osborn: *An analysis method for asymmetric resonator transmission applied to superconducting devices*. Journal of Applied Physics **111** (2012), 054510. DOI: 10.1063/1.3692073 (cit. on p. 33).

[166] S. Probst, F. B. Song, P. A. Bushev, A. V. Ustinov, and M. Weides: *Efficient and robust analysis of complex scattering data under noise in microwave resonators*. Review of Scientific Instruments **86** (2015), 024706. DOI: 10.1063/1.4907935 (cit. on pp. 35, 57).

[167] G. Duffing: *Erzwungene Schwingungen bei veränderlicher Eigenfrequenz und ihre technische Bedeutung*. Sammlung Vieweg 41/42. Braunschweig: F. Vieweg & Sohn, 1918. 134 pp. (cit. on p. 35).

[168] L. J. Swenson, P. K. Day, B. H. Eom, H. G. Leduc, N. Llombart, C. M. McKenney, O. Noroozian, and J. Zmuidzinas: *Operation of a titanium nitride superconducting microresonator detector in the nonlinear regime*. Journal of Applied Physics **113** (2013), 104501. DOI: 10.1063/1.4794808 (cit. on p. 35).

[169] J. S. Chapin: "Sputtering process and apparatus". U.S. pat. A. Inc. 1979. URL: https://patents.google.com/patent/US4166018A/en (cit. on p. 38).

[170] A. F. Mayadas, M. Shatzkes, and J. F. Janak: *Electrical resistivity model for polycrystalline films: the case of specular reflection at external surfaces*. Applied Physics Letters **14** (1969), 345–347. DOI: 10.1063/1.1652680 (cit. on p. 40).

[171] K. Yoshida, K. Watanabe, T. Kisu, and K. Enpuku: *Evaluation of magnetic penetration depth and surface resistance of superconducting thin films using coplanar waveguides*. IEEE Transactions on Applied Superconductivity **5** (1995), 1979–1982. DOI: 10.1109/77.402973 (cit. on p. 42).

[172] A. F. Ioffe and A. R. Regel: *Non-crystalline, amorphous and liquid electronic semiconductors*. Prog. Semicond **4** (1960), 237–291 (cit. on p. 43).

[173] G. Deutscher: *Granular Superconductivity: a Playground for Josephson, Anderson, Kondo, and Mott*. Journal of Superconductivity and Novel Magnetism **34** (2021), 1699–1703. DOI: 10.1007/S10948-020-05773-Y/FIGURES/1 (cit. on p. 43).

[174] C. Enss and S. Hunklinger: *Low-Temperature Physics*. Berlin Heidelberg: Springer-Verlag, 2005 (cit. on p. 44).

[175] C. Macklin, K. O'Brien, D. Hover, M. E. Schwartz, V. Bolkhovsky, X. Zhang, W. D. Oliver, and I. Siddiqi: *A near–quantum-limited Josephson traveling-wave parametric amplifier*. Science **350** (2015), 307–310. DOI: 10.1126/science.aaa8525 (cit. on p. 46).

[176] G. J. Grabovskij, T. Peichl, J. Lisenfeld, G. Weiss, and A. V. Ustinov: *Strain tuning of individual atomic tunneling systems detected by a superconducting qubit.* Science (New York, N.Y.) **338** (2012), 232–4. DOI: 10.1126/science.1226487 (cit. on p. 46).

[177] A. Bilmes: *Resolving locations of defects in superconducting transmon qubits*. PhD thesis. Karlsruhe Institute of Technology, 2019. DOI: 10.5445/KSP/1000097557 (cit. on pp. 47, 54).

[178] J. Lisenfeld, A. Bilmes, A. Megrant, R. Barends, J. Kelly, P. Klimov, G. Weiss, J. M. Martinis, and A. V. Ustinov: *Electric field spectroscopy of material defects in transmon qubits*. npj Quantum Information **5** (2019), 1–6. DOI: 10.1038/s41534-019-0224-1 (cit. on pp. 47, 58, 79).

[179] T. Lindström, J. Burnett, M. Oxborrow, and A. Y. Tzalenchuk: *Pound-locking for characterization of superconducting microresonators*. Review of Scientific Instruments **82** (2011), 104706. DOI: 10.1063/1.3648134 (cit. on p. 47).

[180] M. S. Bartlett: *Smoothing Periodograms from Time-Series with Continuous Spectra*. Nature **161** (1948), 686–687. DOI: 10.1038/161686a0 (cit. on p. 50).

[181] P. Welch: *The use of fast Fourier transform for the estimation of power spectra: A method based on time averaging over short, modified periodograms*. IEEE Transactions on Audio and Electroacoustics **15** (1967), 70–73. DOI: 10.1109/TAU.1967.1161901 (cit. on p. 50).

[182] R. B. Blackman and J. W. Tukey: *The Measurement of Power Spectra from the Point of View of Communications Engineering — Part I*. Bell System Technical Journal **37** (1958), 185–282. DOI: 10.1002/j.1538-7305.1958.tb03874.x (cit. on p. 50).

[183] J. R. Pierce: *Physical Sources of Noise*. Proceedings of the IRE **44** (1956), 601–608. DOI: 10.1109/JRPROC.1956.275123 (cit. on p. 52).

[184] F. Grüneis: *The transition from generation–recombination noise in bulk semiconductors to discrete switching in small-area semiconductors*. Physica A: Statistical Mechanics and its Applications **568** (2021), 125748. DOI: 10.1016/j.physa.2021.125748 (cit. on p. 52).

[185] D. Allan: *Statistics of atomic frequency standards*. Proceedings of the IEEE **54** (1966), 221–230. DOI: 10.1109/PROC.1966.4634 (cit. on p. 52).

[186] J. Snyder: *An Ultra-High Resolution Frequency Meter. Thirty Fifth Annual Frequency Control Symposium*. Thirty Fifth Annual Frequency Control Symposium. 1981, pp. 464–469. DOI: 10.1109/FREQ.1981.200513 (cit. on p. 53).

[187] D. Howe, D. Allan, and J. Barnes: *Properties of Signal Sources and Measurement Methods*. *Thirty Fifth Annual Frequency Control Symposium*. Thirty Fifth Annual Frequency Control Symposium. 1981, pp. 669–716. DOI: 10.1109/FREQ.1981.200541 (cit. on p. 53).

[188] J. A. Barnes, A. R. Chi, L. S. Cutler, D. J. Healey, D. B. Leeson, T. E. McGunigal, J. A. Mullen, W. L. Smith, R. L. Sydnor, R. F. C. Vessot, and G. M. R. Winkler: *Characterization of Frequency Stability*. IEEE Transactions on Instrumentation and Measurement **IM-20** (1971), 105–120. DOI: 10.1109/TIM.1971.5570702 (cit. on p. 53).

[189] B. M. Lansdorp and O. A. Saleh: *Power spectrum and Allan variance methods for calibrating single-molecule video-tracking instruments*. The Review of Scientific Instruments **83** (2012), 025115. DOI: 10.1063/1.3687431 (cit. on p. 53).

[190] M. Kristen, J. N. Voss, M. Wildermuth, H. Rotzinger, and A. V. Ustinov: *Random telegraph fluctuations in granular microwave resonators*. Applied Physics Letters **122** (2023), 202602. DOI: 10.1063/5.0147430 (cit. on pp. 57, 61, 63, 64, 66, 67, 69).

[191] S. E. de Graaf, L. Faoro, J. Burnett, A. A. Adamyan, A. Y. Tzalenchuk, S. E. Kubatkin, T. Lindström, and A. V. Danilov: *Suppression of low-frequency charge noise in superconducting resonators by surface spin desorption*. Nature Communications **9** (2018), 1143. DOI: 10.1038/s41467-018-03577-2 (cit. on p. 58).

[192] S. N. Artemenko and A. F. Volkov: *Electric fields and collective oscillations in superconductors*. Soviet Physics Uspekhi **22** (1979), 295. DOI: 10.1070/PU1979v022n05ABEH005495 (cit. on p. 58).

[193] W. Schottky: *Über spontane Stromschwankungen in verschiedenen Elektrizitätsleitern*. Annalen der Physik **362** (1918), 541–567. DOI: 10.1002/andp.19183622304 (cit. on p. 62).

[194] Y. M. Blanter and M. Büttiker: *Shot noise in mesoscopic conductors*. Physics Reports **336** (2000), 1–166. DOI: 10.1016/S0370-1573(99)00123-4 (cit. on p. 62).

[195] J. Burnett, A. Bengtsson, D. Niepce, and J. Bylander: *Noise and loss of superconducting aluminium resonators at single photon energies*. Journal of Physics: Conference Series **969** (2018), 012131. DOI: 10.1088/1742-6596/969/1/012131 (cit. on p. 64).

[196] S. E. de Graaf, A. Y. Tzalenchuk, and T. Lindström: *1/f frequency noise of superconducting resonators in large magnetic fields*. Applied Physics Letters **113** (2018), 142601. DOI: 10.1063/1.5053660 (cit. on p. 64).

[197] C. M. Van Vliet and P. H. Handel: *A new transform theorem for stochastic processes with special application to counting statistics*. Physica A: Statistical Mechanics and its Applications **113** (1982), 261–276. DOI: 10.1016/0378-4371(82)90019-X (cit. on p. 67).

[198] D. Niepce, J. J. Burnett, M. Kudra, J. H. Cole, and J. Bylander: *Stability of superconducting resonators: Motional narrowing and the role of Landau-Zener driving of two-level defects*. Science Advances **7** (2021), 462–486. DOI: DOI: 10.1126/sciadv.abh0462 (cit. on pp. 67, 69).

[199] P. J. de Visser, J. J. A. Baselmans, P. Diener, S. J. C. Yates, A. Endo, and T. M. Klapwijk: *Number Fluctuations of Sparse Quasiparticles in a Superconductor*. Physical Review Letters **106** (2011), 167004. DOI: 10.1103/PhysRevLett.106.167004 (cit. on p. 70).

[200] J. Baselmans, S. J. C. Yates, R. Barends, Y. J. Y. Lankwarden, J. R. Gao, H. Hoevers, and T. M. Klapwijk: *Noise and Sensitivity of Aluminum Kinetic Inductance Detectors for Sub-mm Astronomy*. Journal of Low Temperature Physics **151** (2008), 524–529. DOI: 10.1007/s10909-007-9684-3 (cit. on p. 70).

[201] S. E. de Graaf, L. Faoro, L. B. Ioffe, S. Mahashabde, J. J. Burnett, T. Lindström, S. E. Kubatkin, A. V. Danilov, and A. Y. Tzalenchuk: *Two-level systems in superconducting quantum devices due to trapped quasiparticles*. Science Advances **6** (2020), eabc5055. DOI: 10.1126/sciadv.abc5055 (cit. on pp. 70, 86, 90, 126).

[202] A. Roy, Y. Wu, R. Berkovits, and A. Frydman: *Universal Voltage Fluctuations in Disordered Superconductors*. Physical Review Letters **125** (2020), 147002. DOI: 10.1103/PhysRevLett.125.147002 (cit. on p. 70).

[203] C. Barone, H. Rotzinger, C. Mauro, D. Dorer, J. Münzberg, A. V. Ustinov, and S. Pagano: *Kondo-like transport and magnetic field effect of charge carrier fluctuations in granular aluminum oxide thin films*. Scientific Reports **8** (2018), 13892. DOI: 10.1038/s41598-018-32298-1 (cit. on p. 70).

[204] C. Barone, H. Rotzinger, J. N. Voss, C. Mauro, Y. Schön, A. V. Ustinov, and S. Pagano: *Current-Resistance Effects Inducing Nonlinear Fluctuation Mechanisms in Granular Aluminum Oxide Nanowires*. Nanomaterials **10** (2020), 524. DOI: 10.3390/nano10030524 (cit. on p. 70).

[205] A. V. Khvalyuk and M. V. Feigel'man: *Distribution of the order parameter in strongly disordered superconductors: An analytic theory*. Physical Review B **104** (2021), 224505. DOI: 10.1103/PhysRevB.104.224505 (cit. on p. 70).

[206] C. Müller, J. Lisenfeld, A. Shnirman, and S. Poletto: *Interacting two-level defects as sources of fluctuating high-frequency noise in superconducting circuits*. Physical Review B **92** (2015), 035442. DOI: 10.1103/PhysRevB.92.035442 (cit. on p. 76).

[207] Y. Shalibo, Y. Rofe, D. Shwa, F. Zeides, M. Neeley, J. M. Martinis, and N. Katz: *Lifetime and Coherence of Two-Level Defects in a Josephson Junction*. Physical Review Letters **105** (2010), 177001. DOI: 10.1103/PhysRevLett.105.177001 (cit. on p. 79).

[208] M. Von Schickfus and S. Hunklinger: *Saturation of the dielectric absorption of vitreous silica at low temperatures*. Physics Letters A **64** (1977), 144–146. DOI: 10.1016/0375-9601(77)90558-8 (cit. on p. 79).

[209] B. Golding, M. v. Schickfus, S. Hunklinger, and K. Dransfeld: *Intrinsic Electric Dipole Moment of Tunneling Systems in Silica Glasses*. Physical Review Letters **43** (1979), 1817–1821. DOI: 10.1103/PhysRevLett.43.1817 (cit. on p. 79).

[210] G. Baier and M. v. Schickfus: *Dielectric rotary echoes in vitreous silica*. Physical Review B **38** (1988), 9952–9957. DOI: 10.1103/PhysRevB.38.9952 (cit. on p. 79).

[211] J. Lisenfeld, A. Bilmes, S. Matityahu, S. Zanker, M. Marthaler, M. Schechter, G. Schön, A. Shnirman, G. Weiss, and A. V. Ustinov: *Decoherence spectroscopy with individual two-level tunneling defects*. Scientific Reports **6** (2016), 23786. DOI: 10.1038/srep23786 (cit. on p. 79).

[212] S. M. Meißner, A. Seiler, J. Lisenfeld, A. V. Ustinov, and G. Weiss: *Probing individual tunneling fluctuators with coherently controlled tunneling systems*. Physical Review B **97** (2018), 180505. DOI: 10.1103/PhysRevB.97.180505 (cit. on p. 84).

[213] L. Yu, S. Matityahu, Y. J. Rosen, C.-C. Hung, A. Maksymov, A. L. Burin, M. Schechter, and K. D. Osborn: *Experimentally revealing anomalously large dipoles in the dielectric of a quantum circuit*. Scientific Reports **12** (2022), 16960. DOI: 10.1038/s41598-022-21256-7 (cit. on p. 85).

[214] L. D. Alegria, D. M. Tennant, K. R. Chaves, J. R. I. Lee, S. R. O'Kelley, Y. J. Rosen, and J. L. DuBois: *Two-Level Systems in Nucleated and Non-Nucleated Epitaxial alpha-Tantalum films*. 2023. arXiv: 2301.10306[cond-mat]. DOI: 10.48550/arXiv.2301.10306 (cit. on p. 85).

[215] A. L. Burin, M. S. Khalil, and K. D. Osborn: *Universal Dielectric Loss in Glass from Simultaneous Bias and Microwave Fields*. Physical Review Letters **110** (2013), 157002. DOI: 10.1103/PhysRevLett.110.157002 (cit. on p. 85).

[216] M. Schechter and P. C. E. Stamp: *Inversion symmetric two-level systems and the low-temperature universality in disordered solids*. Physical Review B **88** (2013), 174202. DOI: 10.1103/PhysRevB.88.174202 (cit. on pp. 85, 87).

[217] A. L. Efros and B. I. Shklovskii: *Coulomb gap and low temperature conductivity of disordered systems*. Journal of Physics C: Solid State Physics **8** (1975), L49. DOI: 10.1088/0022-3719/8/4/003 (cit. on p. 85).

[218] A. Churkin, D. Barash, and M. Schechter: *Nonhomogeneity of the density of states of tunneling two-level systems at low energies*. Physical Review B **89** (2014), 104202. DOI: 10.1103/PhysRevB.89.104202 (cit. on p. 85).

[219] M. Sidorova, A. Semenov, H.-W. Hübers, K. Ilin, M. Siegel, I. Charaev, M. Moshkova, N. Kaurova, G. N. Goltsman, X. Zhang, and A. Schilling: *Electron energy relaxation in disordered superconducting NbN films*. Physical Review B **102** (2020), 054501. DOI: 10.1103/PhysRevB.102.054501 (cit. on p. 85).

[220] M. Sidorova, A. D. Semenov, H. W. Hübers, S. Gyger, and S. Steinhauer: *Phonon heat capacity and self-heating normal domains in NbTiN nanostrips*. Superconductor Science and Technology **35** (2022), 105005. DOI: 10.1088/1361-6668/AC8454 (cit. on p. 85).

[221] V. Lubchenko and P. G. Wolynes: *Intrinsic Quantum Excitations of Low Temperature Glasses*. Physical Review Letters **87** (2001), 195901. DOI: 10.1103/PhysRevLett.87.195901 (cit. on p. 85).

[222] V. Humbert, M. Ortuño, A. M. Somoza, L. Bergé, L. Dumoulin, and C. A. Marrache-Kikuchi: *Overactivated transport in the localized phase of the superconductor-insulator transition*. Nature Communications **12** (2021), 1–10. DOI: 10.1038/s41467-021-26911-7 (cit. on p. 86).

[223] R. H. Koch, D. P. DiVincenzo, and J. Clarke: *Model for* $1/f$ *Flux Noise in SQUIDs and Qubits*. Physical Review Letters **98** (2007), 267003. DOI: 10.1103/PhysRevLett.98.267003 (cit. on p. 86).

[224] R. M. Lutchyn, L. Cywinksi, C. P. Nave, and S. Das Sarma: *Quantum decoherence of a charge qubit in a spin-fermion model*. Physical Review B **78** (2008), 024508. DOI: 10.1103/PhysRevB.78.024508 (cit. on p. 86).

[225] K. Agarwal, I. Martin, M. D. Lukin, and E. Demler: *Polaronic model of two-level systems in amorphous solids*. Physical Review B **87** (2013), 144201. DOI: 10.1103/PhysRevB.87.144201 (cit. on p. 87).

[226] S. Machlup: *Noise in Semiconductors: Spectrum of a Two-Parameter Random Signal*. Journal of Applied Physics **25** (1954), 341–343. DOI: 10.1063/1.1721637 (cit. on p. 120).

[227] F. Harris: *On the use of windows for harmonic analysis with the discrete Fourier transform*. Proceedings of the IEEE **66** (1978), 51–83. DOI: 10.1109/PROC.1978.10837 (cit. on p. 122).

# List of Publications


[1] M. Kristen, A. Schneider, A. Stehli, T. Wolz, S. Danilin, H. S. Ku, J. Long, X. Wu, R. Lake, D. P. Pappas, A. V. Ustinov, and M. Weides: *Amplitude and frequency sensing of microwave fields with a superconducting transmon qudit*. npj Quantum Information **6** (2020), 1–5. DOI: 10.1038/s41534-020-00287-w.

[2] M. Kristen, J. N. Voss, M. Wildermuth, H. Rotzinger, and A. V. Ustinov: *Random telegraph fluctuations in granular microwave resonators*. Applied Physics Letters **122** (2023), 202602. DOI: 10.1063/5.0147430.

[3] M. Kristen, J. N. Voss, M. Wildermuth, J. Lisenfeld, H. Rotzinger, and A. V. Ustinov: *Observation of two level systems with a giant dipole moment in superconducting granular films*. In preperation (2023).

# Appendix

## A Fabrication parameters

**Table A.1: Granular aluminum evaporation.** All films were deposited in a dynamic sputter process with a plasma voltage of $U_{\mathrm{spt}} = 400\,\mathrm{V}$ ($P_{\mathrm{spt}} = 50\,\mathrm{W}$). The film resistance is controlled by the flow of the ArOx gas at a constant flow of pure Ar (15 sccm), but also depends on the final film thickness $t_{\mathrm{f}}$. For the two layer samples (D+E), the ArOx flow as abruptly increased upon reaching the desired thickness ($\sim 25\,\mathrm{nm}$) of the bottom layer. Note that samples A, D and E were deposited after some slight modifications have been applied to the sputter chamber, compared to sample B and C.

| sample | rate (nm/s) | ArOx flow (sccm) | ArOx flow top layer (sccm) | $t_{\mathrm{f}}$ |
|---|---|---|---|---|
| A | 0.0476 | 2.55 | - | 24 |
| B | 0.0513 | 3.55 | - | 22 |
| C | 0.0588 | 3.70 | - | 30 |
| D | 0.0476 | 2.55 | 3.0 | 24+18 |
| E | 0.0476 | 2.57 | 3.57 | 23+17 |

**Table A.2: Resist application.** To cover the films with a $\sim 1.2\,\mu\mathrm{m}$ thick AZ5214E resist, the spincoater first rotates with a speed of $v_r$ for time $t_r$ to equally distributed the resist over the chip, and then accelerates with $a$ to the final speed $v_s$ which determines the thickness of the resist. After a time $t_s$ at full speed, the chip is removed from the spincoater and subsequently softbaked at temperature $T_B$ for a time $t_B$.

| resist | $a$ (rpm/s) | $v_r$ (rpm) | $t_r$ (s) | $v_s$ (rpm) | $t_s$ (s) | $T_B$ (°C) | $t_B$ (s) |
|---|---|---|---|---|---|---|---|
| AZ5214E | 7500 | 500 | 5 | 6000 | 60 | 110 | 50 |

**Table A.3: Optical exposure.** Optical light at a fixed intensity from a XeHg lamp (wavelength $\lambda = 365\,\text{nm}$) is used to expose the resist through a hard mask covering the desired structures.

| resist | process | intensity ($\text{mW/cm}^2$) | duration (s) |
|---|---|---|---|
| AZ5214E | positive | 13 | 5 |

**Table A.4: Resist Development.** Previously exposed areas of the resist get dissolved by a developer (positive process). To avoid damage to unexposed areas, the development is limited to a certain duration and eventually terminated by an appropriate stopbath.

| resist | developer | duration (s) | stopbath |
|---|---|---|---|
| AZ5214E | AZ Developer (+H20 1:1) | 33 | water |

**Table A.5: Film Etching.** An inductively coupled chlorine based ion plasmas is used for isotropic etching of all areas of the granular aluminum film not covered by resist. There, the ratio between the etching gasses as well as the chamber pressure $p$ are fixed. Separate RF and ICP generators provide control over ion energy and ion density. For two layer samples (D+E), the etching time is increased from 50 s to 90 s. After etching, the remaining resist is removed by a solvent (aceton or NEP).

| system | p (mTorr) | gasses (sccm) | rf power (W) | ICP power (W) | time (s) |
|---|---|---|---|---|---|
| ICP | 10 | Ar/CL (2/12) | 100 | 200 | 50(+40) |

# B Cable attenuation

To estimate the average photon number on resonance from Eq. 3.20, knowledge of the resonator input power is required, which can be calculated from

$$P_{\text{in}} = P_{\text{VNA}} - \text{Att.}. \tag{B.1}$$

Here, $P_{\text{VNA}}$ is the output power of the VNA and the total attenuation Att. is the sum of all installed attenuators ($20\,\text{dB} + 10\,\text{dB} + 10\,\text{dB} + 10\,\text{dB} = 50\,\text{dB}$, Fig. 4.4) plus the attenuation from the microwave cable. Figure B.1 shows the total attenuation of all used measurement lines, corrected for the fact that (at 10 GHz) the stainless steel wires have 23.5 dB/m at room temperature (where the transmission spectrum was measured) but 14.7dB/m at 4 K.

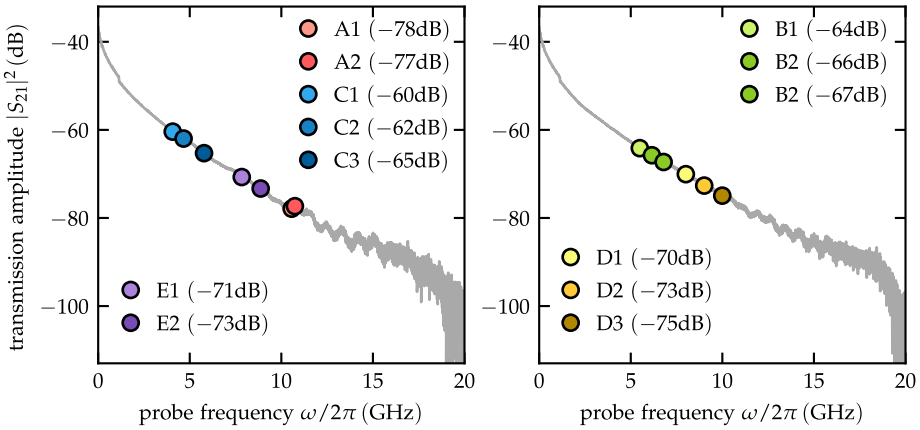


**Figure B.1: Microwave transmission line spectra.** Amplitude transmission spectra of the two microwave lines used to guide the readout signal from the network analyzer to the sample. For each line, the resonators measured on that particular line are marked, together with the total attenuation at their respective resonance frequency.

# C Noise measurements details

## C.1 Noise spectrum of a RTS

In this section a short derivation of the Lorentzian spectrum of a random telegraph signal (RTS) is provided [226]. Usually, the RTS is defined as a random signal, that might be in one of two state, called 0 and 1 in the following. The probability of making a transition from 0 to 1 in a short time $dt$ is $dt/\sigma_0$ and similarly, $dt/\sigma_1$ is the probability to make a transition from 1 to 0. Thus, $\sigma_0$ and $\sigma_1$ are the mean lifetimes of the respective states and the corresponding probabilities to be in that state are $\sigma_0/(\sigma_0+\sigma_1)$ and $\sigma_1/(\sigma_0+\sigma_1)$. In experimentally measured RTS data, state 1 usually only occurs for a small fraction of the time and $\sigma_1 \ll \sigma_0$ will thus be assumed in the following.

To obtain the noise spectrum, it is useful to first calculate the autocorrelation function and then apply the Wiener–Khinchin theorem. Assuming that the signal $x(t)$ may take on the values $x_0 = 0$ and $x_1 = A$, the autocorrelation function can be written as

$$\begin{aligned} r_{xx}(s) &= \langle x(t)x(t+s)\rangle \\ &= \sum_{i,j} x_i x_j \times P(x(t)=x_i) \times P(x(t+s)=x_j \text{ given } x(t)=x_i) \\ &= A^2 \frac{\sigma_1}{\sigma_1+\sigma_0} P_{11}(s) \\ &\approx A^2 \frac{\sigma_1}{\sigma_0} P_{11}(s). \end{aligned} \tag{C.1}$$

Further, one can derive the probability for an even number of transitions in the time increment $s+ds$,

$$P_{11}(s+ds) = P_{10}(s)\frac{ds}{\sigma_0} + P_{11}(s)(1-\frac{ds}{\sigma_1}), \tag{C.2}$$

from the sum of two mutually elusive events: (1) the probability $P_{10}(s)$ for an odd number of transitions during $s$ followed by one transition in $ds$ and (2) the probability for an even number of transitions in $s$ and no transition in $ds$. Solving Eq. C.2 in the limit $ds \to 0$ and for $\sigma_1 \ll \sigma_0$ yields

$$P_{11}(s) \approx \mathrm{e}^{-s/\sigma_1}. \tag{C.3}$$

Finally, inserting Eq. C.3 into Eq. C.1, the spectrum can be calculated from the the Fourier transform of the autocorrelation function (Wiener–Khinchin formula)

$$\begin{aligned} S(f)_{\sigma_1 \ll \sigma_0} &= \int_{-\infty}^{\infty} r_{\mathrm{xx}}(s) \mathrm{e}^{-2\pi i f s} ds \\ &= \frac{A^2}{\pi} \frac{\sigma_1}{\sigma_0} \frac{\frac{1}{\sigma_1}}{(2\pi f)^2 + \left(\frac{1}{\sigma_1}\right)^2} \\ &= \frac{A^2}{\pi} \frac{\sigma_1}{\sigma_0} \frac{\sigma_1}{1 + (2\pi f \sigma_1)^2} \end{aligned} \tag{C.4}$$

For $\bar{I}^2 \equiv A^2 \sigma_1 / (4\pi\sigma_0)$ and $\tau_0 \equiv \sigma_1$ Eq. C.4 is identical to Eq. 4.11, which is the most commonly used expression.

## C.2 PSD window comparison

In Welch's algorithm for the power spectral density (PSD) (see Sec. 4.3.2), the overlapping segments are tapered by a window function before the Fourier transform is performed. Because, generally, the choice of the particular window can have an (unwanted) effect on the final spectrum [227], their influence on the noise analysis was investigated for this work. However, as shown in Fig. C.1, the noise spectra does not depend on the choice of the window function. Thus, the standard Hanning window was used throughout this work.

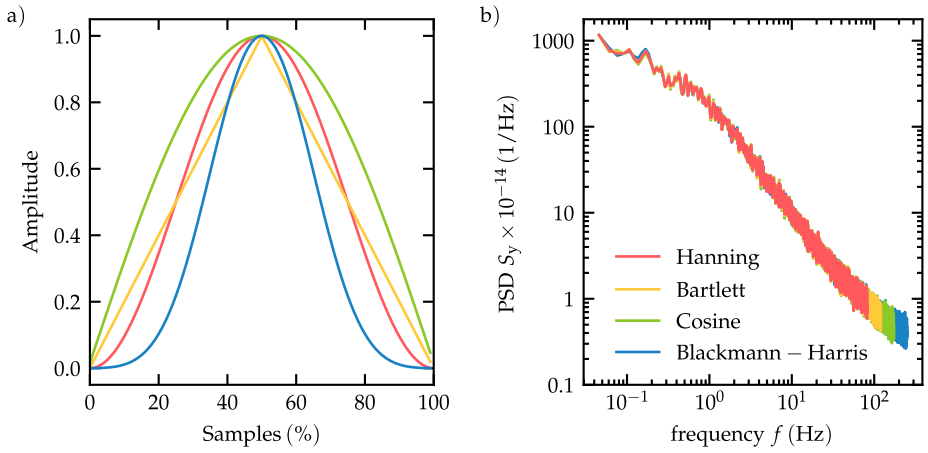


**Figure C.1: Welch windows comparison. a)** Selection of window functions. **b)** Resonator noise spectrum calculated with Welch's method, using the respective windows shown in a). Some spectra were shortend to highlight the overlap.

# D Additional TLS data

## D.1 TLS parameter

**Table D.1: TLS key parameter.** Tunneling energy $\Delta_{\mathrm{TLS}}$ and asymmetry energy $\epsilon_{\mathrm{TLS}}$ (both in units of $\mu$eV) obtained from fits to all pronounced anti-crossings measured on samples A-C. The effective coupling to the applied electrode voltage $[p^*] = \mathrm{GHz/V}$ is proportional to the TLS dipole moment (see Sec. 4.4 for details).

| TLS | $\Delta_{\mathrm{TLS}}$ | $\epsilon_{\mathrm{TLS}}$ | $p^*$ | TLS | $\Delta_{\mathrm{TLS}}$ | $\epsilon_{\mathrm{TLS}}$ | $p^*$ |
|---|---|---|---|---|---|---|---|
| A1(#1) | 43.66 | 205.05 | 0.48 | C3(#6) | 16.65 | 1325.22 | 1.71 |
| A1(#2) | 43.66 | 241.59 | 0.85 | C3(#7) | 16.51 | 601.68 | 1.64 |
| A1(#3) | 42.91 | 518.44 | 0.81 | C3(#8) | 16.37 | 1034.91 | 2.99 |
| A1(#4) | 43.2 | 41.45 | 0.29 | C3(#9) | 16.66 | 53.77 | 0.93 |
| A2(#5) | 42.47 | 476.89 | 1.03 | C3(#10) | 16.58 | 539.32 | 4.05 |
| B2(#1) | 22.64 | 291.21 | 0.94 | C3(#11) | 18.86 | 1206.17 | 2.36 |
| B2(#2) | 22.65 | 260.66 | 1.01 | C3(#12) | 18.86 | 522.9 | 1.9 |
| B2(#3) | 22.1 | 282.83 | 0.94 | C3(#13) | 19.15 | 293.22 | 1.12 |
| B2(#4) | 19.92 | 803.3 | 2.43 | C3(#14) | 19.14 | 264.34 | 1.32 |
| B2(#5) | 22.66 | 106.11 | 1.73 | C3(#15) | 19.26 | 17.71 | 0.68 |
| B2(#6) | 24.39 | 1450.41 | 2.09 | C3(#16) | 19.22 | 49.13 | 0.98 |
| B3(#7) | 25.33 | 935.19 | 1.31 | C3(#17) | 18.99 | 305.79 | 0.95 |
| B3(#8) | 25.27 | 67.89 | 0.52 | C3(#18) | 7.68 | 75.88 | 0.13 |
| B3(#9) | 25.42 | 9.55 | 0.08 | C3(#19) | 19.08 | 1076.7 | 1.9 |
| B3(#10) | 24.77 | 435.52 | 1.62 | C3(#20) | 19.02 | 431.86 | 1.13 |
| B3(#11) | 25.23 | 872.6 | 1.14 | C3(#21) | 19.1 | 805.78 | 1.56 |
| B3(#12) | 27.03 | 1559.71 | 1.99 | C3(#22) | 23.75 | 1117.0 | 1.49 |
| B3(#13) | 27.39 | 552.53 | 1.4 | C3(#23) | 23.26 | 6.74 | 1.53 |
| B3(#14) | 27.87 | 44.87 | 0.55 | C3(#24) | 23.54 | 156.46 | 1.77 |
| B3(#15) | 28.05 | 21.66 | 0.32 | C3(#25) | 23.85 | 82.84 | 0.88 |
| B3(#16) | 28.01 | 125.53 | 0.54 | C3(#26) | 23.62 | 387.13 | 1.02 |
| C3(#1) | 16.81 | 1241.58 | 1.54 | C3(#27) | 23.64 | 91.1 | 1.24 |
| C3(#2) | 16.62 | 814.5 | 2.2 | C3(#28) | 23.62 | 835.63 | 3.78 |
| C3(#3) | 16.64 | 1025.05 | 3.96 | C3(#29) | 23.25 | 810.83 | 2.41 |
| C3(#4) | 16.79 | 36.24 | 0.76 | C3(#30) | 23.48 | 2222.08 | 3.18 |
| C3(#5) | 16.51 | 83.78 | 2.59 | C3(#31) | 23.62 | 1961.71 | 2.78 |

**Table D.2: TLS key parameter.** Tunneling energy $\Delta_{\mathrm{TLS}}$ and asymmetry energy $\epsilon_{\mathrm{TLS}}$ (both in units of $\mu$eV) obtained from fits to all pronounced anti-crossings measured on samples D+E. The effective coupling to the applied electrode voltage $[p^*]$ = GHz/V is proportional to the TLS dipole moment (see Sec. 4.4 for details).

| TLS | $\Delta_{\mathrm{TLS}}$ | $\epsilon_{\mathrm{TLS}}$ | $p^*$ | TLS | $\Delta_{\mathrm{TLS}}$ | $\epsilon_{\mathrm{TLS}}$ | $p^*$ |
|---|---|---|---|---|---|---|---|
| D3(#1) | 33.12 | 34.04 | 0.12 | E2(#2) | 32.19 | 134.56 | 4.28 |
| D3(#2) | 32.9 | 49.38 | 0.09 | E2(#3) | 32.16 | 576.16 | 4.78 |
| D3(#3) | 32.88 | 745.26 | 0.99 | E2(#4) | 32.28 | 536.71 | 3.73 |
| D3(#4) | 32.75 | 217.21 | 0.83 | E2(#5) | 32.26 | 713.99 | 3.73 |
| D3(#5) | 33.1 | 37.12 | 0.12 | E2(#6) | 32.4 | 201.34 | 0.28 |
| D3(#6) | 33.03 | 426.07 | 0.76 | E2(#7) | 32.41 | 83.49 | 0.21 |
| D3(#7) | 33.1 | 408.25 | 0.67 | E2(#8) | 31.77 | 166.93 | 1.31 |
| D3(#8) | 36.68 | 119.15 | 0.52 | E2(#9) | 32.01 | 477.9 | 1.57 |
| D3(#9) | 37.2 | 271.47 | 1.4 | E2(#10) | 32.27 | 680.56 | 1.9 |
| D3(#10) | 36.81 | 60.96 | 0.23 | E2(#11) | 36.64 | 2017.75 | 2.7 |
| D3(#11) | 36.96 | 134.67 | 0.51 | E2(#12) | 36.59 | 1113.33 | 1.99 |
| D3(#12) | 41.3 | 550.39 | 1.37 | E2(#13) | 36.69 | 257.15 | 0.39 |
| D3(#13) | 41.2 | 861.65 | 1.25 | E2(#14) | 36.59 | 1260.49 | 1.9 |
| D3(#14) | 41.26 | 388.15 | 2.2 | E2(#15) | 36.67 | 792.18 | 1.14 |
| D3(#15) | 38.67 | 314.63 | 1.58 | E2(#16) | 36.44 | 581.81 | 0.91 |
| D3(#16) | 40.6 | 488.87 | 0.98 | E2(#17) | 36.14 | 487.04 | 0.75 |
| E2(#1) | 32.38 | 2879.02 | 3.63 | E2(#18) | 36.64 | 833.11 | 1.17 |

## D.2 Anticrossing gallery

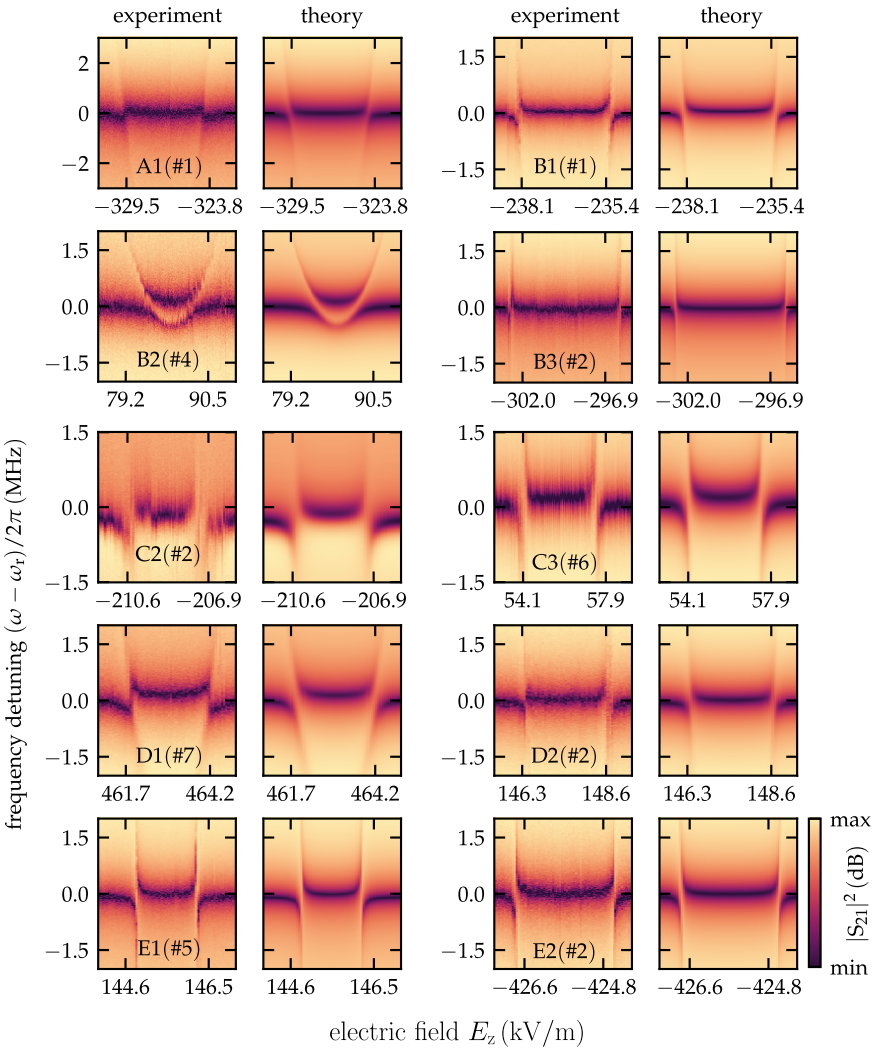


**Figure D.1: Anticrossing gallery.** Selection of transmission spectra from different resonators strongly coupled to a TLS. The experimental data can be fitted by input-output theory (Eq. 6.3)

.

## D.3 Thermal cycling

In Ref. [201], the argument was made that the spectral reconfiguration of TLS after mild thermal cycling is evidence for TLS originating from trapped quasiparticles rather than atomic defects. For the TLS investigated int his work, similar experiments were performed. A shown in Fig. D.2, a slight shift of the TLS traces (dark line) can be observed after cyling the sample to 1.8 K for several minutes. However, simply waiting between two measurements seems to have a similar effect (Fig. D.2(c), see also Fig. 6.5). Thus, possible effects due to the reconfiguration of the gap $\Delta$ are obscured by existing temporal fluctuations, i.e., thermal cycling experiments do not provide further information.

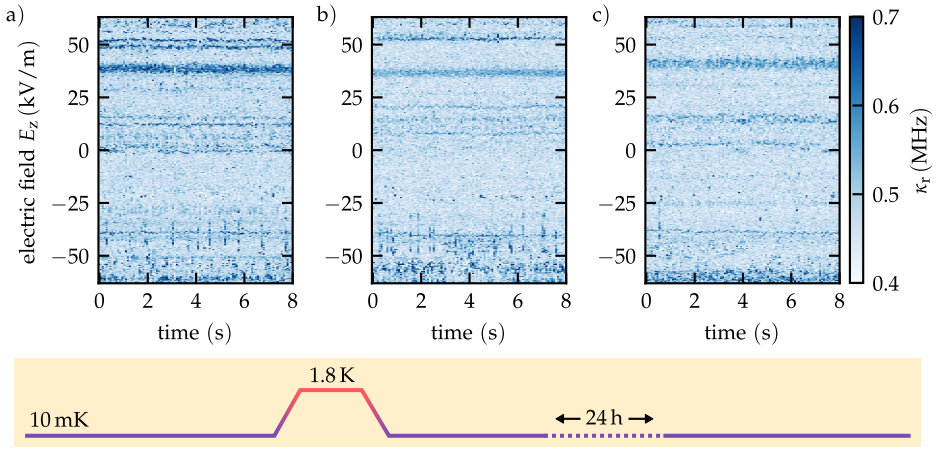


**Figure D.2: Spectral reconfiguration of TLS. a)** Resonator (C3) loss rate over time as a function of the electric field. Dark traces indicate an increased loss rate due to the interaction with a TLS. **b)** Same as in a), but after thermal cycling the sample to 1.8 K. **c)** Same as in b), but after a 24 h wait.

# Acknowledgements

Back when I was in school, my physics teacher wrote Heisenberg's uncertainty principle on the board one day and we would discuss its implications and work out some rudimentary, phenomenological derivation. He then told us that in order to see the actual derivation that would also explain the prefactor to Planck's constant, one would have to finish school and then study physics. Which is what I did. There, it was thanks to many wonderful friends that I had as much fun outside university as I had studying the fundamentals of nature. These studies now culminated in this thesis, which would not have been possible without guidance and assistance from many people whom I would like to acknowledge in the following.

I want to thank Prof. Alexey Ustinov for the opportunity to work in his group and for supervising this thesis. His ability to point out the important details while remaining aware of the bigger picture has helped focusing my efforts in the right direction whenever we discussed my work. I am particularly grateful for the possibility to visit different conferences and seminars in and outside Europe.

I want to thank Prof. Alexander Shnirman for being the second reviewer of this thesis and for his countless contributions to the field of superconducting circuits.

A special thanks go to Hannes Rotzinger for his consistent support throughout my work as a PhD student. Not only is he a great person to discuss physics (or non-physics) topics, he also encouraged me in my discussion making when I faced my largest challenges. For this I am very gratefully.

A big thanks also goes to Jan Nicolas Voss and Micha Wildermuth , together with whom I had the pleasure to investigate the peculiarities of granular aluminum. I enjoyed discussing and tackling problem with you as much as I cherished our time outside the lab.

My gratitude also goes to Andre Schneider, whose guidance in and outside academia has helped me grow as a person in the last couple of years. I owe him all my expertise on cryogenic setups as well as bad jokes and I am very found of all the fun memories we made together in our free time.

I want to thank Jürgen Lisenfeld and Alex Bilmes for sharing their expertise on two-level systems and for always having an open ear for my questions.

I would also like to thank Jochen Braumüller and Alex Stehli for mentoring me during my early steps as a scientist and for introducing me to the field of superconducting circuits. Similarly, I am grateful to Tim Wolz, who taught me many things, from noise measurements to scientific writing, as well as Jan Brehm and Steffen Schlör, for inspiring me with their passion for and knowledge of science and technologies.

I greatly appreciate the patience and support of Yannick Schön, Lucas Radtke, Silvia Diewald and Aina Quintilla during the fabrication of countless samples. I am glad a did not have to tackle the challenges the cleanroom holds on my own.

Additional and special thanks goes to the secretaries of the PI, Steffi Baatz and Claudia Alaya, and the IQMT, Carmen Dörflinger and Dorothea Trautmann, as well as Michael Meyer and Jannis Ret from the workshop. It was thanks to their assistance that I could turn my attention solely to science.

Finally, I want to express my thanks to all other current and former members of the Ustinov group, particularly András Di Giovanni, Alex Kreuzer, Hossam Tohamy, Markus Griedel, Konstantin Händel, Benedikt Berlitz and Gerda Fisher, for providing such a positive working environment.

Last but not least I want to thank my family, to whom I owe the opportunity and privilege to peruse such a long academic journey. Their unconditional love and support allowed me to become the person I am today. My very last thanks goes to Janina, for never failing to put a smile on my face. I love you and I am grateful to have you by my side.

Karlsruhe, June 2023 M. Sc. Maximilian Kristen